INFORMATION TO USERS

The most advanced technology has been used to photograph and reproduce this manuscript from the microfilm master. UMI films the text directly from the original or copy submitted. Thus, some thesis and dissertation copies are in typewriter face, while others may be from any type of computer printer.

The quality of this reproduction is dependent upon the quality of the copy submitted. Broken or indistinct print, colored or poor quality illustrations and photographs, print bleedthrough, substandard margins, and improper alignment can adversely affect reproduction.

In the unlikely event that the author did not send UMI a complete manuscript and there are missing pages, these will be noted. Also, if unauthorized copyright material had to be removed, a note will indicate the deletion.

Oversize materials (e.g., maps, drawings, charts) are reproduced by sectioning the original, beginning at the upper left-hand corner and continuing from left to right in equal sections with small overlaps. Each original is also photographed in one exposure and is included in reduced form at the back of the book. These are also available as one exposure on a standard 35mm slide or as a 17" x 23" black and white photographic print for an additional charge.

Photographs included in the original manuscript have been reproduced xerographically in this copy. Higher quality 6" x 9" black and white photographic prints are available for any photographs or illustrations appearing in this copy for an additional charge. Contact UMI directly to order.

U·M·I

Effects of gravity waves on the polar O_2 and OH airglow

Viereck, Rodney Allen, Ph.D.

University of Alaska Fairbanks, 1988

EFFECTS OF GRAVITY WAVES

ON THE

POLAR O_2 AND OH AIRGLOW

A

THESIS

Presented to the Faculty of the University of Alaska

in Partial Fulfillment of the Requirements

for the Degree of

DOCTOR OF PHILOSOPHY

By

Rodney A. Viereck, M.S.

Fairbanks, Alaska

May, 1988

EFFECTS OF GRAVITY WAVES

ON THE
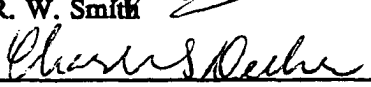
POLAR O_2 AND OH AIRGLOW

by

Rodney A. Viereck
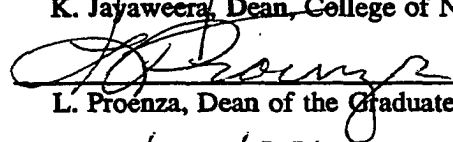
RECOMMENDED:

V. Degen

D. C. Fritts

M. H. Rees

R. W. Smith

C. S. Deehr, Chairman, Advisory Committee

J. L. Morack, Head, Physics Department

APPROVED:

K. Jayaweera, Dean, College of Natural Sciences

L. Proenza, Dean of the Graduate School

2/12/88

Date

Abstract

The effect of gravity waves on the OH (87 km) and O_2 (95 km) airglow emissions was examined using spectroscopic airglow data. The data was obtained from Longyearbyen, Svalbard (78°N) and Fairbanks, Alaska (64°N) using Ebert-Fastie spectrometers and a system of Meridian Scanning Photometers. The spectrometers scanned in wavelength from 8200Å to 8750Å which included the airglow emissions from the OH(6-2) Meinel band and the O_2(0-1) atmospheric band. The analysis was done by fitting a synthetic spectrum to the data and thereby the rotational temperature was calculated as well as the band intensity of each of the emissions. The rotational temperatures were assumed to represent the temperature of the emission region.

Gravity waves were assumed to modify the density and temperature of the atmosphere in the region of the airglow emissions. These modifications were measured as fluctuations in the band intensity and rotational temperatures of the two emissions. In order to compare the data with theoretical models, it was necessary to calculate two parameters. The parameter η is defined as the ratio of the amplitudes of the fluctuations in intensity and temperature. The other parameter is the phase angle between the fluctuations in intensity and temperature. These parameters were found to vary with wave period. The variations in η and phase agreed fairly well, for long period waves, with the most recent models. None of the models agree with the observed values of η and phase for short period waves.

The second part of this thesis examines the vertical and horizontal wavelengths, the phase speeds, and the propagation directions of several specific gravity wave examples. During a 60 hour period of data taken from Svalbard, three well defined gravity

waves were observed. The propagation directions implied a moving source south of the observing station.

Table of Contents

List of Figures

List of Tables

xi

Acknowledgments

xii

I would like to thank Dr. Mike Hickey of NASA who, through several discussions, provided me insight on the interpretation of my results. At the time that this thesis was being written, Mike had only submitted his papers on gravity waves and the airglow. His work seems to be the only theory which agrees with my data. I hope that he continues to work in the field.

This thesis was printed with a software package called TeX. The program is very powerful, but also somwhat confusing. The original TeX Macro routines, that were used to format this thesis, were graciously provided by Dirk Lummerzheim (now Dr. Dirk). Several other students helped by providing a good working atmosphere. These include, but are not limited to, my office partner Jim Conner, and my good friends Mark Mandt and Gerald Walker, both of whom had better be there to graduate with me.

I would also like to acknowledge Sheila Finch, who not only *profread* this thesis out of the goodness of her heart, but also typed numerous other documents at speeds which boggle the mind.

Finally, I would like to thank my wife Donna, who supported me with her love and understanding, and my baby daughter Lauren, who provided the final inspiration to complete this thesis.

CHRISTMAS ON SVALBARD
(to the tune of 'Dark as Dungeon)

It's up every morning to a wonderful sight
a bowl full of oatmeal and pickled herring delight
We dig in with gusto and narry a sound
'bout the codliver oil that washes it down.

Chorus:
   Where it's dark as a dungeon and cold as hell too
   Where the troubles are many and the pleasures are few
   Where the sun never shines and the winds always blow
   Its so cold on Svalbard, its no place to go

Out to the station for another days work
and a look at the data that the instruments took
But the power had failed and the instruments quit
so all of our data is nothing but ...garbage

So we slave and we labour all day and all night
on computers with memories that aren't working right
and Ebert and Fastie, and Mr. Fabry Perot
are fed to the polar bears out in the snow

After all is repaired and looks as it should
the weather turns cloudy and the data's no good
So we head into town for a night of good cheer
and drown all our troubles in Mack Polar Beer

Next day with hangovers we set out in pain
just to find that the Russians have been spying again
They believe that we're spys for the US CIA
but they always bring vodka so all is OK

It's Christmas on Svalbard and the Norsk food is a treat
Mutton and Potatoes washed down with Aquavit
we begin to relax when our kind host replies
'You must try some fish, it's been rotting in lye'

xiv

CHAPTER 1

Introduction To Gravity Waves and Airglow

The earth's atmosphere is different from that of all other known planets and these differences are what make the planet earth inhabitable for humans. Not only does the atmosphere provide life-giving gases such as O_2 and CO_2, but it also protects many life forms from harmful types of radiation from space, such as the ultra-violet solar radiation. The atmosphere also acts as a thermal regulator so that the difference between night and day is only tens of degrees Celsius rather than hundreds. Similarly the average surface temperatures at the poles and the equator are within one hundred degrees Celsius. The scale of human activity has increased to the point that its effect on the atmosphere is no longer insignificant. It is for these reasons that our understanding of the atmosphere and its processes is so important.

1.1 Gravity Waves in the Atmosphere

The redistribution of atmospheric energy is often the result of convection (winds). Another way in which energy is transported from one region to another is by the creation, propagation and dissipation of waves. Atmospheric waves range from very short, high-frequency sound waves to the very long, low-frequency planetary waves and tides which make up the weather systems. In the middle of the spectrum is a class of waves called *gravity waves*. Gravity wave periods range from several minutes to more than one day. The term *gravity wave* is derived from the fact that the force of gravity is the major restoring forces for the oscillatory motion. The opposing force is buoyancy due to the vertical density gradient.

1

The upper frequency limit of gravity waves is the natural frequency of a parcel when displaced from its equilibrium position. If a parcel of air is lifted into a region of less dense air the force of gravity is no longer balanced by the force of buoyancy and the parcel of air will fall back to its original position. As it accelerates, it gains downward momentum and overshoots its equilibrium position. The parcel is then in a region of more dense air and is buoyed back upward. Thus, the air parcel bobs up and down like a cork in the water. The natural frequency of this motion is called the *buoyancy frequency* or the *Brunt-Väisälä frequency*. The low frequency, or long period, limit is called the *inertial frequency* near which the parcel moves over such large time and distance scales that the Coriolis effect is important. It should be noted that the gravity waves described thus far are in a class called *internal* gravity waves. The other class of gravity waves is called *surface* gravity waves and include the waves on the surface of water.

The sources of internal gravity waves in the atmosphere have been observed to include topography, wind shear, and convection, as well as many others. Thunderstorms and nuclear explosions often produce large scale rapid upward motions (convection) which push parcels of air upward into regions where the air is less dense, and thus start the oscillatory motion associated with gravity waves. Other gravity wave sources include the interaction between strong winds and mountain ranges (topography). If the vertical motion associated with the gravity wave production is slow enough, then the temperature and density of the air parcel have time to adjust to their surrounding environment. This is called diabatic motion and is very slow. It is when the vertical motion is too rapid (adiabatic) to allow for the parcel to adjust to equilibrium with the surrounding environment, that gravity waves are formed.

One of the relevant properties of gravity waves is that they may be assumed to propagate upward. Under the assumption of energy conservation, the amplitude of a gravity wave depends inversely on the density of the medium and thus a small amplitude

gravity wave at the surface of the earth can grow to a very large wave in the upper atmosphere. The upward propagating wave grows until its amplitude is so large that the wave becomes unstable. This is known as a breaking gravity wave.

It has been theorized that the dynamics of the upper mesosphere (70-100 km) are largely influenced by the propagation and dissipation of internal gravity waves. Since the first gravity wave theory of *Hines* [1960] was used to explain the wave-like structures observed in meteor wind data, gravity waves have been proposed as a mechanism for numerous dynamical problems such as balancing the thermal budget of the upper atmosphere and explaining changes in the polar mesospheric temperatures associated with stratospheric warming events. Gravity waves may also play a role in the observed semidiurnal oscillations in the region of the mesopause [*Walterscheid*, 1981].

Numerous measurements of the effects of gravity waves have been made by radar and optical techniques. In the last decade, the importance of gravity waves in atmospheric models became more and more significant and new theories were being proposed. Numerous measurements of airglow emissions, such as those of *Krassovsky et al.* [1977], *Takahashi et al.* [1985] and *Taylor et al.* [1987], have observed wave-like structures with oscillatory motion in both the temporal and spatial frames. Similar wave-like structures have been observed in the summer-time, high latitude, noctilucent clouds which occur at similar altitudes to the airglow emissions. These wave-like structures are attributed to the passage of gravity waves.

1.2 The Airglow

The nightime airglow is a phenomenon associated with the chemistry of the atmosphere. The thermal motion of the atoms and molecules in the atmosphere can result in collisional recombination of atoms and molecules producing different chemical species.

The product atoms or molecules are often formed in vibrationally excited states. The excited molecule or atom will return to its lowest energy state and in the process, it will radiate energy or give up energy to other species by collision. The radiated energy is in the form of a photon and the wavelength of the photon is determined by the amount of energy released in the transition. The emitted photons are often observable from the ground and make up the airglow of the atmosphere. The airglow is quite weak and usually observable only at night (nightglow); however, under certain circumstances it may be observed during the day (dayglow).

For some species, the excited molecules are *metastable* and therefore, collisionally deactivated or *quenched*. Collisional deactivation does not produce radiation. For this reason, there are few airglow emissions from the lower atmosphere where the collision frequency is high. The upper atmosphere is much less dense and the collision frequency is much lower; thus, there is a better chance for a molecule to go from an excited state to its ground state through radiation.

The brightness, or intensity, of an airglow emission is proportional to the number of radiating molecules or atoms in the excited state. This can be related to the total density of the species. The different lines associated with each molecular transition are a result of the internal rotational structure of the diatomic or radical molecule. It can be shown (see Appendix A) that the relative intensities of the lines that constitute the rotational structure of the emission spectrum, are dependent on the rotational temperature. One of the primary assumptions of our airglow research is that the OH and O_2 molecules undergo enough collisions, while in the excited state, that the rotational temperature is the same as the atmospheric temperature of the local region of the emitting molecule.

1.3 Gravity Waves and the Airglow

The first observations of gravity waves in the OH airglow were made by *Krassovsky* [1972] and in an attempt to quantify his observations, *Krassovsky* defined a parameter η, which is the ratio between the percentage of the fluctuations in intensity to percentage of the fluctuations in temperature. More specifically, $\eta = \frac{\delta I/\bar{I}}{\delta T/\bar{T}}$ where the δ implies wave amplitude and the *overbar* is the mean. *Krassovsky* used linear gravity wave theory and calculated that $\eta = 3.5$. His observations were not in good agreement with his calculated value for η and he proposed an additional mechanism for the productionof OH* to explain his results.

Recently however, several models have included the effects of both the chemistry and the dynamics on the OH nightglow during the passage of gravity waves. The first part of this study is a comparison between observed fluctuations in the OH and O_2 airglow emissions with the recent model of *Walterscheid et al.* [1987] and the modifications to that model by *Hickey* [1987a,b]. For some gravity waves, there is fair agreement between the data and the theories. Also included in this discussion, is the study by *Hines and Tarasick* [1987]. These studies, along with several earlier studies by *Krassovsky* deal primarily with the OH emission. The O_2 emission has had relatively little attention. The only theoretical treatment of the effect of gravity waves on the O_2 emission is by *Weinstock* [1978]. The first part of this thesis includes the comparison of these theories with the observed fluctuations in the airglow.

The second part of this research was to study the propagation of high latitude gravity waves by observing the airglow at different altitudes and different positions. Two airglow emissions with two different emission heights can provide limited vertical information. The horizontal structure may be observed by using instruments that scan the sky. The

combined observations of horizontal and vertical structure of gravity waves in the upper mesosphere using airglow emissions is the subject of this work.

1.4 The Observations

The instruments used for this study were Ebert-Fastie spectrometers and a system of Meridian Scanning Photometers (MSP). There were two observing sites, each with similar instrumentation which included at least one spectrometer dedicated to the OH-O_2 airglow study and an MSP with one of the five channels available for OH measurements.

The two observing sites were located on opposite sides of the geomagnetic north pole. The Poker Flat Research Range, which is about 35 km north of Fairbanks, Alaska, (64°N, 145°W) is operated by the University of Alaska. The other site is near the town Longyearbyen, Svalbard (78°N, 16°E) about 1000 km north of Norway and was established as a joint venture between the University of Alaska and the University of Tromsø. The high latitude stations provide coverage of a part of the mesosphere which is not only interesting and relatively unexplored but also shrouded in darkness for much of the winter season. Svalbard is in total darkness for two months around the winter solstice which allows for uninterrupted diurnal measurements of the airglow. Continuous observations are imperative for studies of gravity waves, which are periodic with time scales between 5 minutes and 12 hours. It is for this reason that the in-depth analysis of gravity wave effects chosen for this thesis is concentrated on a three day period of data from Svalbard, during the last week of 1986.

CHAPTER 2

Instrumentation

The data set used in this study was obtained primarily by ground-based optical instruments for determining the intensity and rotational temperature of atmospheric molecular airglow emissions. To accomplish this objective, it was necessary to isolate appropriate spectral lines of the airglow emission spectra using instruments based on optical interference filters and diffraction gratings. The airglow emissions were observed in the night sky with diffraction grating spectrometers and a system of meridian-scanning photometers. The spectrometer was used to obtain spectra of the OH(6-2) and $O_2(0-1)$ band emissions with ~ 5Å spectral resolution (full width at half height). The meridian-scanning photometer system was used to obtain the brightness of individual spectral lines along the magnetic meridian. The following section is a summary of the principles of Ebert-Fastie spectrometers (EFS) and meridian scanning photometers (MSP) and the data analysis techniques.

2.1 Ebert-Fastie Spectrometers:

An Ebert-Fastie spectrometer consists of a spherically concave mirror, a plane reflective grating, and a pair of curved slits. The theory of this particular spectrometer configuration was first described by *Ebert* in 1889, and later, these simple monochromers were improved by *Fastie* [1952] for use as a spectral analyzer for metallurgical research.

The essence of the EFS is in the use of a single concave mirror to turn the incoming light into parallel rays and to refocus the diffracted light onto the exit slit as shown in

7
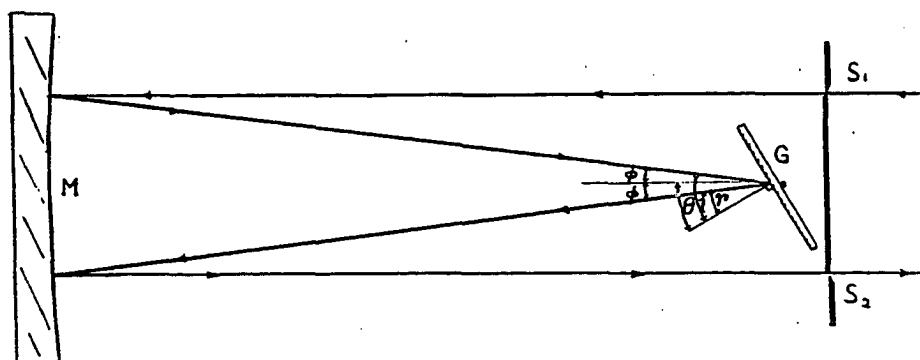
Fig. 2.1 Diagram of an Ebert-Fastie spectrometer. The incident light passes through the entrance slit, S_1, and is reflected onto the grating by the mirror, M. The curvature of the mirror turns the divergent rays of light, from the slit, into parallel rays. The light is dispersed by the grating, G and is refocused onto the exit slit, S_2, by the other half of the mirror. The wavelength of light that is focused onto the exit slit is a function of the grating angle θ.

Figure 2.1. The curved entrance and exit slits are both arcs of a circle which accommodate the spherical aberration of the main mirror along the length of the slits. This allows relatively long slits to be used without the corresponding loss of resolution. The incoming white light from the sky passes through the entrance slit and illuminates half of the mirror. The slits lie in the focal plane of the mirror and thus the divergent rays of light from the slit are transformed, by the curved mirror, into parallel rays of light which strike the grating. The angle of the divergent light from the grating can be related to the wavelength of the light by a simple equation, as will be seen. The dispersed light is

refocused by the second half of the mirror onto the exit slit, which lies in the focal plane of the mirror.

Reflected light is dispersed by a plane grating as shown in Figure 2.1 and the wavelength of the reflected light is dependent on the incident and reflection angles according to the *grating equation*

$$n\lambda = a(\sin i + \sin r) \quad n = 1, 2, 3, \cdots \qquad 2.1$$

where λ is the wavelength, n is the order, a is spacing between grating rules, i and r are the angles of incidence and reflection measured from the grating normal. The details of the Plane reflection grating are shown in Figure 2.2. The above equation can be modified to the Ebert-Fastie application by observing that the angles r and i, relative to the grating normal, and the angles θ and ϕ, as defined in Figure 2.1, are related such that

$$r = \theta - \phi$$

$$i = \theta + \phi$$

Substituting these equations into the equation 2.1, the grating equation can be rearanged to

$$n\lambda = 2a\sin\theta\cos\phi \qquad 2.2$$

In the Ebert-Fastie spectrometer, the angle ϕ is constant and the angle θ is the angle of the grating where $\theta = 0$ when the grating is perpendicular to the centerline, or optical axis, of the mirror. Given the parameters of the instrument, it is possible to calculate, by way of the grating equation, the grating angle required to observe a given wavelength.

It can be seen in Figure 2.1 that the field-of-view of the spectrometer is defined by the size and focal length of the mirror. The 1/2-meter EFS has a mirror area of about
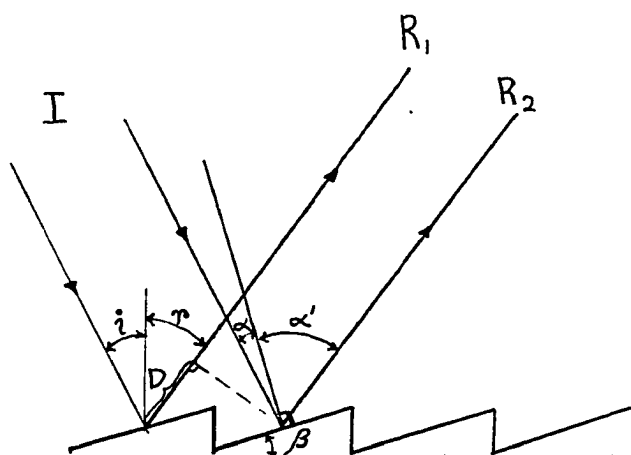
Fig. 2.2 Diagram of a plane reflection grating. Constructive interference will occur when the path difference, D, is equal to an integer number of wavelengths (i.e. $n\lambda = D$ $n = 1,2,3,...$). The wavelength of the reflected light is dependent on the the angle of incidence, i and the angle of reflection, r. The intensity of the reflected light will also depend on the *blaze angle* β where the maximum intensity will occur when the incident angle α is the same as the reflected angle α'. Note that at a given reflection angle there will be waves of wavelength $\lambda = D/n$, where n is any integer. Thus it will be necessary to isolate the desired wavelength with a broad band filter.

10cm×10cm and a distance to the slit of 1/2 meter. This defines a cone with a half angle (angle from center to edge) of about 5.5°. The cone angle is somewhat larger in the direction parallel to the slit of the spectrometer. The field-of-view of the 1/2 meter (1-meter) spectrometer resulted in a measurement area at 90 km altitude of about 17 km×21 km (9 km×12 km).

Scanning through the wavelength range is accomplished by means of an arm with one end attached to the grating mount and the other riding on a rotating cam. The cams

are designed such that the radius is a linear function of the rotation angle. Changes in the size of the wavelength region are done by replacing one cam by another with a different throw. Another way to change the size of the wavelength interval is to change the spectral order (n in equation 2.2) by changing the angle of the grating with respect to the cam arm. Since the wavelength, λ, is not linearly proportional to the the angle of the grating, θ, then a different value for n will result in a different wavelength range for the same range in θ. As the order increases, the wavelength interval per unit angle decreases. Thus, by going to the second order, the spectrometer can cover half the wavelength interval with the same throw of the cam but with twice the spectral resolution.

To separate overlapping orders, it is necessary to place a simple wavelength cutoff filter at the entrance slit. Corning glass filters were used in this study. The limit of the infrared sensitivity of the detector usually determined the long wavelength limit.

The detector that best suited the needs of this experiment was determined by the requirement for spectral sensitivity to almost 9000Å in wavelength, which is in the near infrared, or near IR, region of the spectrum. Any detector which is sensitive to these wavelengths will also be sensitive to the thermionic emission of the detector itself. Thus, it is usually necessary to cool these detectors. Our experiment also required that the instrument operate for several weeks without maintenance. The best, near-infrared, low maintenance, detector was found to be a Hamamatsu-942, Galium-Arsenide (GaAs) detector cooled to -25°C by means of a thermoelectric cooler. A 40 mm diameter, f/1 lens was used to focus all of the light from the 40 mm exit slit onto the 8 mm×10 mm photocathode (see Figure 2.1).

The detectors are essentially a solid photocathode (8mm×10mm) and an anode coupled by a chain of dynodes. This system, when maintained at high electric potential, will produce a pulse of electrons at the anode with each registered incident photon at the photocathode. The anode of the photomultiplier tube is connected to a pulse amplifier

and discriminator, or PAD, which converts the pulses of electrons into clean, 3 volt pulses of equal length. A microcomputer is used to count the number of pulses during a specified integration period and to record the results, along with time, date, and other details of the instrument settings, on magnetic tape.

The operating parameters of the spectrometers that were used in this study varied somewhat from one application to another. The focal lengths of the spectrometers were 500 mm and 1000 mm; the scan rate varied from 5 sec. to 30 sec.; and the spectral bandwidth was usually between 4Å and 10Å. Other adjustable parameters were the photomultiplier signal sampling rate, the spectral order, and the slit-width. All of these variables were optimized to minimize the error and maximize the temporal resolution depending on the conditions. For instance, the background spectral contamination due to the twilight could be overcome somewhat by reducing the slit-width and thus, the amount of background light. For spring and fall data, when the solar depression angle remained small, the slit was closed down to 0.1 mm. The sampling rate, the order, and the slit-width were all interdependent. The system was usually set up so that there were at least six samples per spectral line.

To obtain spatial information with an Ebert-Fastie spectrometer, the field-of-view was directed to three different azimuths at a constant elevation angle with a rotating mirror (see Figure 2.3). The angle of the mirror defined the elevation angle and the mirror was rotated to three azimuth positions. The mirror would remain in each position for a pre-determined number of scans. The directions most often used were magnetic north, south, and east at an elevation angle of 60°. This pattern resulted in observations of the emitting layer (85 to 95 km altitude) at a horizontal distance of 30 km and 50 km from the zenith point. During optimum conditions, six 30 sec. scans were taken at each position.
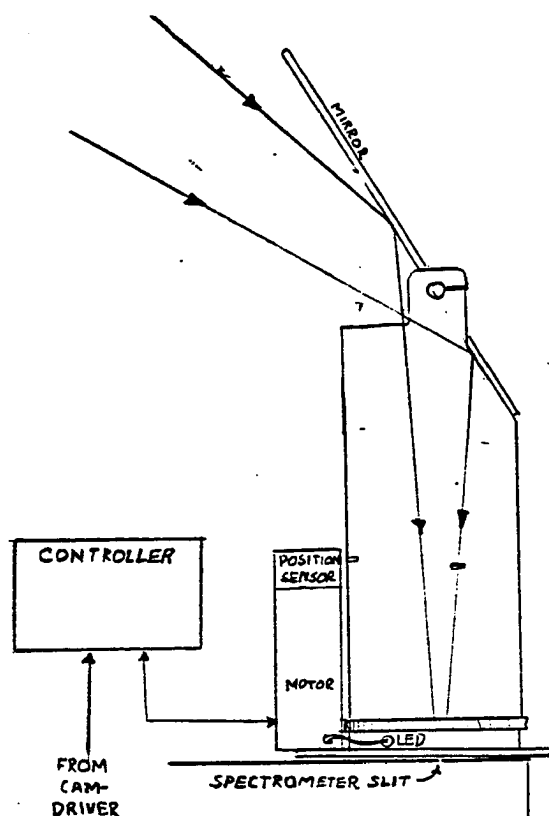
Fig. 2.3 Mirror system used on the Ebert-Fastie spectrometers. This system enabled the spectrometers to provide horizontal information. The LED (light emitting diode) was used to provide a mirror azimuth position indicator in the data.

2.2 Spectrometer Data and Analysis

The data records were written on magnetic tape and consisted of several 16 bit words of information such as time, date, spectral region, number of samples in the record, followed by a series of samples which represented photomultiplier counts in the sample intervals. Each of the sample intervals represented a wavelength bin. The spectrum could then be reconstructed by plotting the photomultiplier counts in each sampling interval as a linear function of wavelength.

In order to increase the signal-to-noise ratio (usually to a value of 2 or more), it was necessary to co-add (point-by-point addition of a time series) several data records. The number of records that were co-added, depended on the quality of the data and the purpose of the analysis. For instance, ten minute temporal resolution was not required to determine seasonal changes.

Once the desired number of data records were co-added together, it was necessary to calibrate the sensitivity of the instrument as a function of wavelength. Photomultiplier tubes are, in general, not equally sensitive across the entire spectral region, nor is the reflectance of the spectrometer grating or the dispersion of the instrument at the exit slit. It was necessary to compensate for these factors by calibrating each instrument individually. This was done by illuminating a $BaSO_4$-coated screen with a standard lamp of known brightness. The spectrometer was pointed at the screen, such that the screen filled its field-of-view, and then scanned through the wavelength interval of interest. This process resulted in a calibration curve (in Rayleighs per count) as a function of wavelength. Figure 2.4 shows the lamp-brightness curve (curve A), the observed brightness (curve B) and the resulting calibration curve (curve C) of a spectrometer. The final curve could then be multiplied by each scan resulting in a spectrum of brightness in Rayleighs as a function of wavelength.

After each spectrum was calibrated for intensity, it could then be used to determine the band intensity and rotational temperature. This was done by way of an iterative process of calculating the synthetic spectrum for a given rotational temperature and instrument function, and determining the least-mean-squares-difference, or L, between the data and model. By minimizing L with respect to the model temperature, it was possible to determine the temperature which best fit the data. The details of this process are discussed in the remainder of this section. The calculation of the synthetic spectrum
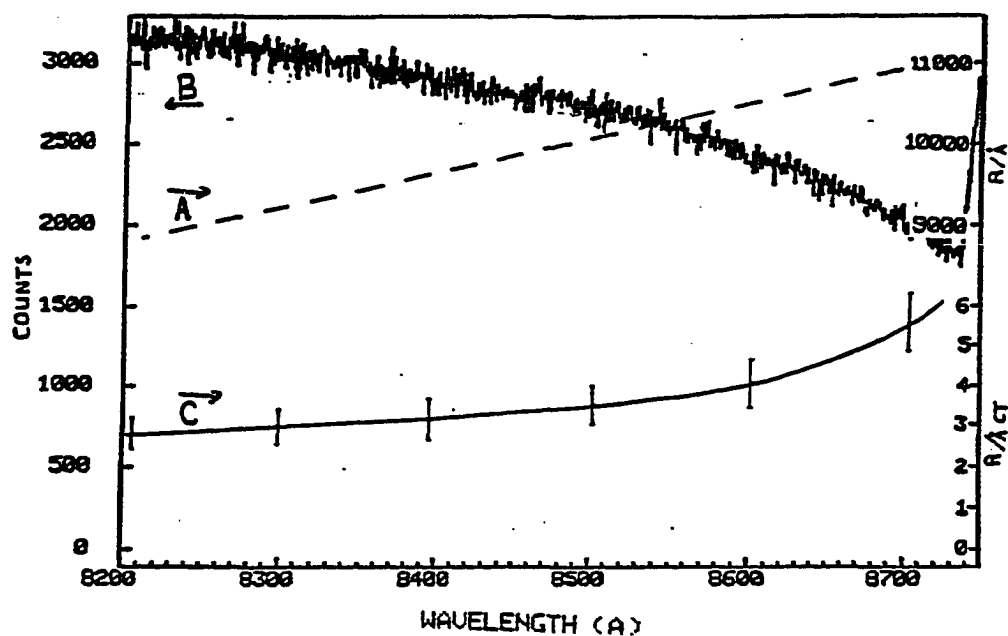
Fig. 2.4 This plot shows the three curves needed for calibrating the spectrometers all plotted as a function of wavelength. The calibration was done by pointing the spectrometer at a $BaSO_4$-coated screen which was illuminated by a standard lamp of known brightness in Rayleighs per Ångsrom (dashed curve A). This produced a spectrum of the lamp brightness convolved with the instrument sensitivity in counts (solid curve B). The two were combined to produce a calibration curve in units of Rayleighs per Ångstrom per count (curve C). Curve C could be multiplied by the data curve to produce a calibrated spectrum of the data in units of Rayleighs per Ångstrom.

is discussed in Appendix A. Figure 2.5 shows both the observed and the synthetic spectra for the OH (6-2) and the O_2 (0-1) vibrational bands.

A term called FIT was calculated using the following formula,

$$FIT = (100 - L)/100$$

This resulted in a variation of FIT from large negative numbers to $FIT = 1$ which corresponded to $L = 0$ or, in other words, a perfect fit. A new artificial spectrum was
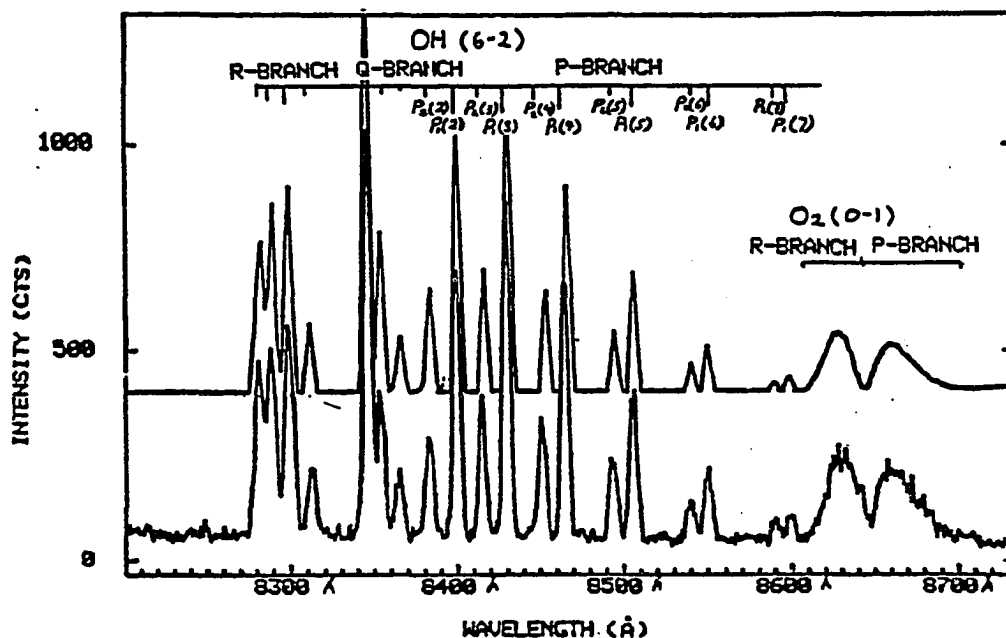
Fig. 2.5 Synthetic spectrum (top curve) and observed spectrum (bottom curve) for the OH (6-2) and O₂ (0-1) vibrational bands. Analysis was done by calculating the rotational temperature for which the difference between the two curves was minimized.

calculated for each of a series of rotational temperatures and thus, the fitting process was repeated several times for each data record. The temperature of the data was chosen to correspond with a maximum in the value FIT.

The fitting process required the calculation of four parameters. Given a data set, D_i, and a model set M_j, (i and j represent the ith and jth elements of the sets) there are two X-axis parameters and two Y-axis parameters that can be adjusted. The X-axis position for each element of the model was defined by

$$XPOS_j = XOFFSET + XSCALE \times j.$$

where $XOFFSET$ slides the model along the data set and $XSCALE$ expands the scale of the model. Likewise, the Y-axis position was calculated by

$$YPOS_j = YOFFSET + YSCALE \times M_j$$

The best fit for a given model spectrum was determined by the variation of the four parameters until the least-mean-squares-difference was minimized and FIT was maximized. The agreement between the spectra was quite good except for a line at 8446Å which is an emission line produced by excitation of atmospheric atomic oxygen by auroral electron precipitation. This auroral line was not included in the synthetic spectra and the calculation of FIT ignored the data around this emission line.

One important consideration was that the wavelength of a specific data bin was not fixed. The computer was not driving the cam motor so there was an uncertainty of one bin position in the wavelength of each of the data array elements. It was critically important to adjust for this before calculating the temperature. This was done by adjusting the $XSCALE$ and $XOFFSET$ parameters before calculating the temperature of each data scan.

In addition to the temperature, the band intensity was calculated for each data record. The band intensity is the integrated intensity of all of the lines of the spectrum. It is easy to see that the intensity of the band is linearly proportional to the value of $YSCALE$. The linear factor, which was dependant on the absolute calibration, was calculated for one spectrum in the time series and then held constant throughout the data set.

Often the data was simply not of good enough quality to use for the determination of the rotational temperature or band intensity. The rejection criteria included a value

of *FIT* less than 0.8. This minimum *FIT* was determined experimentally to correspond to a relative uncertainty of approximately $\pm 2°K$ for most of the data. The uncertainty of the calibration resulted in an absolute uncertainty of $\pm 5°K$ but the calibration error was a systematic error and was constant over the time scales which are discussed here. The total error is assumed to be $\pm 5°K$ for all of the OH data presented in this thesis.

The data was discarded if the background scattered light was of the same magnitude as the intensity of the brightest line of the spectrum. This resulted in the rejection of data taken with a combination of clouds and full moon or when the solar depression angle was less than 6 degrees. The aurora also introduced contamination due to several very weak N_2 1st positive auroral emission lines that lie under the OH(6-2) band. The atomic oxygen line at 8446Å was a good indicator of auroral activity. The data were considered unusable, due to auroral contamination, if the 8446Å auroral line was more than twice the intensity of the neighboring OH $P_1 3$ line at 8465Å. Often the combination of aurora and twilight would make the data unusable. In this case the value of *FIT* was used as the limiting factor.

The use of these three criteria for rejecting data covered most of the possible problems that could arise, such as aurora, low signal, bright lights, and electronic noise. The results of the analysis were two time series, one of temperature and the other of intensity. The first figure in the next Chapter (Figure 3.1) shows a 36 hour time series of both temperature and intensity from the OH emission, observed from Svalbard during December, 1986. The top trace is temperature and the bottom trace is integrated band intensity.

2.3 Meridian Scanning Photometer

The Meridian-Scanning-Photometer system, or MSP, consists of five photometers,

each with tilting interference filters to scan in wavelength and a large rotating mirror, angled at 45°to the optical axis, to scan the meridian. The two MSP systems that were used in this study are part of existing auroral observatories at Longyearbyen, Svalbard (LYR) and Poker Flat, Alaska (PKR). The MSP at Svalbard is normally operated as part of the auroral campaigns which take place during the period around the winter solstice. The Fairbanks MSP is part of the Poker Flat Rocket Range research facility and is used primarily for rocket campaigns. There were times when it was possible to use one or two of the five MSP channels for the airglow observations needed for this study.

The MSP provides spatial information along the north-south geomagnetic meridian by scanning the fields of view of the photometers from horizon to horizon. Five photometers are mounted horizontally so that they pointed at the rotating mirror. Figure 2.6 shows the basic components of the MSP.

The light from the sky (airglow) is reflected by the mirror mounted at 45°on a motor driven shaft. As the mirror turned, it reflected the light from the magnetic meridian into the 5 photometers. The mirror rotated through 360°every four seconds.

Each of the interference filters is held in a computer driven, tilting device. The bandpass of an interference filter can be shifted towards shorter wavelengths by tilting the filter so that the incident light is not perpendicular to the surface of the filter. This is shown in Figure 2.7 where the basic principles of an interference filter are described. Tilting the filter is essentially changing the incident angle in Figure 2.7 and in this way, the bandpass (3Å at half transmission) of each filter may be tuned to include the wavelength of the emission of interest. The band pass of each filter is adjusted to be on and off the designated emission lines with each consecutive rotation of the mirror. Scans with the filter bandpass away from the emission line measure the background light. These scans are co-subtracted, point-by-point, from the scans which include the emission line. This allows for subtraction of the scattered background light, such as scattered
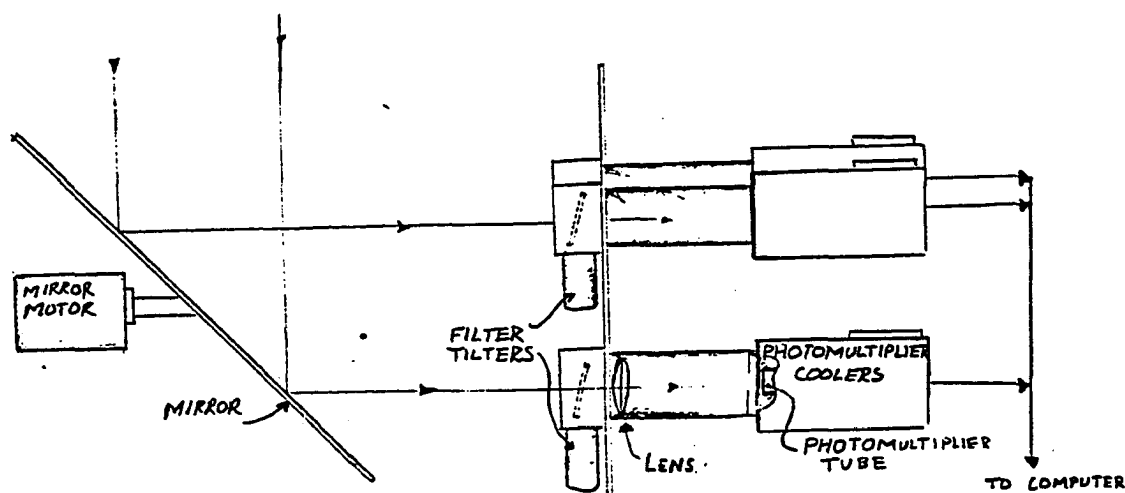
Fig. 2.6 Diagram of the components of the Meridian Scanning Photometer. The rotating mirror reflected the light from the sky onto the interference filters which are adjusted to allow only one emission line each to pass through to the photomultipliers. The rotation of the mirror resulted in a meridional scan from horizon-to-horizon.

sunlight, moonlight and other unwanted emissions. As well as a filter tilting mechanism, each photometer has a lens system and aperture which restricted the field-of-view of the photometers to 1°.

As the mirror rotates, the computer samples the pulses from the photometers at a rate of 90 samples per second while the mirror is pointed toward the sky, thus providing 1° spatial resolution. There are intensity calibration lamps and spectral lamps mounted below the mirror such that during the part of the rotation that the mirror point downward, the photometers are calibrated. As with the spectrometers, the MSP has cooled, GaAs Hamamatsu 942 detectors in a pulse counting mode. In an attempt to reduce the amount of stored data, two scans are summed together before the recording of the data
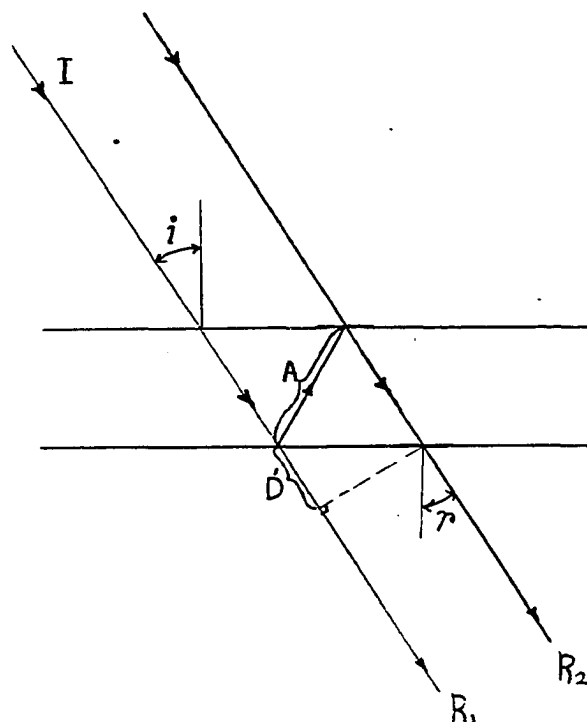
Fig. 2.7 Diagram of an interference filter. Constructive interference will occur when the path difference, D, is equal to an integer number of wavelengths (i.e. $n\lambda = D$ $n = 1, 2, 3, ...$). The wavelength of the reflected light is dependent on the the angle of incidence, i and the angle of reflectance, r. Note that at a given angle i, there will be waves of wavelength $\lambda = D/n$, where n is any integer. Thus, it will be necessary to isolate the desired wavelength with a broad band filter.

on tape. Thus, a complete 180° scan is recorded every 8 seconds. Since every other scan is a measurement of the background intensity, the best resolution possible is 16 seconds. For the airglow study, it was necessary to add several of these scans before the signal-to-noise ratio was high enough. The MSP system is described in more detail by *Romick* [1976].

2.4 MSP Data Analysis

For the airglow study described in this thesis, two of the photometers in the MSP were

fitted with OH interference filters. The bandpasses of the two filters were adjusted to include the $P_1 2$ and $P_1 4$ lines of the the OH (6-2) band at 8400Å and 8465Å respectively. The ratio of the intensity of these two lines is a function of the rotational temperature of the emitting OH molecule. Either channel could be used to provide spatial information on the OH intensity. By taking the ratio of the output of the two channels, it is theoretically possible to obtain the rotational temperature of OH as a function of time and of zenith angle. Unfortunately the signal-to-noise of the instrument is often inadequate to obtain useful temperatures. The observed temperature fluctuations were of the order of 10% of the average temperature. The ratio of the intensities of the $P_1 2$ and $P_1 4$ lines would thus, change by less than 3%. Since the intensity of the band goes through 50% fluctuations, and the statistical uncertainty of the measurements is considerable, the use of two OH lines to calculate temperatures proved to be unsatisfactory. Further refinements are nesessary before this technique will be usable.

The MSP is specifically designed for auroral observations which are usually much brighter than the OH airglow emissions. A single scan provided only marginal measurements of the airglow with a signal to noise ratio of about one. Since the noise is random and the signal is not, adding the scans is a simple means of increasing the signal-to-noise ratio.

The MSP data can be used to determine limited information on the horizontal structure of gravity waves. Since the MSP scans only in the geomagnetic meridian, the horizontal wavelength cannot be determined with this instrument alone. It is necessary to have at least three non-colinear points of measurement to determine the horizontal wavelength and propagation direction. Thus, the combination of the spectrometer with the spatial scanning mirror system and the MSP provides a good means of studying the horizontal structure of the airglow.

CHAPTER 3

Oscillations in the Airglow Brightness and Temperature

The effects of any atmospheric perturbation, such as gravity waves, on an emitting layer in the upper atmosphere may be described in terms of several different quantities which are measurable with optical observations. The emission intensity is perhaps the easiest to measure, but since there are so many contributing factors, it is the most difficult to interpret. The rotational temperature is more difficult to extract from the data, but fluctuations in temperature are better understood. The ground-based observations of emission spectra, used in this study, provided both the intensity of the airglow and the rotational temperature of the emitting molecule. The combination of OH and O_2 emission intensities and temperatures provided limited information on the vertical structure of the wave field. Finally, by modifying the instrumentation to scan in different directions, it was possible to measure the horizontal distribution of the fluctuations in temperature and intensity. This allowed us to determine horizontal wavelengths and horizontal propagation speeds.

3.1 Relative Amplitudes of Oscillations in Rotational Temperature and Band Intensity of the OH Airglow

In order to infer some of the basic properties of internal gravity waves, it is imperative that the interaction beween gravity waves and the airglow emissions be thoroughly understood. At the time of writing this thesis, there are only a few theoretical studies on the interaction between the airglow and gravity waves, and there are even fewer comparisons between theory and observations. It is the purpose of this chapter to compare

23

some of our observations of oscillations in the airglow emissions to those of the previous researchers who attributed their observed oscillations to internal gravity waves at mesopause heights.

There have been numerous studies which examine wave-like oscillations in the rotational temperature and intensity of the OH airglow. Some of the key papers include *Krassovsky* [1972], *Krassovsky and Shagaev* [1973], [1974a] [1974b], *Krassovsky and Shefov* [1976], *Sivjee et al.* [1972], *Myrabø et al.* [1983], and *Sivjee et al.* [1987]. These studies involved single direction measurements.

In order to quantify the effects of gravity waves on the OH airglow, *Krassovsky* introduced a quantity called η, defined as the ratio of the fractional amplitude of oscillation of the brightness of the emission to that of the rotational temperature. In other words, $\eta = \frac{\delta I / \bar{I}}{\delta T / \bar{T}}$ where δ is the fluctuation amplitude and the *overbar* indicates the average of the quantity. *Krassovsky* [1972] calculated that η should be on the order of one. His observations however, did not agree well with his prediction. Other observations such as those by *Hamwey* [1986], *Sivjee et al.* [1987], and *Hecht et al.* [1987] have also observed different η values ranging between one and five.

Our observations have also included measurements of brightness and rotational temperature. An example of oscillations in the airglow emissions is shown in Figure 3.1 where the top trace is the OH rotational temperature and the bottom curve is emission brightness, or intensity. The thickness of the two curves represents the uncertainty in the measurements. Any fluctuation which has an amplitude less than the uncertainty is considered insignificant. There are two wave-like oscillations during the 36 hour period shown in Figure 3.1, one begining at 20:00 UT on day 362 and the other begining at 18:00 UT on day 364. Both have similar periods of about 2.2 hours.

In the example shown in Figure 3.1, the oscillations in intensity are on the order of 20% of the average intensity. The temperature fluctuations, on the other hand, are only

LYR OH DEC. 28-29 1986
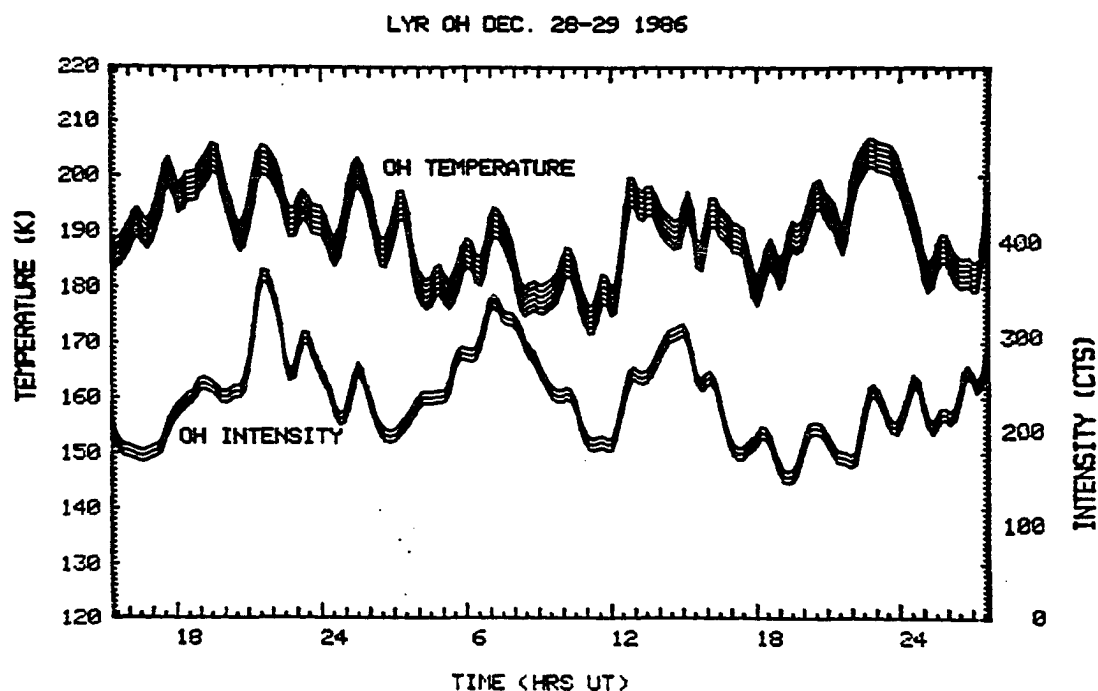
Fig. 3.1 Thirty six hours of OH emission rotational temperature (top) and integrated band intensity (bottom), both calculated as functions of time showing several wavelike oscillations. The thickness of the curves represents the uncertanty in the measurements. The data were acquired from Svalbard, Norway in December of 1986. Note the two wave packets, the first beginning at 20:00 on December 28 (day 362) second at 18:00 UT on December 29 (day 363). Both waves have periods of approximately 2.2 hours.

about 5% of the average temperature. The value of η, as defined by *Krassovsky*, would be $\eta = (20\%/5\%) = 4$. This does not agree with the value of one that was calculated by *Krassovsky* [1972], but it does agree with the value predicted by *Hamwey* [1986].

Another example of wave-like oscillations can be seen in Figure 3.2. In this case, the period of oscillation is on the order of 15 minutes and the temperature fluctuations (top trace) are larger than the intensity fluctuations. The amplitude of the temperature fluctuations is again about 5% while the intensity fluctuations are less than 5%, which is much less than the 20% of the previous figure. In this case the value of η is less

PKR OH SEPT 13,1987
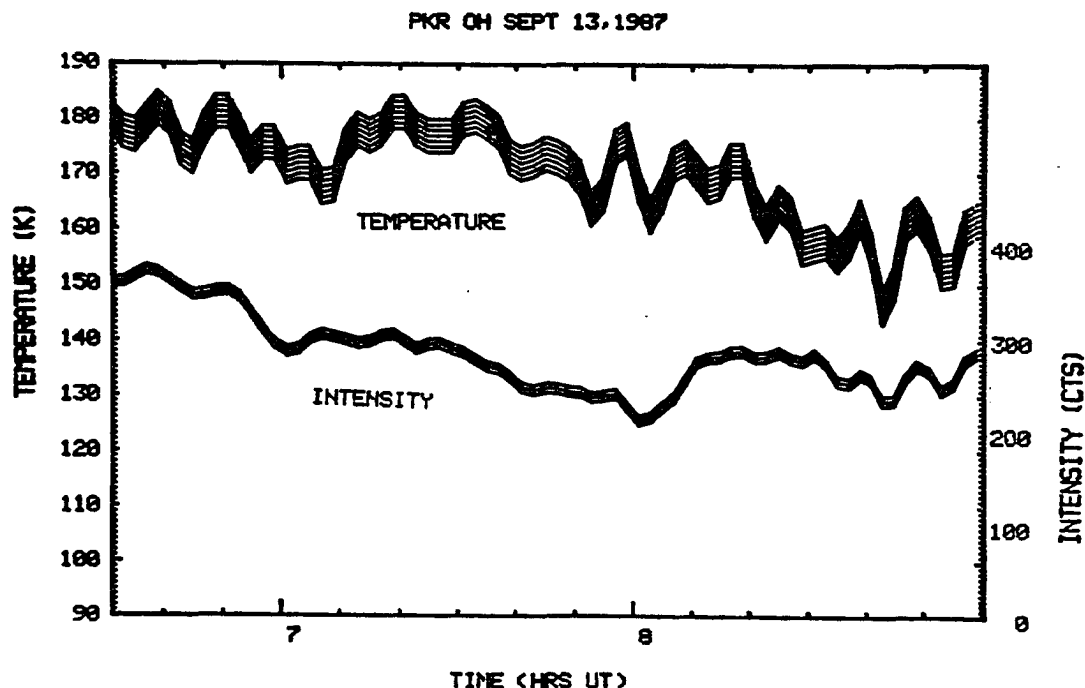
Fig. 3.2 Same as Figure 3.1 but the 2.5 hours of data in this Figure were taken at Poker Flat Research Range on September 13, 1987 and show oscillations with periods of about 10-15 minutes. The thickness of the two curves represents the uncertainty in the measurements. Any fluctuation which has an amplitude less than the uncertanty is considered insignificant. Note that the relative amplitude of the intensity fluctuation is much less than those in Figure 3.1. In this example, the value of the parameter η is less than one.

than one which does not agree with either *Krassovsky* or *Hamwey*. From the examples shown in Figure 3.1 and 3.2, it is clear that the relative amplitudes of the oscillations in temperature and intensity are not constant and may depend on the period of the wave.

Figure 3.3 shows another wave-related phenomenon. As in Figure 3.1, the top trace is temperature and the bottom trace is intensity. In this 12 hour segment, observed from Svalbard, there are two obvious wave periods present. The first is a 2.5 hour oscillation, which is a slightly longer period than in the example in Figure 3.1. There are also secondary wave packets with shorter periods, of approximately 30 minutes, embedded in

LYR OH DEC. 28, 1986
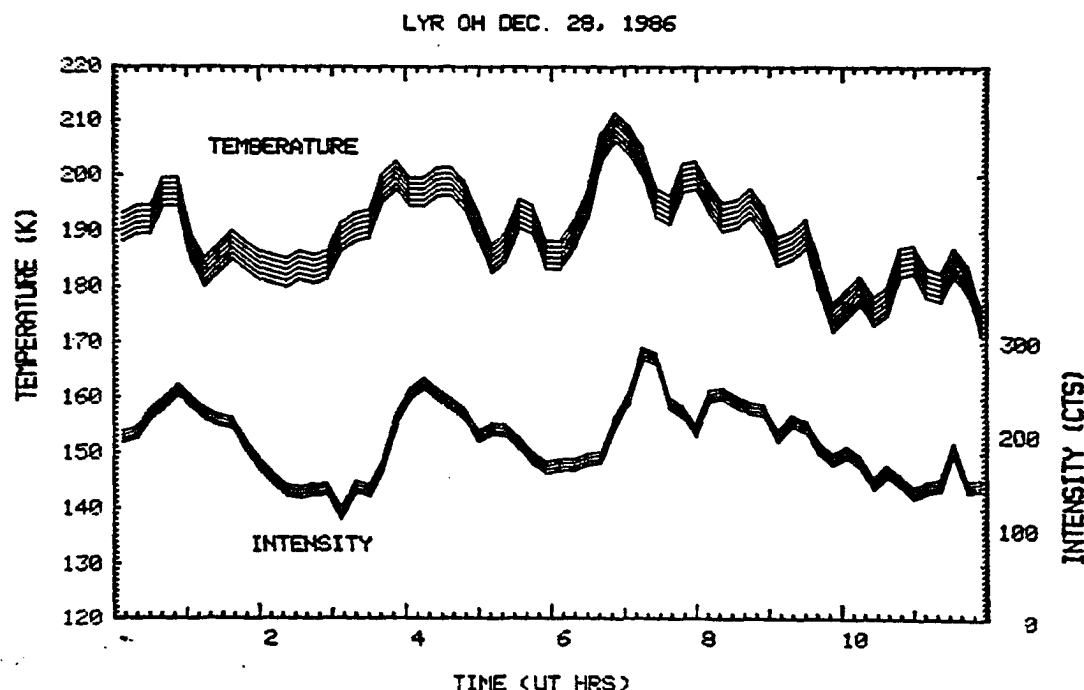
Fig. 3.3 Same as Figure 3.1 but the 12 hours of data in this Figure are from Svalbard on December 28, 1986 and show two different wave periods. There are both long and short period oscillations present in this data set. The large wave period is about 2.5 hours, which is similar to Figure 3.1. The smaller waves have approximately 30 min. periods and they occur only during the decreasing phase of the larger wave. The relative amplitudes are similar to those in Figures 3.1 and 3.2 and result in values of $\eta = 4$ for the long period wave and $\eta = 1$ for the shorter wave.

the decreasing phase of each of the long period waves. It is interesting to note that the long period waves no longer have the sinusoidal appearance as in the waves in Figure 3.1. In this example, the intensity goes through a rapid increase during the first part of the wave. The decreasing phase of the intensity wave is much more gradual and there are short period wave packets as well during this phase of the wave.

One should note that the relative amplitudes of the oscillations in intensity and temperature are similar to those of the first two figures. The long period waves in Figure 3.3 have wave amplitudes of approximately 40% and 10% for the intensity and

temperature respectively, which gives a value of $\eta = 4$. The shorter wave amplitudes are 10% for both the intensity and temperature, which results in $\eta = 1$. Again the values of η seem to be dependent on the period of the wave with larger η values for larger wave periods. This phenomenon of changing ratios, between wave amplitudes in intensity and temperature, is important, and it will be shown that the ratio of these amplitudes can be used to identify other gravity wave parameters.

3.2 Relative Amplitudes of the Oscillations in the Intensity and Temperature of the O_2 Airglow.

The O_2 airglow responds somewhat differently to the passage of gravity waves than does the OH airglow. There are similar oscillations in both temperature and intensity of the O_2 emission but the relative amplitudes of the O_2 intensity and temperature are not the same as for the OH emission. For instance, the amplitude of the 45 minute oscillations in intensity of O_2, in Figure 3.4 are less than 10% of the average while the temperature fluctuations are on the order of 3% of the average temperature resulting in a value of $\eta < 1$. This example also shows a wave with a period of more than 6 hours with intensity and temperature amplitudes which yield a value of $\eta \simeq 5$.

Thus the oscillations in the O_2 airglow temperature and intensity are similar to the oscillations observed in the OH emissions even if the derived parameters are different. Since these emissions come from two different altitudes, the similarities between the OH and O_2 airglow emissions can be used to study the vertical propagation of gravity waves.

3.3 Similarities in the OH and O_2 Emission; Indications of Vertical Structure

Noxon [1978] observed both OH and O_2 temperatures to try and determine the vertical structure of gravity waves. He found that there were, at times, correlated waves

LYR O2 JAN. 10, 1986
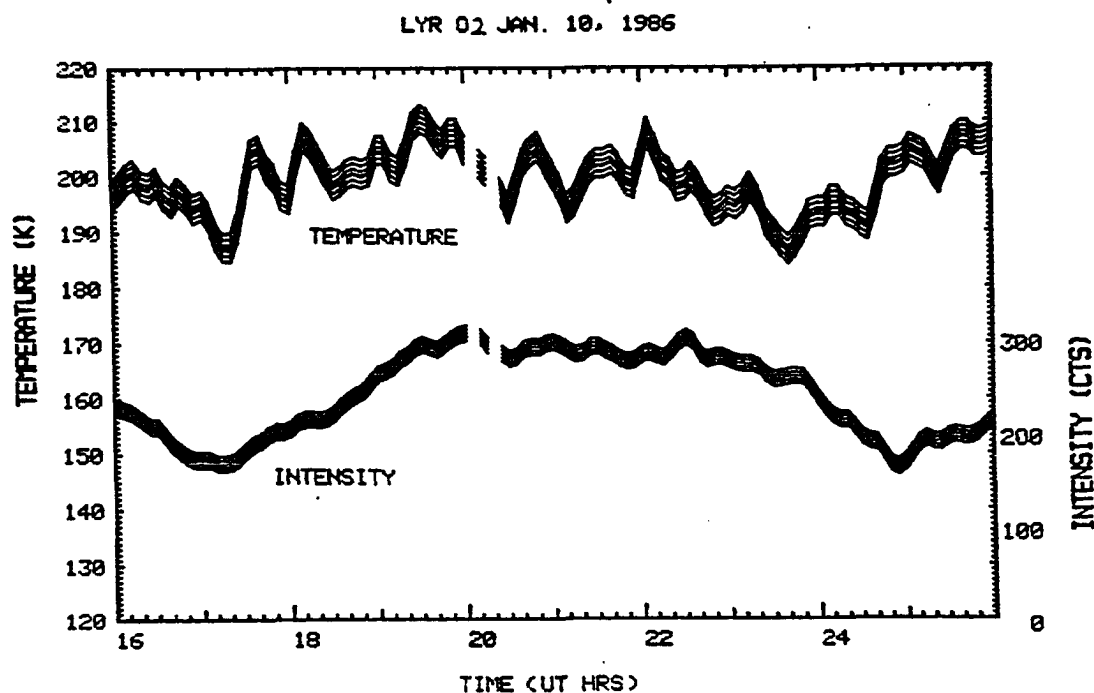
Fig. 3.4 Oscillations in O_2 temperature and intensity as observed from Svalbard in January of 1986. There are two oscillations present in this data set, one with a 45 minute period and a value of $\eta < 1$, and the other with a 6-8 hour period and a value of $\eta \simeq 5$.

in the OH and O_2 temperatures. He also found that there was a lot of variability in the ratio of the amplitudes of the fluctuations in temperatures of the two emissions. *Noxon's* study concluded that OH and O_2 emissions could indeed be used for analysis of gravity waves in the upper mesosphere and that the use of two emissions instead of one could add significantly to the understanding of propagation and the vertical profile of gravity waves.

Noxon [1978] did find some correlation between the oscillations in the rotational temperatures calculated from the two emissions. He determined that there was phase shift of one to two hours between the OH and O_2 emissions with the O_2 leading. This would indicate a downward propagating phase with a vertical phase speed of about 2.8

m/s. The downward propagating phase is a characteristic of most gravity waves, as will be shown in the next chapter.

There have been many other attempts to measure the vertical structure of gravity waves. The wave-like oscillations in *Noxon's* data do not have well defined wave structure, and thus it is difficult to determine the wave period accuratelly enough to calculate the vertical wavelength of the waves. According to liar measurements by *Gardner and Voelz* [1986], the vertical wavelength of gravity waves is directly correlated with wave period as can be seen in Figure 3.5a. *Meek et al.* [1986] made similar measurements with an MST radar and found that the vertical wavelength is inversely proportional to the wave period as can be seen in Figure 3.5b. *Smith* [1985] also used an MST radar but he found a different relationship between wave period and vertical wavelength (see Figure 3.5b). The three data sets shown in the two plots in Figure 3.5 show three different relationships between the wave period and the vertical wavelength. It should be noted that the optical measurements of *Gardner and Voelz* [1986] do not account for Doppler shifting of the wave period due to the mean wind. It is unlikely however that this could account for the differences between the optical and radar measurements.

One possible cause for this discrepancy could be the different techniques for obtaining the data. Both the *Meek et al.* [1986] study and the *Smith* [1985] study were based on radar measurements which are dependent on electron densities. The study by *Gardner and Voelz* [1986] was based on lidar measurements, which are dependent on the density of the neutral atmosphere. It is possible that the two techniques do not measure the same phenomenon.

Our measurements can also provide information on the vertical wave field. The OH and O_2 emissions provide temperature information at $\sim 87km$ and $\sim 95km$ respectively. This results in a vertical separation of $8km$. If the vertical separation between these emitting layers ($\sim 8km$) is larger than the vertical wavelength, λ_z, it will be difficult
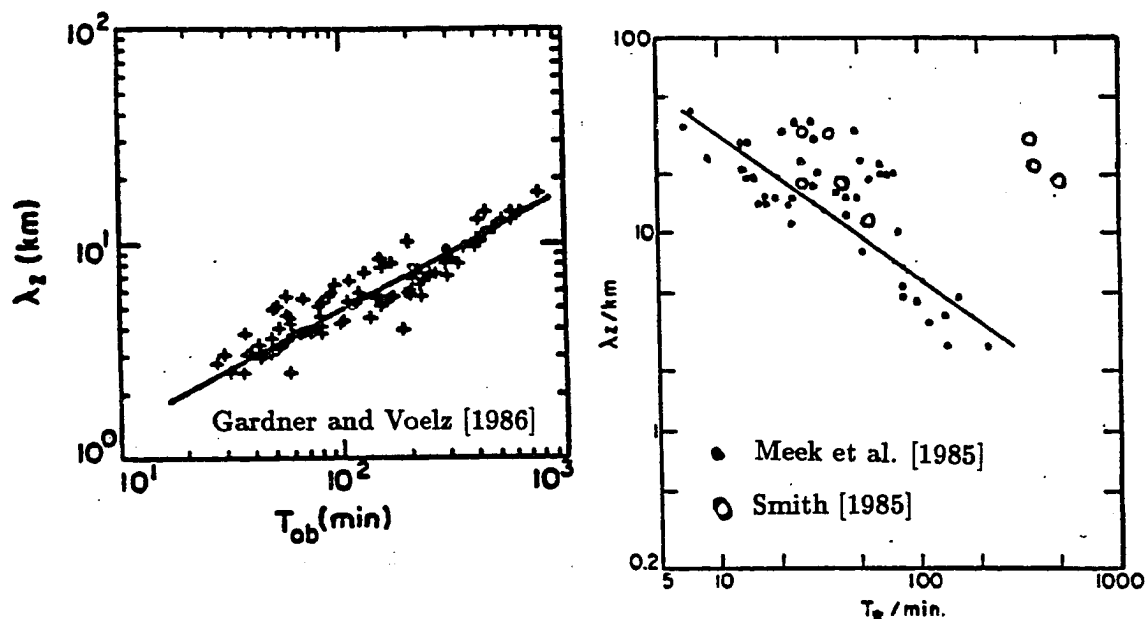
Fig. 3.5   Previously observed relationships between the vertical wavelength of gravity waves and the wave period. a) The observations by *Gardner and Voelz* [1986] based on lidar measurements. b) The observations by *Meek et al.* [1986] (dots) and *Smith* [1985] (open cicles). It is obvious that there is little agreement between the measurements.

to follow a single wave as it passes through both layers. Only when $\lambda_z > 8km$ will the vertical wavelength be definable. The phase between the fluctuations in the two emissions can be used to determine the vertical wavelength of the gravity waves, if the same wave can be identified in each of the layers. Figure 3.6 is an example of two temperature time series of OH and O_2 rotational temperatures. A constant 20°K was subtracted from the O_2 trace in order to display the relation between the variations. There are several wave-like oscillations in the data set. If the phase angle θ between the waves is zero and the vertical wavelength λ_z is smaller than the separation between the layers (8 km) then
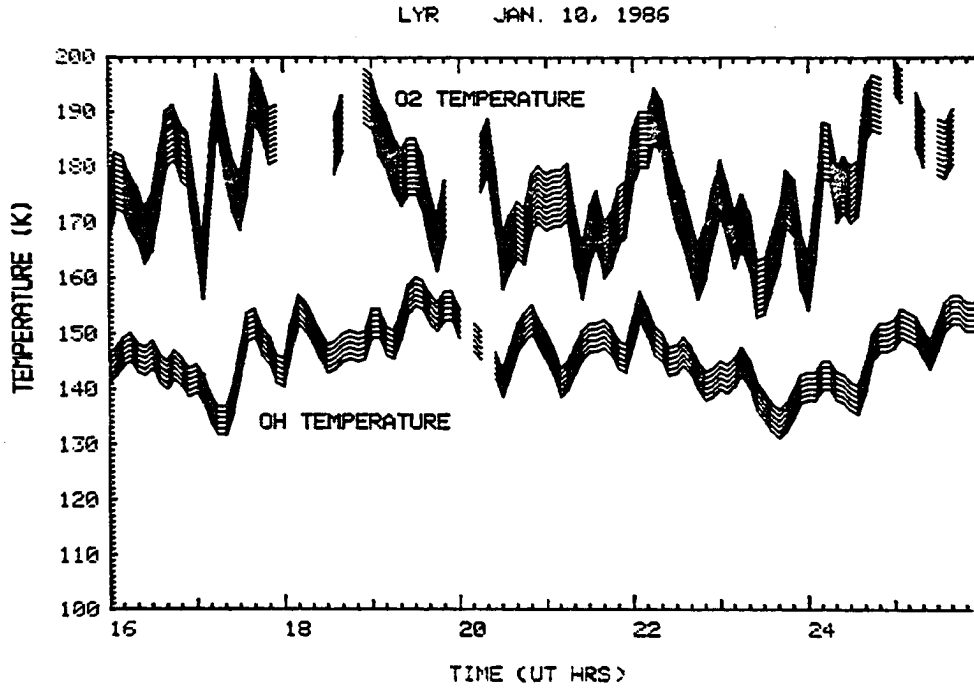
Fig. 3.6 Two time series of temperature from the OH ($85km$) and O_2 ($95km$) airglow emissions. The data sets were separated by 20°K for display purposes. These time series were compared using cross-correlation techniques to determine the vertical structure of propagating gravity waves.

the wavelength, λ_z, must satisfy the equation,

$$n\lambda_z = 8km \qquad n = 1,2,3,\cdots.$$

for $\lambda_z < 8km$. On the other hand, if $\lambda_z > 8km$, then the phase angle defines the wavelength such that

$$\lambda_z = \frac{2\pi 8km}{\theta}.$$

When the phase angle between the OH and O_2 is calculated as a function of frequency, the vertical wavelength can be inferred. Figure 3.7a shows the phase angle between the OH and O_2 temperature fluctuations as a function of wave period. The short period waves are not absolutely defined, since the vertical distance between the

two emissions is greater than the vertical wavelength. There does seem to be a repeated trend in the data. This would then imply a relation between the frequency of the wave and the vertical wavelength λ_z. Each time the phase changes from $+180°$ to $-180°$, one more wavelength is fit between the layers. The phase can be converted to vertical wavelength as described by the above equations. The results can be plotted as a function of period as seen in Figure 3.7b where it was assumed that the vertical wavelength for the long period waves is larger than the vertical separation of the layers and that each time the phase angle passed through $180°$, the number of wavelengths between the layers increased by one. It is clear that our observations agree well with those of *Gardner and Voelz* [1986].

It should be pointed out at this time that the above example is a special case. There are numerous examples that do not have as clear a phase relationship as above, but there is almost always some sort of non-random relationship between the phase in OH and O_2 temperatures as a function of frequency.

3.4 The Horizontal Structure of Oscillations in the OH and O_2 Airglow Intensity and Temperature

One of the best examples of the effect of gravity waves on the airglow layer has been the TV and photographic records of the horizontal distribution of airglow intensity [*Peterson and Kieffaber*, 1973; *Moreels and Herse*, 1977]. The time resoluton was not adequate to observe the horizontal propagation of the waves, however; improvements in modern imaging systems have shown the possibility of studying gravity wave production and propagation using the airglow [*Taylor*, 1986]. In order to develop the theory of the interaction of gravity waves with the airglow, it will be necessary to observe the horizontal
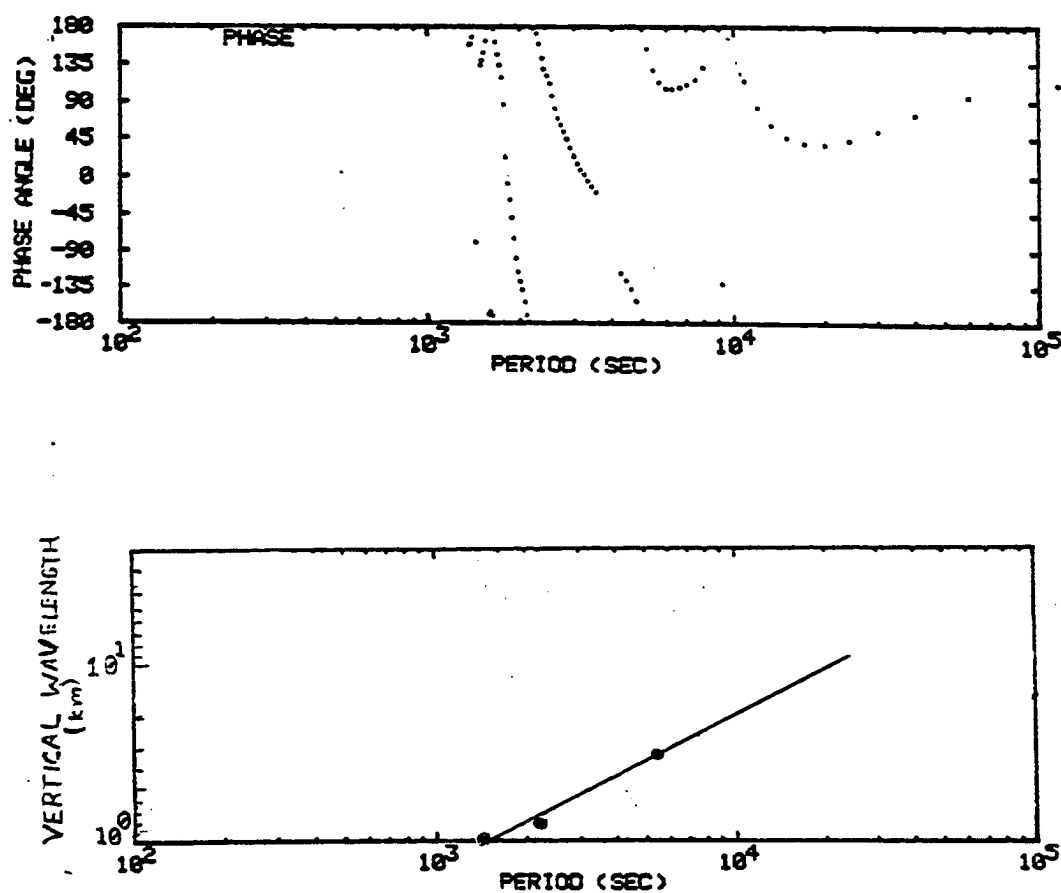
Fig. 3.7 Two plots showing phase between the temperature at 87km and 95km a) and the vertical wavelength b) calculated from the phase. There is often too much uncertainty in measuring wavelengths of 1-2 km with points separated by 8 km, but it is clear that in this example there is some sort of relationship between the wavelength of the wave and the wave period.

extent of both the temperature and intensity with a time resolution of approximately 5 minutes.

Several methods were used in this study to examine the horizontal structure of the OH and O_2 airglow. The first method involved scanning the field of view of the spectrometer around the sky by way of a mirror (see Figure 2.3). The mirror system allowed us to get measurements from the three different directions with a time resolution of 6-9 minutes per total revolution. The mirror was set to point in the geomagnetic directions of north, south, and east, at an elevation of 65°above the horizon.

Once the spectrometer data were separated into the three directions, the time series of temperature and intensity were analyzed for waves and other common features, as can be seen in Figure 3.8. The propagation direction and velocity of the mesopause region gravity wave disturbances could be calculated from the data set. In the example in Figure 3.8 it was determined that the long period waves observed in the intensity traveled from an azimuth angle of 180°(where 0°is geographic north) with a horizontal propagation velocity of 60 m/s. The shorter period waves traveled in a similar direction with a similar velocity. This example and several others will be discussed in Chapter 6.

Another method of studying the horizontal structure of oscillations in the airglow is with the MSP. This instrument is able to obtain a spatial image in one dimension and still yield temporal information with one minute resolution. Figure 3.9 shows the MSP data for the same period as in Figure 3.8. In Figure 3.9, the X-axis is time, the Y-axis is horizontal distance along the geomagnetic meridian and the intensity of the emission is represented by the whiteness of the plot. The wavelike structures in brightness can be seen to propagate northward in Figure 3.9. The meridional horizontal velocity can be calculated to be about 50 m/s and the horizontal wavelength is about 200 km. This is confirmation of wavelength of the same waves observed with the spectrometer data and mirror system. Detailed analysis of this and several other examples will be postponed
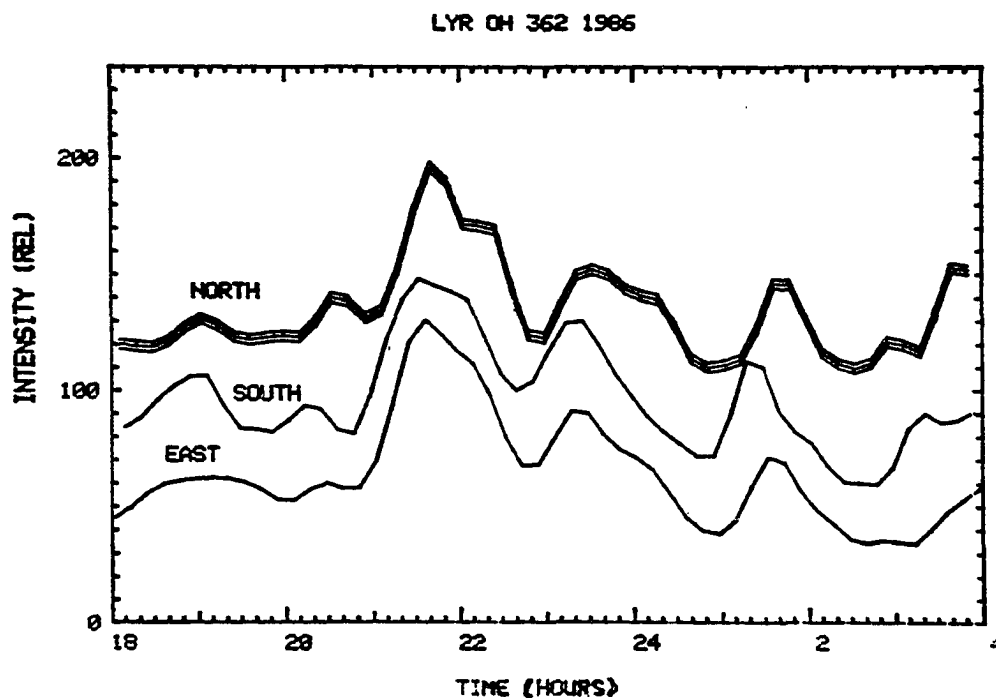
Fig. 3.8   Time series of OH intensity emission as observed in the geomagnetic directions of north, south, and east. The thickness of the top curve represents the uncertanty of the measurements and is the same for the other two curves. The wave in this example propagated from the south with a phase velocity of 60 m/s.

until after the discussion of the theoretical response of the airglow emissions to gravity waves.

3.5 Semidiurnal Oscillations in the OH and O_2 Airglow

Another example of wave related phenomena is the semidiurnal oscillations which are observed at high latitudes during the polar night, as in Figure 3.10. These oscillations are observed in the temperatures and in the airglow intensities of both the OH and O_2 emissions and they cannot be explained by classical solar tidal theory [*Walterscheid et al.* 1986]. Since atmospheric tides are the products of diurnal heating of the atmosphere by solar radiation, it is difficult to explain such strong tidal modes at 78° north geographic
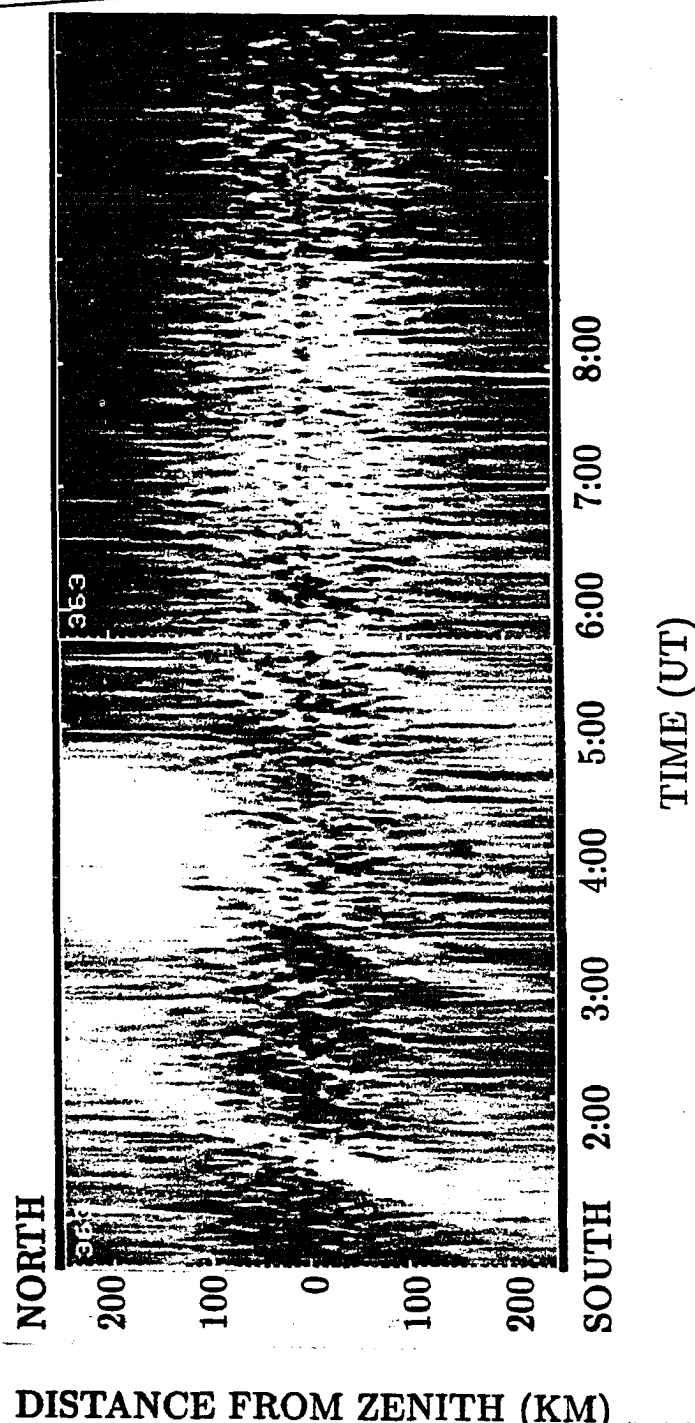
Fig. 3.9 10 Grayshade plot of OH airglow intensity as a function of meridional distance and of time for the same period as Figure 3.8. The X-axis is time, the Y-axis is horizontal distance, and the intensity of the airglow is represented by the grayshade. The wave is seen as diagonal stripes in the grayshade.
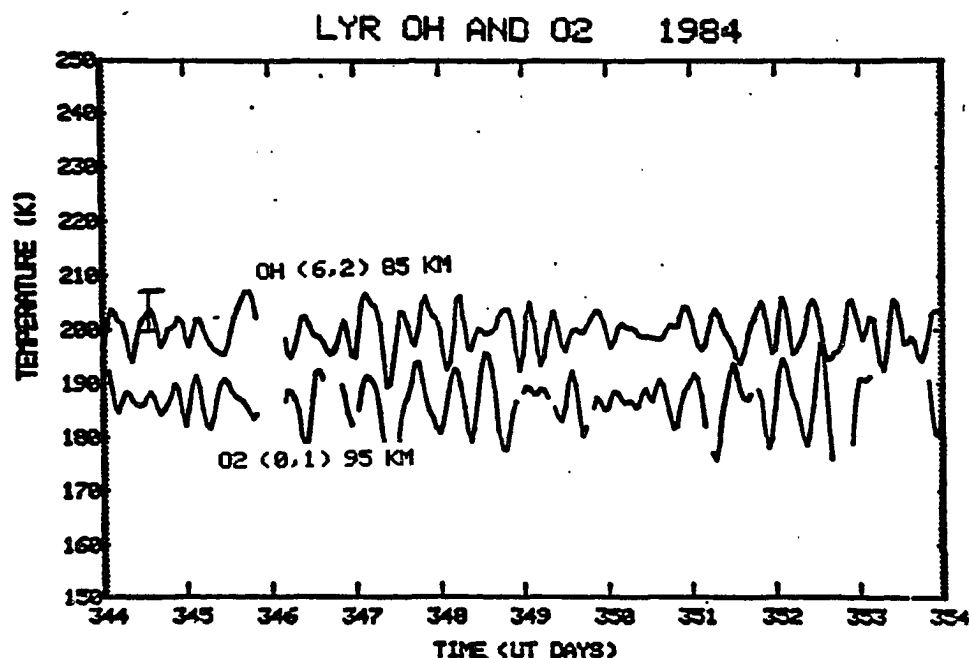
Fig. 3.10 Semidiurnal oscillations in the temperatures at 85 km and 95 km from the OH and O_2 airglow emissions respectively. The offset between the two is added for display purposes. The data set has been filtered to enhance the semidiurnal, or 12 hour, oscillations.

latitude during the polar night. During the two and a half months around the winter solstice, there is no sunlight on Svalbard. Thus, there is no local diurnal heating of the atmosphere and the observed tidal modes must have either propagated northward for several thousands of kilometers or they are a result of some secondary process related to the atmospheric tides. *Walterscheid et al.* [1986] theorized that these semidiurnal oscillations could be a product of tidal wave-gravity wave interactions. These semidiurnal oscillations were observed in the OH airglow by *Myrabø* [1984] and by *Sivjee et al.* [1986] and in the O_2 airglow by *Myrabø et al.* [1986].

It is possible that these semidiurnal osillations are tidally driven gravity waves. The inertial period for wave motion (longest period for gravity waves) is approximately 13.5

hours at polar latitudes [*Holton* 1979]. Thus, a periodic driving force, such as the solar driven atmospheric tides, could conceivably produce gravity waves or tides in the first harmonic. This would result in gravity waves with a twelve hour period. It should be noted that the amplitude of the oscillations in the O_2 temperature at 95 km is only about 10-20% larger than in the OH temperature at 87 km. Since gravity waves increase in amplitude with a decrease in density (as will be shown in the next chapter) one would expect somewhat larger amplitudes in the O_2 temperature fluctuations. This implies that either the semidiurnal oscillation is not a true gravity wave or that the gravity wave, with a semidiurnal period of oscillation, is undergoing dispersion such that the amplitude remains constant as the wave propagates upward.

CHAPTER 4

Theoretical Considerations

Harmonic motions in the atmosphere arise from the interaction of at least two opposing forces upon parcels of air. The scale of atmospheric oscillations ranges from 10^{-4} to 10^7 meters with oscillation periods between 10^{-6} and 10^6 seconds (10 days). Sound waves make up the high frequency end of the spectrum and the restoring force is due to pressure gradients. *Gravity waves* are waves which include the earth's gravity as one of the restoring forces. Gravity waves can be classified into two categories. *Surface* gravity waves are those which propagate at the surface of, or the interface between, two different media, such as water waves. *Internal* gravity waves propagate internally in the medium. It is the second of these that will be discussed in the remainder of this chapter.

This chapter will be devoted to the discussion of general gravity wave theory and the interaction of gravity waves with the airglow. A considerable portion of the airglow discussion will focus on the work of *Waltersheid et al.* [1987] and modifications to this work by *Hickey* [1987a,b].

4.1 Atmospheric Oscillations in the Presence of Gravity

The following derivation of gravity waves is taken in part from *Houghton* [1986], *Holton* [1979], and *Smith* [1985], as well as *Fritts* (private communication). It is possible to derive all of the wave motions of the atmosphere from the equations of fluid motion. The three equations are

$$\text{Momentum:} \qquad \rho\frac{d\mathbf{U}}{dt} = -\rho2(\mathbf{\Omega} \times \mathbf{U}) - \nabla p + \rho\mathbf{g} + \nu\nabla^2\mathbf{U} \qquad 4.1$$

$$\text{Continuity:} \qquad \frac{d\rho}{dt} = -\rho\nabla \cdot \mathbf{U} \qquad 4.2$$

$$\text{Energy:} \qquad \frac{d\theta}{dt} = 0 \qquad 4.3$$

where: $\mathbf{U}$ is the velocity vector

$2(\mathbf{\Omega} \times \mathbf{U})$ is the Coriolis acceleration

p is pressure

ρ is density

$\mathbf{g}$ is gravitational acceleration

ν is kinematic viscosity

θ is potential temperature

t is time.

The bold-face indicates vector quantities. In order to follow convention, the velocity vector components are labeled u, v, and w for the rectangular coordinates of $\hat{x}, \hat{y}$, and $\hat{z}$, such that $\mathbf{U} = (u, v, w)$ and the components are directed eastward, northward and upward.

The first term in each of the equations is the total time (or advective) derivative of some quantity. In the first two equations, the advective derivative will be replaced by the set of partial derivatives such that $\frac{d}{dt} = \frac{\partial}{\partial t} + u\frac{\partial}{\partial x} + v\frac{\partial}{\partial y} + w\frac{\partial}{\partial z}$. The right side of the momentum equation represents the driving forces: the Coriolis effect, the pressure gradient, the gravitational force, and a viscosity term. The Coriolis term can also be separated into component form. The vertical component is negligible compared

41

to the pressure gradient and gravitational forces, and the horizontal components can be rewritten as $-fv$ and fu, where $f = 2\omega \sin \phi$ is known as the Coriolis parameter. It should be noted that the Coriolis parameter has the units of inverse time and it will be shown that this is the lower limit for gravity wave frequencies. Since the mean free path in the mesosphere is much less than the scale of most gravity wave motions, the viscous damping will be relatively small. To obtain a first order solution, we will drop the viscosity term altogether. It will be shown later that this step may lead to oversimplified conclusions.

In order to further simplify the calculations, it is acceptable to assume that the atmosphere is an incompressible fluid (i.e $d\rho/dt = 0$). The potential temperature can be written as

$$\theta = T(\frac{p_o}{p})^\gamma$$
$$= \frac{p}{\rho R}(\frac{p_o}{p})^\gamma$$

4.4

where $\gamma = c_p/c_v$ is the ratio of the specific heats and R is the ideal gas constant. By taking the total derivative of Equation 4.4, and applying Equation 4.3, it is possible to obtain

$$\frac{1}{c_s}\frac{dp}{dt} = \frac{d\rho}{dt} = 0$$

where $c_s^2 = \gamma RT$ is the sound speed.

The next step is to separate the momentum equation into $\hat{x}, \hat{y}$ and $\hat{z}$ components

and solve for the unknown quantities. The fluid equations become

$$\rho\left(\frac{\partial u}{\partial t} + u\frac{\partial u}{\partial x} + v\frac{\partial u}{\partial y} + w\frac{\partial u}{\partial z}\right) - \rho f v = -\frac{\partial p}{\partial x}$$

$$\rho\left(\frac{\partial v}{\partial t} + u\frac{\partial v}{\partial x} + v\frac{\partial v}{\partial y} + w\frac{\partial v}{\partial z}\right) + \rho f u = -\frac{\partial p}{\partial y}$$

$$\rho\left(\frac{\partial w}{\partial t} + u\frac{\partial w}{\partial x} + v\frac{\partial w}{\partial y} + w\frac{\partial w}{\partial z}\right) = -\frac{\partial p}{\partial z} - \rho g .$$

$$\frac{\partial u}{\partial x} + \frac{\partial v}{\partial y} + \frac{\partial w}{\partial x} = 0$$

$$\frac{\partial \rho}{\partial t} + u\frac{\partial \rho}{\partial x} + v\frac{\partial \rho}{\partial y} + w\frac{\partial \rho}{\partial z} = 0$$

The five fluid equations can be solved using the linear perturbation method. It is assumed that each of the quantities can be separated into a mean and a perturbation part. For example the x component of the velocity would then be expanded as $u(x,y,z,t) = u_o(x,y,z,t) + u'(x,y,z,t)$ where u_o is the average quantity and u' is the perturbation quantity. After substitution into the fluid equations, the results can be separated into mean and perturbation equations with the solution of the mean equations producing the geostrophic relation, $fU = -\rho_o^{-1}\partial p_o/\partial n$, and hydrostatic equation, $\rho_o^{-1}(dp_o/dz) = -g$, where n is normal to the flow direction. These two equations describe the steady state of the atmosphere.

The assumption of hydrostatic balance will allow us to set the remaining horizontal derivatives of the mean horizontal velocities as well as the mean vertical velocity to zero. By assuming a steady state, the time derivatives of the mean quantities will be zero as well. Also, any terms involving the products of two perturbation quantities have been assumed to be small, as is standard for obtaining a linear solution. It should be noted that, to a good approximation, the mean horizontal wind varies much more slowly than the perturbation quantities. Thus,

$$\frac{\partial u_o}{\partial t} \ll \frac{\partial u'}{\partial t}$$

Without loss of generality, it is possible to rotate the coordinate system such that the wave propagates in the x-z plane. Thus all derivatives with respect to y will be zero.

After elimination of all of the negligible quantities, the fluid equations finally reduce to a set of four equations and four unknowns.

$$\rho_0\left(\frac{\partial u'}{\partial t} + u_0\frac{\partial u'}{\partial x} + w'\frac{\partial u_0}{\partial z}\right) + \frac{\partial p'}{\partial x} - \rho_0 f v' = 0$$

$$\rho_0\left(\frac{\partial w'}{\partial t} + u_0\frac{\partial w'}{\partial x}\right) + \rho' g + \frac{\partial p'}{\partial z} + \rho_0 f u' = 0$$

$$\frac{\partial \rho'}{\partial t} + u_0\frac{\partial \rho'}{\partial x} + w'\frac{\partial \rho_0}{\partial z} = 0$$

$$\frac{\partial u'}{\partial x} + \frac{\partial w'}{\partial z} = 0$$

The perturbation quantities are assumed to be sinusoids of the form

$$u' = A\exp\left[i(kx + mz - \omega t)\right].$$

As a result of this assumption, the derivatives in space and time can be replaced by coefficients that are linear in x, z, and t. In other words,

$$\frac{\partial u'}{\partial x} = iku' \qquad \frac{\partial u'}{\partial z} = imu' \qquad \frac{\partial u'}{\partial t} = -i\omega u'.$$

After replacing the partial derivatives, the fluid equations can be solved for one of the variables. Solving for the vertical velocity, w', yields

$$\frac{\partial^2 w'}{\partial z^2} + \frac{1}{\rho_0}\left(\frac{\partial \rho_0}{\partial z}\right)\frac{\partial w'}{\partial z} + k^2\left[\frac{N^2 - \beta^2}{\beta^2 - f^2}\right]w' = 0. \qquad\qquad 4.5$$

where $N = g\theta_z/\theta = (g/T)(T_z + g/c_p)$ is the Brunt-Väisällä frequency and c_p is the specific heat. From a stationary observer's point-of-view, the wave will have a Doppler-shifted frequency $\beta = \omega - (\mathbf{k}\cdot\mathbf{U}_0)$ proportional to the speed of the mean wind $\mathbf{U}_0$. It is important to remember this point since, at high altitudes, the wind speed, u_0, and the phase speed, c_{phase}, can be of similar magnitudes. In which case, the Doppler-shifted frequency may be significantly different from the actual wave frequency.

One way to analyze the resulting waves is to solve Equation 4.5 for the vertical wave number, m which will have both a real and imaginary part such that

$$m^2_{real} = k^2 \left[\frac{(N^2 - \beta^2)}{(\beta^2 - f^2)} \right] - \frac{1}{(4H^2)}$$

$$m_{imag} = -\frac{1}{2H}$$

where H is the scale height, $H \equiv R\overline{T}/(g + R\overline{T}_z)$. The imaginary part results in exponential growth in the amplitude of the wave as it propagates upward. After some simplification, it can be seen that the real part of m will be positive if and only if $f < \beta < N$. This sets the upper and lower limits for gravity wave frequencies such that the intrinsic gravity wave frequency is less than the inertial frequency, f (which corresponds to a period of $\simeq$ 13.2 hours for the high latitude mesopause), and greater than the Brunt-Väisällä period, N ($\simeq$ 5 min.).

The next assumption is that the waves are *hydrostatic*. This implies that the accelerations are sufficiently small that $\frac{\partial p'}{\partial z} \sim 0$ implies that the vertical wavelength of the wave is much smaller than the horizontal wavelength, or that $m \ll k$. The result is that the equation for the vertical wave number, m, reduces to

$$m^2 = \frac{N^2}{(c-u)^2} \qquad \text{or} \qquad m = \pm \frac{N}{(c-u)}.$$

The sign of m can be determined by considering the group velocities, $d\omega/dk$ and $d\omega/dm$. The previous equation can be rearranged to yield

$$\omega = k(u \pm (N/m))$$

The phase and group velocities are

	Phase Velocity	Group Velocity
Horizontal	$\omega/k = u \pm (N/m)$	$d\omega/dk = u \pm (N/m)$
Vertical	$\omega/m = (k/m)(u \pm (N/m))$	$d\omega/dm = \mp kN/m^2$

For an upward traveling wave, the lower sign is chosen. This implies that for upward energy, or group propagation, the phase velocity is downward. It is very unlikely for the vertical group velocity to be downward since the increase in density of the atmosphere results in a decrease in the wave amplitude. Thus the phase fronts of a gravity wave should propagate downward. It should also be noted that the horizontal phase and the horizontal group velocities are in the same direction.

To a first order approximation, the amplitude of internal gravity waves will increase with height. This is due simply to conservation of energy [*Hines*, 1960]. The density of the atmosphere, ρ, is proportional to $\exp[-z/H]$. The energy of the wave is proportional to $\rho\omega^2 a^2$, where a is the wave amplitude. If energy is conserved, then $a \propto \sqrt{\rho}$. In the case of the OH and O_2 airglow layers which lie at 87 km and 95 km respectively, the density decreases by a factor of $\simeq 6$ [*Chamberlain*, 1978] and thus the amplitude of a nondispersive wave should increase by a factor of $\simeq 2.5$ (or by a factor of 3 according to *Noxon* [1978]). If an amplitude increase is not observed in the data, then this is evidence for some sort of wave dissipation.

It can be seen, in the group and phase velocity equations, that the upper frequency limit, N, and the lower frequency limit, f, act to inhibit or select different wave frequencies. The quantities, N and f are not constants, but change with changing conditions and latitudes. Likewise, the wave itself can travel into regions of different mean wind and thus, the apparent frequency of the waves can change. As this Doppler-shifted frequency, β, approaches the lower limit, f, the vertical energy propagation goes to zero. This is defined as a *critical level* in the atmosphere. Conversely, as the wave frequency approaches the Brunt-Väsällä frequency, N, the vertical energy propagation goes to zero, but in this case the vertical wavelength goes to infinity and the wave is reflected. This is called a *turning level*. Given the correct conditions, it is possible for a wave to be ducted between two turning level altitudes. In this case, the wave may travel horizontally over

long distances. If a wave undergoes dissipation, the wave energy can be transformed into thermal energy through viscous or heat conductive processes or it can dissipate into turbulence.

4.2 Wave Effects

One of the ways in which gravity waves have been studied is via the airglow emissions. The propagation of gravity waves through the atmosphere will modify the temperature of the region and often produce eddies and mixing. This can change the density of the minor constituents and, as a result, change the intensity of the airglow emissions as well as the observed temperature. The intensity of OH, for instance, is dependent upon several minor atmospheric constituents which may or may not vary in the same way as the local density of the atmosphere. It is important to understand how the density and temperature of the atmosphere will change as the gravity wave passes.

Interest in the interaction between gravity waves and the atmosphere has grown since the first theoretical description of gravity waves by *Hines* [1960]. In the last couple of decades it has been recognized that gravity waves are a major contributor to the dynamics of the middle and upper atmosphere. The dissipation of gravity waves can play an important role in the energy balance of the atmosphere, as well as provide a driving force for the mean wind. Theoretical studies such as those done by *Hines* [1972], *Houghton* [1978], and *Lindzen* [1981], and the review by *Fritts* [1984], suggest that gravity waves may be a primary factor in the energy and momentum budget of the mesosphere.

Since gravity waves usually propagate upward, the source of lower and middle atmospheric gravity waves is often tropospheric disturbances such as storms and mountains. Some of the tropospheric gravity waves travel up as high as the mesopause region. There are also mechanisms for the local production of gravity waves in the upper atmosphere.

The polar jet often moves meridionally with great velocities. Theoretically, this horizontal motion is enough to stimulate gravity waves. Also, local wind shear can produce gravity waves as well. A source of thermospheric and ionospheric gravity waves is known to be auroral activity. It is theorized that the rapid Joule heating of the ionosphere by the aurora can cause propagating ionospheric gravity waves [*Richmond and Matsushita*, 1975, and *Hunsucker*, 1975].

Since dissipation occurs for almost any wave, upward propagating gravity waves will not grow exponentially as predicted by non-dissipative theory. The amplitude of a gravity wave may grow as the wave propagates upward but as the dissipative processes become larger, the amplitude of the wave may reach a maximum and then, actually decrease. There are at least two types of instabilities that might arise. The most important is due to the advection of more dense air over less dense air in two adjacent phases of a wave [*Fritts*, 1984]. The second is a dynamical instability due to large velocity shears and small static stability within the wave field. Both of these will result in the dissipation of wave energy through either turbulence and turbulent heating or an acceleration of the mean flow. In both mechanisms the result is that the energy, which is added to the tropopause by orographic or meteorologic disturbances, will be transported over large vertical and often horizontal distances. It is this energy transport that makes gravity waves an important element in the atmospheric energy balance [*Fritts*, 1984].

Gravity waves can also interact with other waves to produce third waves [*Hines*, 1960]. *Fritts and Vincent* [1987] have experimental and theoretical evidence of gravity waves interacting with tidal oscillations. *Sivjee et al.* [1987] observed semidiurnal oscillations in the high latitude winter mesopause where linear tidal theory does not predict tides at all and they concluded that these oscillations must also be the result of interactions between gravity waves and tidal oscillations.

4.3 Theoretical Calculations of η and Phase for the OH Emission

Krassovsky [1972] was one of the first to use simple chemistry to interpret the observed fluctuations in his airglow observations. In an attempt to explain his observations, *Krassovsky* introduced a parameter, η, defined as the ratio of the relative amplitudes of the fluctuations in intensity, I, and temperature, T, of an airglow emission. More specifically, η is defined as

$$\eta = \frac{\delta I/\bar{I}}{\delta T/\bar{T}}$$

where the δ indicates fluctuation amplitude, and the overbar indicates time averaged quantities.

There have been numerous studies that discuss the theoretical limits of η. *Krassovsky* [1972] calculated that η should have the form

$$\eta = \frac{2}{\gamma - 1} - \mu$$

where $\gamma = 1.4$ is the ratio of specific heats and μ is the temperature dependence $(T^{-\mu})$ of the three body reaction for O_3 production. Thus for $\mu = 4$ he calculated that η should be on the order of 1. Using similar calculations, but adding temperature dependence of the O_3 loss mechanism, *Hamwey* [1985] predicted higher values for η (i.e. $\eta = 4$). It is clear, from the examples given at the end of the previous section, that η is not single valued.

Walterscheid et al. [1987] added OH chemistry to linear gravity wave dynamics and concluded that the parameter η is a complex quantity depending on wave period, emission layer height, as well as atomic oxygen scale height. The *Walterscheid et al.* study also used a temperature dependence of $\exp[510/T]$ for the O_3 production mechanism. The following is a review of the *Walterscheid et al.* study.

The number density, n, of any minor species can be determined by applying the continuity equation,

$$\frac{\partial n'}{\partial t} = \mathcal{P}' - \mathcal{L}' - \nabla \cdot \left[n\mathbf{U} + \mathbf{K} \cdot N\nabla\left(\frac{n}{N}\right) \right] \qquad 4.6$$

The terms $\mathcal{P}$ and $\mathcal{L}$ are the rates of volumetric production and loss of the minor constituents by chemical reactions. The primes indicate perturbed quantities. The quantity $\mathbf{K} \cdot N\nabla\left(\frac{n}{N}\right)$ is the eddy diffusion contribution to the number density and $\mathbf{K}$ is the eddy diffusion tensor. N is the total number density and it is assumed that all of the species, both major and minor, have the same temperature, T, and velocity, u.

The production and loss terms are, in general, proportional to the product of a temperature dependent reaction rate, $k(T)$, and the concentrations of the reacting species. The chemistry that *Walterscheid et al.* used included the following five reactions;

$$H+O_3 \rightarrow OH+O_2 \qquad k_9 = 1.4 \times 10^{-10} e^{(-470/T)} cm^3/s$$

$$O+HO_2 \rightarrow OH+O_2 \qquad k_{11} = 4 \times 10^{-11} cm^3/s$$

$$O+OH \rightarrow O_2+H \qquad k_7 = 4 \times 10^{-11} cm^3/s$$

$$O+O_2+M \rightarrow O_3+M \qquad k_2 = 1 \times 10^{-34} e^{(510/T)} cm^6/s$$

$$H+O_2+M \rightarrow HO_2+M \qquad k_{10} = 2.1 \times 10^{-32} e^{(290/T)} cm^6/s$$
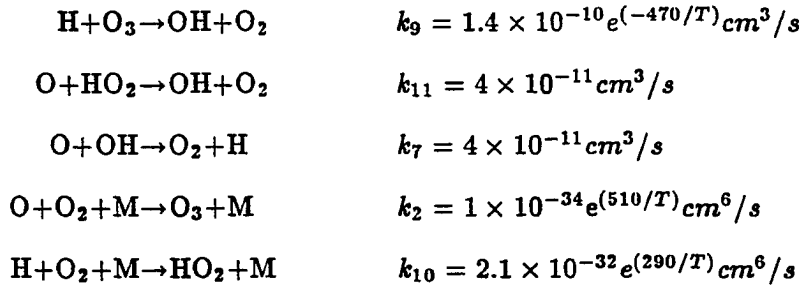
where M is any third atom or molecule (usually N_2 or O_2). The values on the right are the reaction rate constants used by *Walterscheid et al.*

The continuity equation (Equation 4.6) can be linearized about a steady state, $\overline{\mathbf{U}} = 0$, $\overline{T}$ =constant, and $\overline{n} = \overline{n}(z)$, to yield

$$\frac{\partial n'}{\partial t} = \mathcal{P}' - \mathcal{L}' - \frac{d\overline{n}}{dz}w' - \overline{n}\nabla \cdot \mathbf{U}'.$$

The next assumption is that the waves are plane waves propagating in the $x - z$ plane

and thus,

$$(n', T', u', \cdots) = (\hat{n}(z), \hat{T}(z), \hat{u}(z), \cdots) \exp(i\omega t - ik_x x)$$

where ω is the circular frequency of the wave, k_x is the horizontal wave number, and the *hat* denotes the $z-$dependant part of the fluctuation. The resulting, linearized equation is

$$i\omega \hat{n}' = \mathcal{P}' - \mathcal{L}' - \frac{d\overline{n}}{dz}\hat{w}' - \overline{n}\left(-ik_x \hat{u}' + \frac{\partial \hat{w}'}{\partial z}\right)$$

Gravity wave dynamics are used to relate u', w' and $n'(M)$ to the perturbed temperature T' for each of the constituents, M. According to *Walterscheid et al.* [1987], the relevant formulae are

$$-ik_x \hat{u}' + \frac{\partial \hat{w}'}{\partial z} \equiv f_1 \frac{\hat{T}'}{\overline{T}}$$

$$\hat{w}' \equiv f_2 \frac{\hat{T}'}{\overline{T}}$$

$$\frac{\hat{n}'(M)}{\overline{n}(M)} \equiv f_3 \frac{\hat{T}'}{\overline{T}}$$

where the functions f_1, f_2, and f_3 depend only on wave frequency, horizontal wave number, direction of wave energy propagation, and the scale heights of the major gas. These functions can be found in *Walterscheid et al.* [1987]. The production and loss terms are calculated for the five constituents as a set of five equations with five unknowns.

To calculate the parameter η, it was assumed that the OH nightglow intensity was directly proportional to the production rate of excited OH. The resulting formula for η, which depended on wave period, horizontal wave number, and the O scale height, is

$$\eta = \frac{\hat{I}'/\overline{I}}{\hat{T}'/\overline{T}}$$

$$= \{\overline{k}_9 \overline{n}(H)\hat{n}'(O_3) + \overline{k}_9 \overline{n}(O_3)\hat{n}'(H) + \overline{k}_9 \left(\frac{470}{\overline{T}}\right) \frac{\hat{T}'}{\overline{T}} \overline{n}(H)\overline{n}(O_3)$$

$$+ \overline{k}_{11}\overline{n}(O)\hat{n}'(HO_2) + \overline{k}_{11}\overline{n}(HO_2)\hat{n}'(O)\}$$

$$\cdot \{\overline{k}_9 \overline{n}(H)\overline{n}(O_3) + \overline{k}_{11}\overline{n}(O)\overline{n}(HO_2)\frac{\hat{T}}{\overline{T}}\}^{-1}$$

Since all of the $\hat{n}'$ terms are complex quantities, it is clear that η is also a complex

quantity. For the rest of this thesis, let η refer to $|\eta|$.

Walterscheid et al. also added a significant calculation modification to their model. Most of the atmospheric models are calculated in the *Lagrangian* frame of reference, which is the reference frame of the air parcel. Ground based observations do not follow air parcels, but instead, they monitor a specific volume of space and observe the air parcels that pass through. This is an *Eulerian* frame of reference. *Walterscheid et al.* did their calculations in the Eulerian reference frame to improve the comparison between model and data.

The results of the *Walterscheid et al.* study are shown in Figure 4.1 where both η and phase relationships between temperature and intensity are plotted as a function of frequency. In both of the plots of Figure 4.1, the dashed curve is the value of each parameter when only the dynamics is considered and the dotted curve is the value with only chemistry. The solid curve is the combination of chemistry and dynamics. It is clear that neither chemistry nor dynamics can be ignored when examining the effects of gravity waves on the OH airglow.

In order to simplify their calculations, *Walterscheid et al.* omitted the eddy diffusion term with the justification that diffusion time scales are much longer than gravity wave time scales at the height of 85 km. *Hickey* [1987a] found that, for short period waves, this is indeed true, but for waves with periods longer than approximately 2 hours, *Hickey* found significant deviations from the *Walterscheid et al.* calculations.

Hickey [1987a] began with the *Walterscheid et al.* [1987] model and added the dissipative effects of eddy viscosity, thermal conduction, and Coriolis forces. *Hickey's* notation is substantially different from that of the *Walterscheid et al.* study and so the resulting equations are not even similar at first glance. It is, however, sufficient to summarize qualitatively *Hickey's* results.
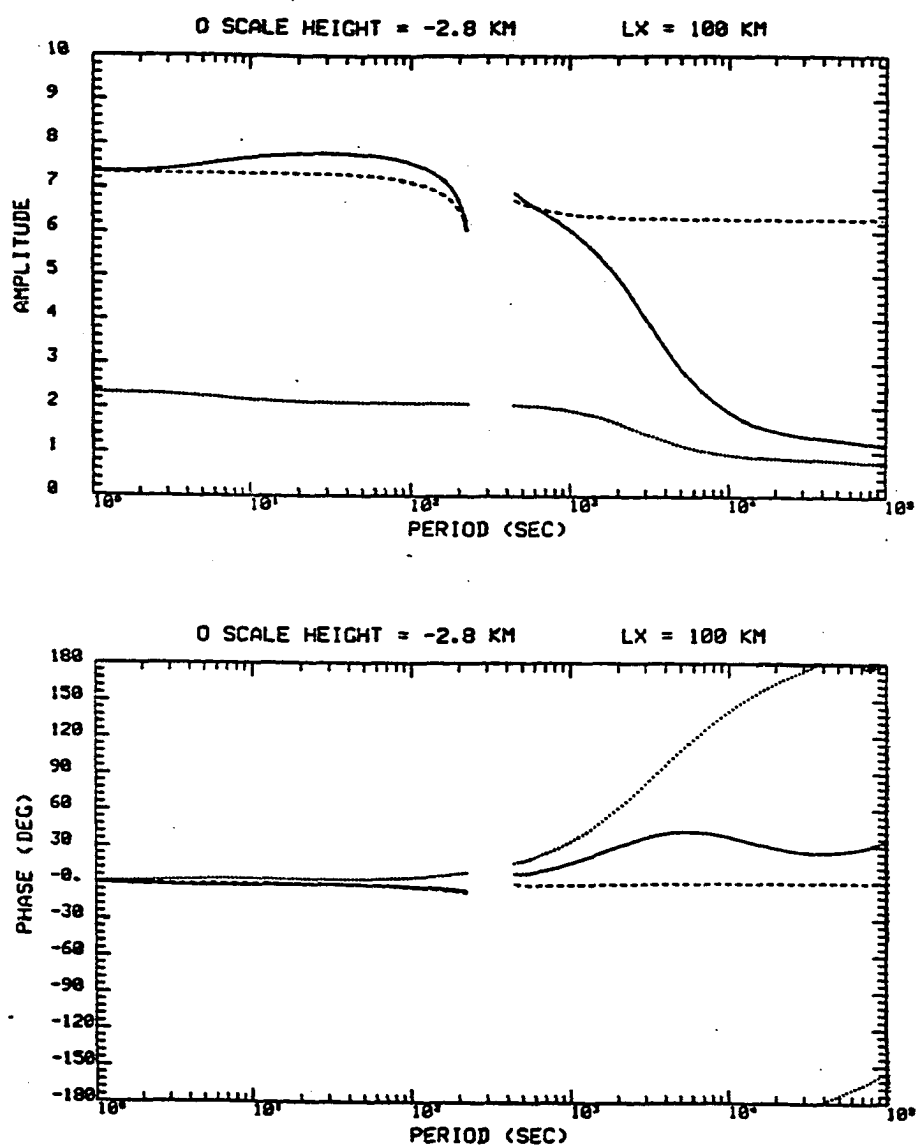
Fig. 4.1 Theoretical values of η and phase as calculated by *Walterscheid et al.* The dotted lines are the values if only chemistry is considered and the dashed is only dynamics. The solid line is the combined value and represents the theoretical values of η and phase.

The most significant result of *Hickey's* study is the modification of the parameters η and phase relative to those of *Walterscheid et al.* The addition of the eddy diffusion and eddy thermal conduction increases the value of η by as much as an order of magnitude at periods greater than 2 to 3 hours. The modification in the phase angle is also most pronounced at longer periods with a significant decrease in the phase angle for the longer periods.

In a second study, *Hickey* [1987b] concluded that η is also dependent on the horizontal wavelength, λ_x. This is due to the reduction in wave amplitude, for long period waves, by the dissipation processes. *Hickey's* modification of the *Walterscheid et al.* model can be seen in Figure 4.2 where η and the phase are calculated for the gravity wave periods of airglow oscillations. The largest difference between the two models is in the long period limits.

The results of the two theories can be presented together as is done in Figure 4.2. The *Walterscheid et al.* study (solid lines in Figure 4.2), concludes that not only is η a complex parameter, but also that both η and phase are frequency dependent. The *Hickey* modification to the *Walterscheid et al.* study concludes that the parameters of η and phase are modified significantly for long periods by nonlinear dissipative effects. *Hickey,* [1987b] also finds that there is a significant dependence, of η and phase, on the horizontal wavelength of the gravity wave. Figure 4.2 shows the important aspects of the results of the two studies by *Hickey* [1987 a and b]. The different traces on the plots refer to different horizontal wavelengths.

4.4 Theoretical Calculations of η and Phase for the O_2 Emission

The interaction of gravity waves with the O_2 airglow was examined theoretically by *Weinstock* [1978] using nondissipative gravity wave theory. He calculated that this
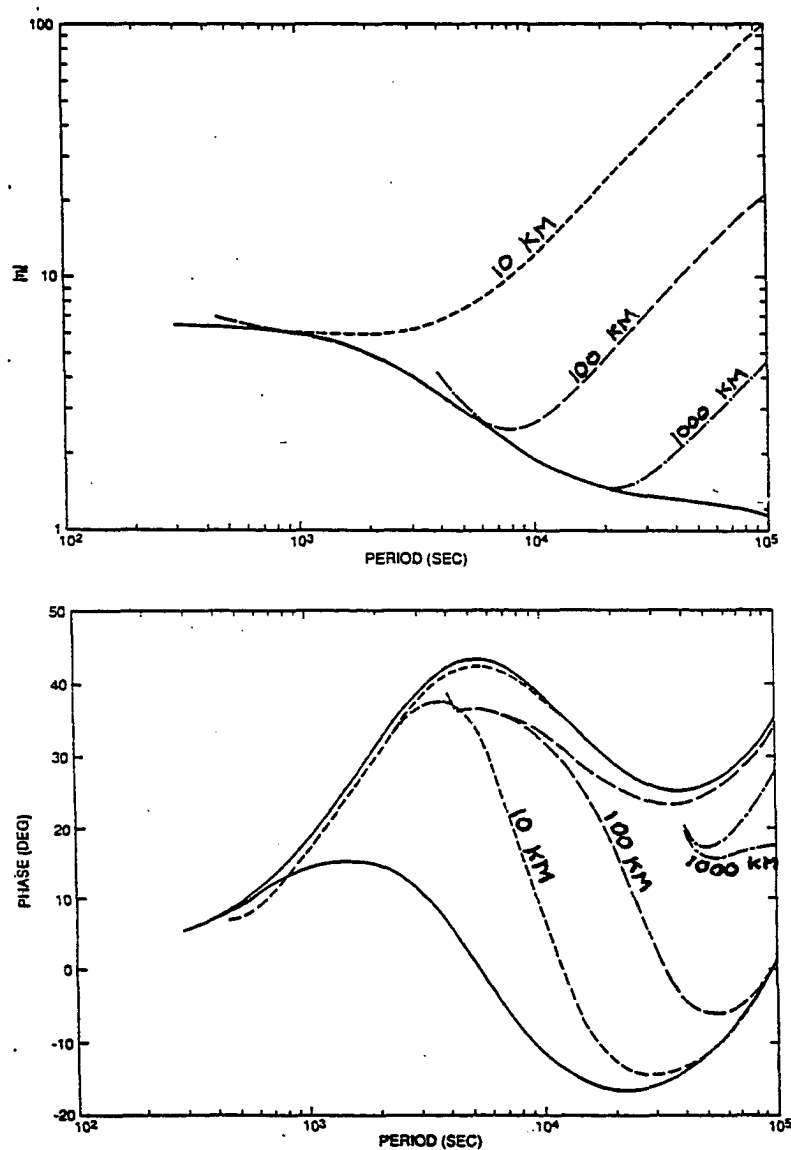
Fig. 4.2 Modifications to the parameters η and phase angle as recalculated by *Hickey* [1987a,b] including nonlinear dissipation terms and the dependence on horizontal wavelength. The top plot shows the theoretical values of the ratio of the relative amplitudes, or η. The bottom plot is the same for the phase angle, θ. The solid line in both traces is the results of the *Walterscheid et al.* [1987] model, the dotted lines are the *Hickey* [1987b] modification to the *Walterscheid et al.* model for 10 km, 100 km, and 1000 km wavelengths.

theoretical treatment, which includes some of the chemistry, yields

$$\eta = \frac{2}{\gamma - 1} - \mu - \left\{ 1 + \frac{\gamma}{\gamma - 1} \left(\frac{H}{H^*} + 1 \right) \right\}$$

where H is the major species scale height (O_2 in this case) and H^* is the minor species scale height (hydrogen or atomic oxygen depending on the mechanism).

Weinstock found η values between -0.1 and +1.1 depending on the scale height of atomic oxygen. The resulting phase angle between temperature and intensity, as calculated by *Weinstock* was either $0°$ or $180°$. He did not attempt to include frequency dependence or gravity wave dissipation in his model. The conclusion of *Weinstock's* study was that, for the O_2 emission, the fluctuations in intensity were too sensitive to atomic oxygen profiles and thus, were not good indicators of gravity wave propagation. One would have to conclude from *Weinstock's* results that η is not a good quantity to use in the analysis of gravity waves observed in the O_2 airglow emissions.

An important point, which was first mentioned by *Weinstock* and later discussed in detail by *Hines and Tarasick* [1987] and *Schubert and Walterscheid* [1987], is the effect of a thick emitting layer. If the vertical wavelength of the gravity wave is equal to or less than the thickness of the emitting layer, then the oscillations of the wave will be reduced or even lost, by the effect of averaging over part or all of a wave cycle. The conclusion by *Weinstock*, at least for O_2 emissions, is that the temperature is not as sensitive to the thickness of the layer as is the intensity. *Hines and Tarasick* claim that their calculations allow for any ratio of brightness to temperature fluctuations as long as the waves are evanescent. Unfortunately, *Schubert and Walterscheid* do not attempt to calculate the integrated intensity, but they do conclude that the intensity measurements will be strongly biased toward long vertical wavelength waves.

CHAPTER 5

A Comparison of Observations and Theories

In the previous chapter, it was determined that fluctuations in the rotational temperature and in the intensity of the OH and O_2 airglow could theoretically be the result of the passage of internal gravity waves through the region. There have been numerous observations of oscillations, or waves, in the brightness and temperature of the airglow. As mentioned before, *Noxon* [1978] observed what appeared to be the effects of gravity waves in the OH and O_2 airglow but, since *Weinstock* [1978] concluded that airglow brightness was not a good gravity wave indicator, *Noxon* only calculated the rotational temperatures. *Krassovsky* [1972] attempted to fit all of his data to one value of the parameter, η. The theories by *Walterscheid et al.* [1987] and *Hickey* [1987a,b] imply that η may change with wave period. Observations by *Sivjee et al.* [1987] and *Hecht et al.* [1987] were not in good agreement with the theories, but both studies based their results on only a few examples. Likewise, *Myrabø et al.* [1987] did not have a large enough data base, nor were the parameters η and phase calculated. In this chapter, the predicted response of the airglow to gravity waves is compared with the observed oscillations for a more extensive data set.

5.1 Data Analysis Technique: The Calculation of η and Phase From the Data

To calculate η and the phase angle between the temperature and intensity fluctuations, it was assumed that the data have been reduced to two time series; one of emission intensity, $I(t)$, and one of temperature, $T(t)$. The uncertainties in both temperature and intensity are less than 3% of the average value. It is often useful to eliminate some of

the random noise by smoothing the time series with a three-point triangle filter before doing the analysis. This is done only when analyzing the data for long period gravity waves, since a three point running average is essentially a low pass filter.

In order to simplify the comparison between the model and the data, it was necessary to transform the time series into the frequency domain via the Fourier transform. This was done by convolving the data sets with a cosine taper, in order to eliminate spurious power from unbalanced endpoints, and then applying a *Mixed Radix* Digital Fourier transform (which is not restricted to data sets with 2^n data points). If we define $\mathcal{X}(\omega)$ to be the discrete Fourier transform of the time series, $X(t)$, (where ω implies the frequency domain), then $\mathcal{X}(\omega)$ is defined as

$$\mathcal{X}(\omega) = \sum_{t=1}^{n} X(t)\exp\left[-\frac{i2\pi t\omega}{n}\right].$$

Using the above formula to obtain $\mathcal{I}(\omega)$ and $\mathcal{T}(\omega)$, it is then possible, following *Jenkins and Watts* [1968] (equations 9.3.1 through 9.3.12), to define the *spectral estimates* for intensity and temperature as,

$$G_I(\omega) = c_g|\hat{\mathcal{I}}(\omega)|^2$$

$$G_T(\omega) = c_g|\hat{\mathcal{T}}(\omega)|^2,$$

and the *cross spectral estimate* between temperature and intensity as

$$G_{IT}(\omega) = c_g\hat{\mathcal{I}}(\omega)^*\hat{\mathcal{T}}(\omega) \qquad\qquad 5.1$$

where the star represents the complex conjugate, $c_g = (1/nf_s t)$ is the gain, and f_s is the sampling frequency. It should be noted that before calculating the spectral estimates, it is necessary to smooth $\mathcal{I}(\omega)$ and $\mathcal{T}(\omega)$ by using a simple three point triangle filter, as indicated by the *hats*. The *cross spectral estimate* of unsmoothed, transformed data is identically one [*Bloomfield*, 1976].

The *cross spectral estimation* (Equation 5.1) can then be used to quantify the correlation between intensity and temperature fluctuations by calculating the *magnitude squared coherency* spectrum

$$C_{IT}^2(\omega) = \frac{|G_{IT}|^2}{G_I G_T}.$$

The range of C_{IT} is between 0 and 1 where $C_{IT} < 1$ implies that there are uncorrelated signals in the data. It is possible to estimate the 95% upper and lower confidence limits for the data by assuming a *Chi squared distribution* [*Jenkins and Watts*, 1968]. Figure 5.1 shows the magnitude squared coherency with the 95% confidence limits. The horizontal dotted line indicates the level above which C_{IT} is found to be statistically different from zero.

Following the methods of *Sivjee et al.* [1987] and *Hecht et al.* [1987], the value of the parameter η can be calculated with the formula

$$|\eta(\omega)| = \frac{G_{IT}}{G_T}\frac{\overline{T}}{\overline{I}}$$

where (G_{IT}/G_T) is the gain estimate. The phase angle, between fluctuations in $I(t)$ and $T(t)$, is calculated as a function frequency by the formula

$$\theta(\omega) = \arctan\left[\frac{-Im(G_{IT})}{Re(G_{IT})}\right]$$

It was determined, using a random sample test, that neither the phase angle, $\theta(\omega)$, nor $\eta(\omega)$ are significant if the *magnitude squared coherency*, $C_{IT}^2(\omega)$ is less than approximately 0.5. Figure 5.2 shows a plot of θ and η as a function of frequency for the same data as in Figures 3.1-3.3. The horizontal bars represent the only periods for which the values of η and phase are significantly different from zero. Thus, to compare observations with theory, it is imperative to compare only the significant values of η and phase angle with the predicted values.

362/15:23
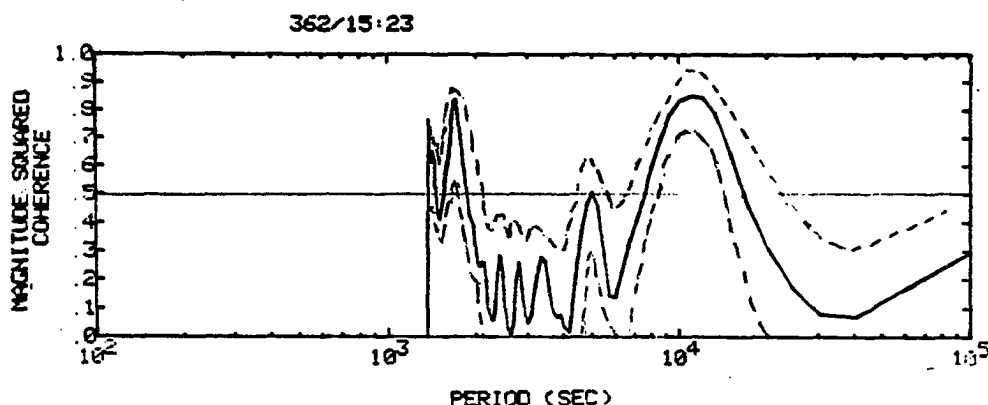
Fig. 5.1 Magnitude squared coherency between the OH airglow intensity and temperature, as a function of frequency calculated from the data in figure 3.3. The upper and lower curves are the 95% confidence limits. The horizontal line is the level above which C_{IT} is statistically different from zero. This information is used to determine if, and at what frequency, the OH airglow showed signs of the passage of gravity waves.

For a given data set, the values of η and phase angle are plotted only when the *magnitude squared coherency*, $C_{IT}^2(\omega)$, was greater than 0.5. This technique produced plots shown in Figure 5.3. In order to cover the complete range of frequencies, without aliasing or mixing wave packets, several passes over the same data set were necessary. Each pass was done with different numbers of data points. In this way, wave packets of different sizes and periods would be represented in the plots of η and phase.

At the short periods ($< 2 \times 10^3$ sec.) there is a significant amount of scatter in the plots of η and phase. This could be a consequence of Doppler shifting of the wave frequency by a mean wind. There is also a large discrepancy between the data and the
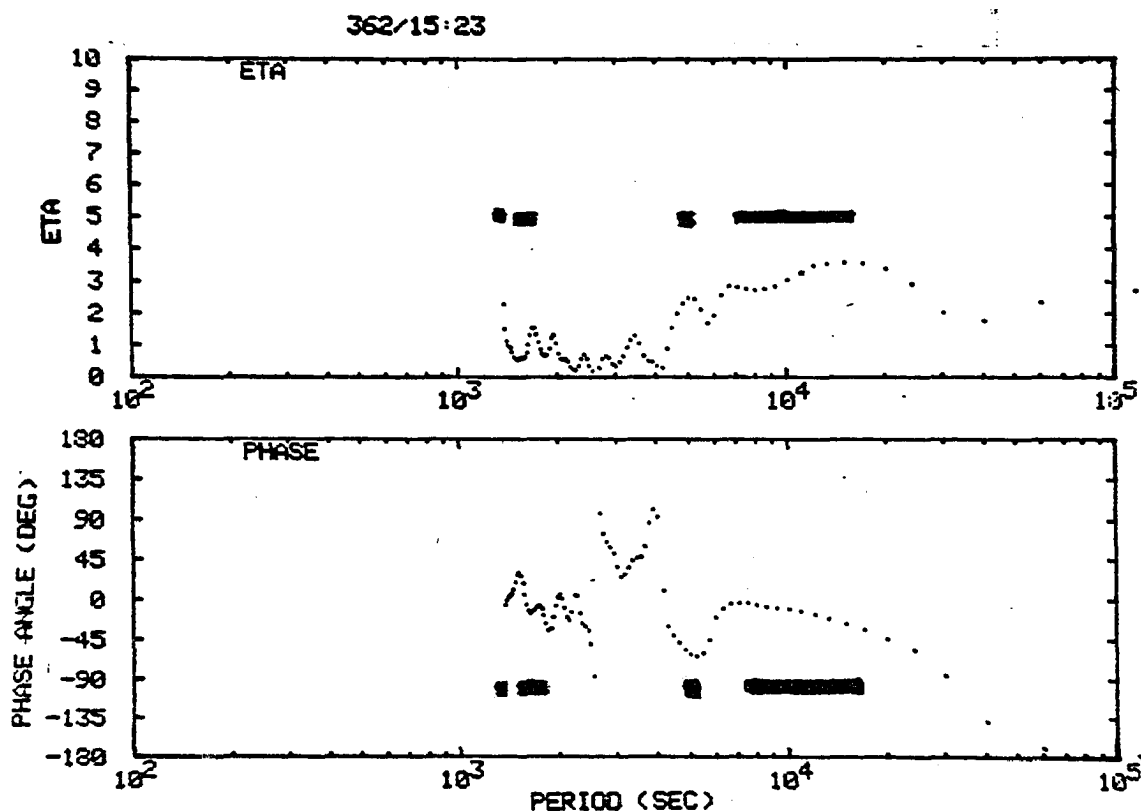
Fig. 5.2 Observed values of η (top) and phase angle, θ (bottom), plotted as functions of frequency calculated for the data shown in Figure 3.3. The horizontal bars represent the wave periods for which the magnitude squared coherence, as shown in Figure 5.1, was greater than 0.5, or in other words, the bars indicate where the data is statistically valid.

models by *Walterscheid et al.* [1987] and *Hickey* [1987a,b]. Again, the Doppler shifting of the wave period by the mean wind may be a problem but it is not possible to increase the values of η for the short wave periods. Thus the Doppler effect would not produce the discrepancy.

Another possible explanation for the discrepancy is that the short period gravity waves have spatial scales which are less than the size of the region of integration defined by the thickness of the emission layer and the field of view of the instrument. The
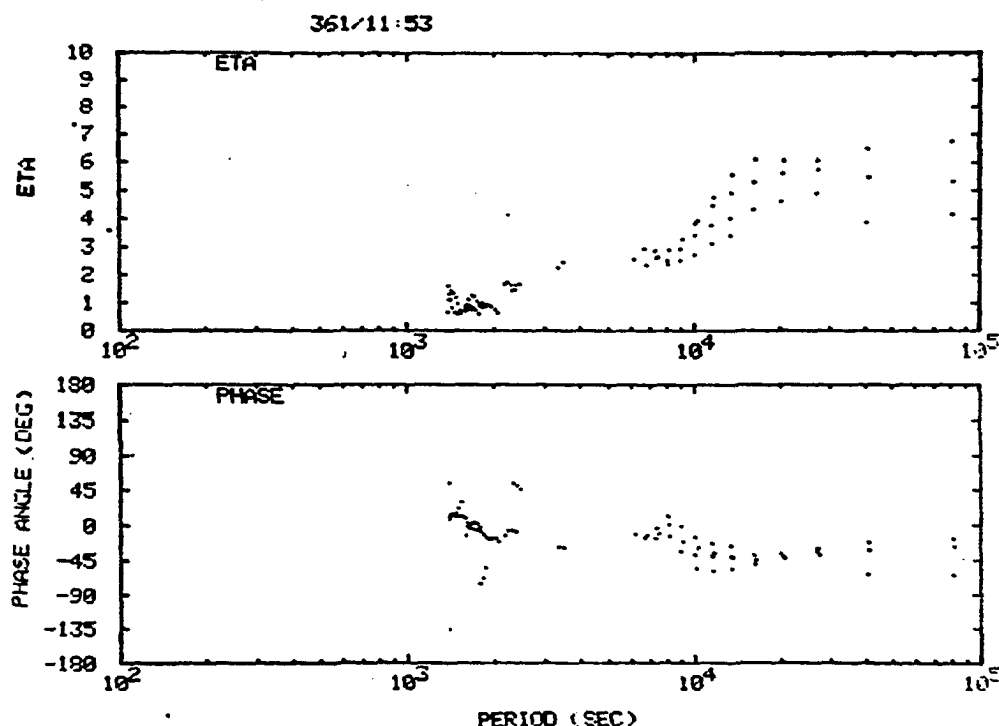
Fig. 5.3 Scatter plots of the values η (top), and *phase* (bottom) plotted as a function of wave period. Note that η and phase are plotted only when the coherence is larger than 0.5. Smaller values of coherence were not statistically valid. This figure covers 5 days of data.

emission layer is observed to be on the order of 2-4 km thick with a sharp peak [*Baker*, 1978]. Using a sodium lidar to observe vertical waves in an emission layer 20 km thick, *Gardner and Voelz* [1986] observed that gravity waves with vertical wavelengths of 3 km and less have periods of 40 minutes and less (see Figure 5.4). Thus, it would be difficult to observe fluctuations in the OH airglow, with periods much less than 40 minutes. The OH layer itself, has a very sharp emission peak, and thus, some fluctuations will be observed, even for shorter periods. But the values of η and phase may not be as accurate for the shorter period gravity waves. The problem with this explanation for the discrepancy
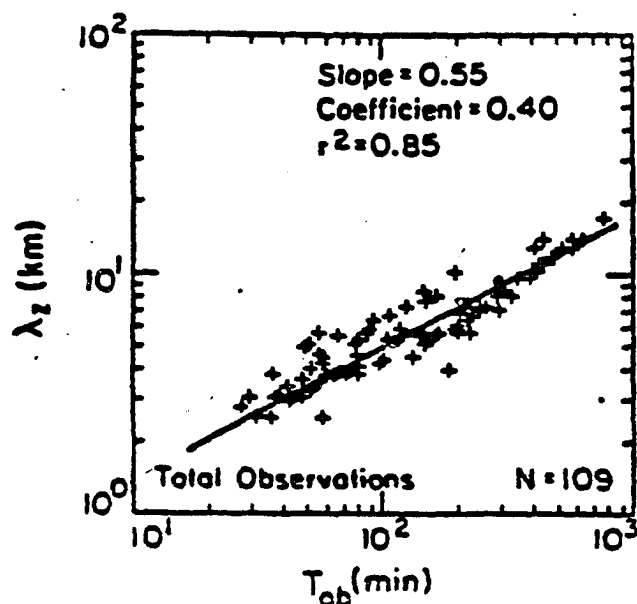
Fig. 5.4   Vertical wavelength of gravity waves as a function of observed period as observed by *Gardner and Voelz* [1986]. These measurements were made with a sodium lidar, from Urbana, Illinois. The data represent the observed effect of gravity waves on the sodium density and shows that gravity waves with periods less than 40 minutes have vertical wavelengths less than 3 km.

is that gravity wave theory predicts short vertical wavelengths to correspond with long period waves. However, this is contradictory to the observations by *Gardner and Voelz* [1986].

Weinstock [1978] did predict similar results for the O_2 emission. He concluded that the brightness fluctuations would be much more susceptible to smoothing by a thick emission layer than would be the temperature fluctuations. This conclusion was disputed by *Hines and Tarasick* [1987].

Another possible explanation for the large scatter and discrepancy at short periods is that the horizontal wavelength is less than the field-of-view of the spectrometer. Many

of the wave-like structures, seen by *Taylor* [1987] have horizontal wavelengths on the order of 15 km. The spectrometer used in this study had a 7.5° half angle field-of-view, which corresponds to a region of the sky 18 km on a side, which is too large to detect features with scale sizes less than 18 km. Moreover, it would be difficult to observe waves with horizontal wavelengths less than twice the field-of-view, or 36 km. Unless the horizontal wavelength is known to be larger than 36 km, the results are suspect.

There is some variation of η and phase at the longer periods as well. Doppler shifting of the wave can produce substantial variability between observed and intrinsic wave periods. If the background wind is strong, for example, the observed wave period will be Doppler shifted. If a wave is propagating in the same direction as the mean wind, the observed wave will be Doppler shifted to a higher frequency. Likewise if the wave and the wind are in opposite directions the observed wave frequency can be Doppler shifted to lower frequencies.

5.2 Comparing Observations with Theory for the OH Airglow

The calculated parameters of the *Walterscheid et al.* [1987] study are shown on the same plot with those from my data in Figure 5.5. There are obviously few similarities between the data and the model. For short period waves, the model predicts the largest values of η. The smallest η values should be found for the longest period waves. The reverse is true according to my data.

The *Walterscheid et al.* study does predict variations based on changes in the scale height of atomic oxygen, but the changes are not large enough to account for the discrepancy between data and theory, even if the scale height of O changes by more than the 50% variation used by the *Walterscheid et al.* study.
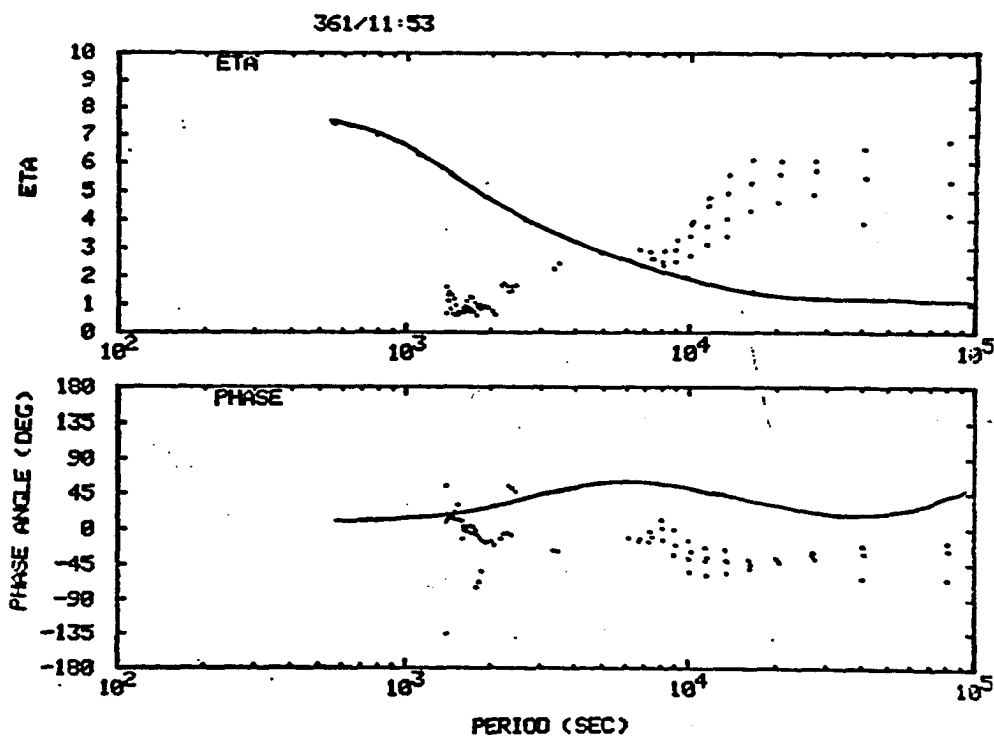
Fig. 5.5 The parameters η and phase, calculated from the data. The points represent values where the magnitude squared coherence was greater than 0.5 . The solid line represents the value predicted by *Walterscheid et al.* [1987].

In another study, *Hickey* [1987a] modified the *Walterscheid et al.* model to include the effects of eddy diffusion, thermal conduction and the Coriolis force on the effects of gravity waves on the OH airglow. The changes were very significant as can be seen in Figure 5.6. where the results of the *Hickey* study are plotted along with the original results of *Walterscheid et al.* In a second study, *Hickey* [1987b] found that η is very sensitive to the horizontal wavelength of the gravity wave as can also be seen in Figure 5.6. If *Hickey's* calculations are correct, then the variability in phase and η that is observed in the data can be easily due to changes in horizontal wavelength. It may be
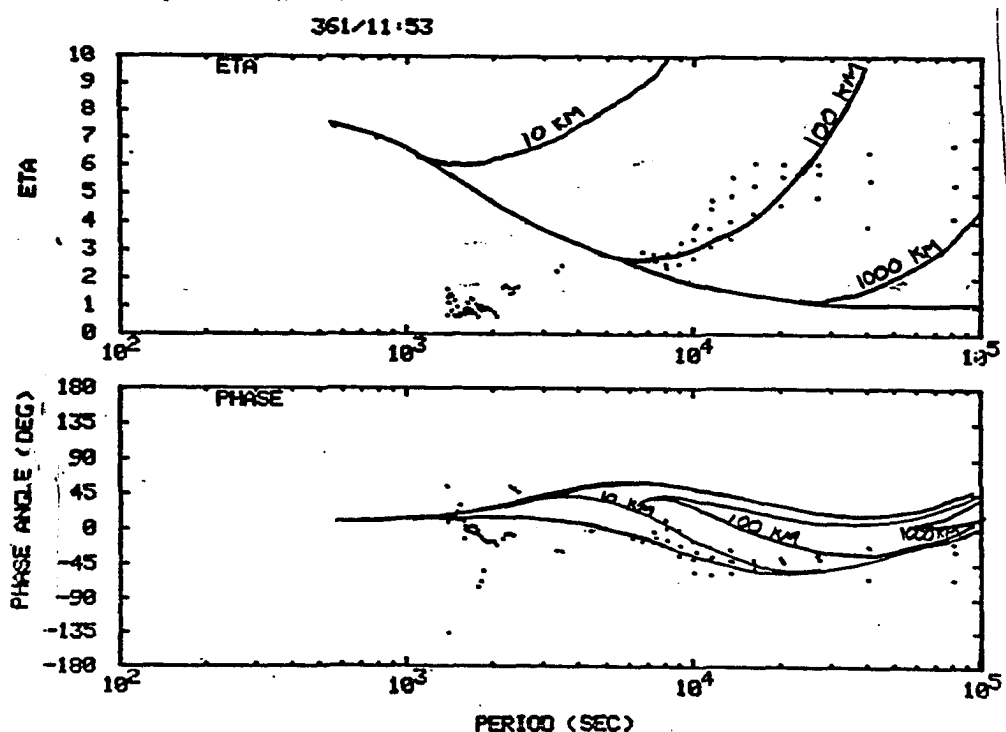
Fig. 5.6 Data from our study plotted along with the theoretical predictions by *Hickey* [1987a,b]. There is a large disagreement between the theory and the data at the small period end of the plot. The *Hickey* [1987a,b] models are a vast improvement over the linear model of *Walterscheid et al.* [1987].

possible to determine the horizontal wavelength of a gravity wave with measurements from a single location by application of *Hickey's* model.

The short-period end of the observed spectrum does not agree well with either model. There have been some very recent studies of the effect that a short vertical wavelength in a thick airglow layer might have on the calculation of η and phase. *Hines and Tarasick* [1987] and *Schubert and Walterscheid* [1987] have both published reports on this subject and both agree that there will be a significant effect. *Schubert and Walterscheid* did not attempt to determine how the observed, height integrated, measurements of temperature

might be affected and thus, they do not help in modifying the η and phase values. *Hines and Tarasick* concluded that any value for the parameter, η, is possible if the waves are evanescent. Thus, their study may help to explain the scatter but not the low values.

In summary, it is clear from my data that the parameters η and phase are dependent on wave period, as predicted by *Walterscheid et al.* [1987]; however, their theory does not predict the dependence that was observed. This discrepancy is partially eliminated by the modifications to the *Walterscheid et al.* model by *Hickey* [1987a,b]. *Hickey* included the nonlinear effects of thermal conduction and eddy diffusion and found significant changes in η and phase at long periods as compared to the original model. His theory is also in better agreement with my data. The variation in the data could also be accounted for by the fact that we have not eliminated the Doppler shifting in period due to the background wind. This is a major effect for waves with phase speeds which are of the same order of magnitude as the wind speed, but is not addressable in this study. The deviations from theory at short periods may have resulted from the observations having been integrated over a volume which was larger than the wavelength of the waves.

It is clear from the comparison between observations of η and phase angle and the *Walterscheid et al.* model as modified by *Hickey*, that the fluctuations observed in the OH airglow are most probably the interaction of internal gravity waves with the atmospheric airglow. There are no other atmospheric oscillations with such broad temporal and spatial scales.

5.3 Effects of Gravity Waves on The $O_2(\Sigma^1)$ Airglow Emissions: Theory and Observations

Since the $O_2(0\text{-}1)$ atmospheric band is much weaker in intensity and the spectral lines are much closer together, the analysis of the O_2 data is much more difficult. It is probably

for this reason that there have been relatively few studies done on the interaction of O_2 with internal gravity waves. The previous experimental research includes studies on the high latitude intensity of O_2 by *Myrabø et al.* [1984], comparisons of O_2 emissions with OI emissions by *Witt et al.* [1979], and rocket measurements of the altitude of the O_2 emission [*Donahue et al.* 1973].

Noxon [1979] measured O_2 temperatures, but not intensity, on the suggestion of *Weinstock* [1978], who said that the fluctuations in emission brightness were too dependent on emission layer thickness. Since recent developments in gravity wave airglow theory have raised some questions about *Weinstock's* work [see *Hines and Tarasick*; 1987], we decided to re-examine the relationship between O_2 airglow intensity and temperature.

Figure 5.7 is an example of η and phase for the O_2 emissions. The values for η are similar to those calculated for OH, and range between $\eta < 1$ and $\eta \approx 8$. The plot of the phase angle between intensity and temperature, shows that the temperature and intensity are $180°$ out of phase for most of the frequencies.

Following the calculations in the atmospheric dynamics text by *Holton* [1979], it is possible to explain the phase angle observations using linear gravity wave theory. We can begin with the hydrostatic relation

$$\frac{\partial \overline{p}}{\partial z} = -\overline{\rho}g$$

where p is pressure, z is height, ρ is density, and g is the gravitational constant. The *potential temperature* is defined as

$$\theta = T(\frac{p_o}{p})^\gamma$$
$$= \frac{p}{\rho R}(\frac{p_o}{p})^\gamma$$

where R is the ideal gas constant, and γ is the ratio of specific heats. From these
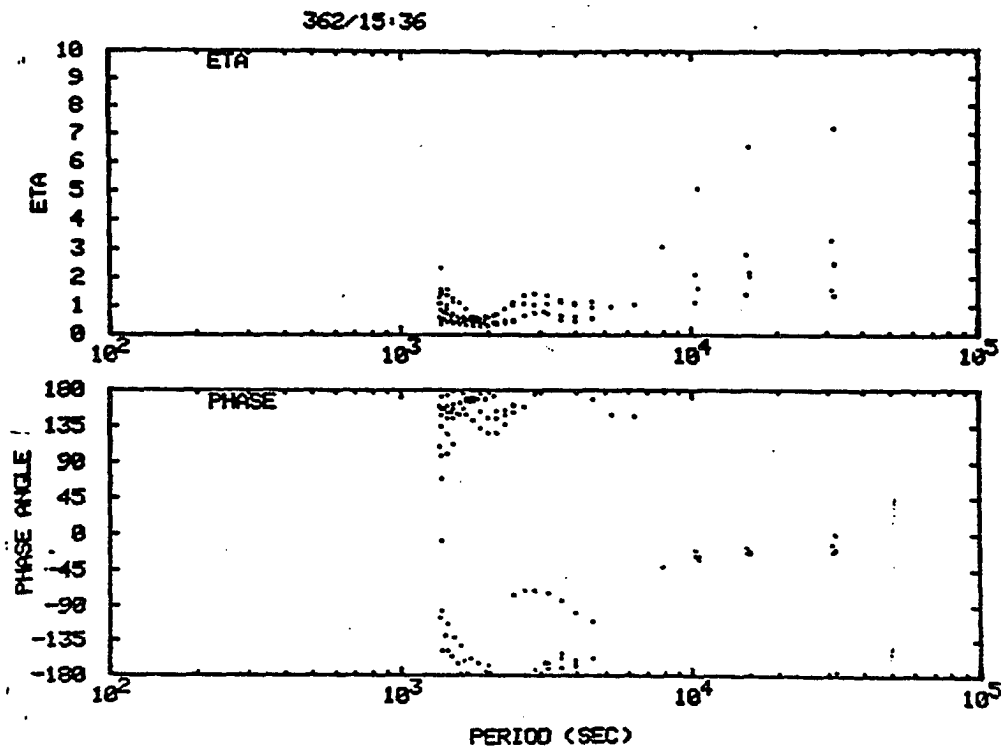
Fig. 5.7 This figure shows both η (top) and phase (bottom) as a function of wave period for the O_2 airglow emission. As in the previous figures, the points on the plot correspond to data with a magnitude squared coherency greater than 0.5. Note that η has features similar to those for the OH emission while the plot of the phase indicates that the intensity and temperature are out of phase over most of the frequencies.

equations we can solve for ρ. Using linear perturbation theory we get

$$\rho' \simeq -\bar{\rho}\frac{\theta'}{\bar{\theta}} + \frac{p'}{c_s^2}$$

5.2

where c_s^2 is the sound speed and the *primes* indicate the perturbation quantities.

For internal gravity waves, the perturbations are assumed to be primarily in temperature with the resulting pressure changes following the ideal gas law. This allows us to use the approximation $|\bar{\rho}_{z=0}\theta'/\bar{\theta}| \gg |p'/c_s^2|$. As a result, we can see that to a first

approximation, $\theta'/\bar{\theta} = -\rho'/\bar{\rho}$. Since the potential temperature is proportional to the temperature, T, and since the intensity of the emission is proportional to the density ρ, (ignoring any other loss mechanism such as quenching) we can rewrite Equation 5.2 as

$$\frac{T'}{\bar{T}} = -\frac{I'}{\bar{I}}$$

where I is the intensity. This implies that the fluctuations in temperature and in intensity will be 180° out of phase. Thus, we can see that linear gravity wave theory can explain the relation between the intensity and the temperature of the O_2 airglow emissions.

The major difference between the responses of the OH and O_2 airglow emissions to gravity wave perturbations is in the phase between intensity and temperature fluctuations. The production of OH* is primarily by the ozone mechanism, or $O^3+H \rightarrow$ OH*$+O_2$. This mechanism is very sensitive to ozone density which, in turn, is sensitive to atomic oxygen density. Thus, the intensity of OH is several steps away from the atomic oxygen density. O_2, on the other hand, is a result of $O+O+M \rightarrow O_2+M$, which is directly dependent on the square of the atomic oxygen density. Thus, if the atomic oxygen density is inversely dependent on temperature, then it is likely that O_2 will at least have an inverse relationship with the temperature. Another possible reason for the variability in the OH response is that the OH emission layer occurs in a region where the atomic oxygen density is changing very rapidly with height [Donahue et al., 1973]. This would make the OH intensity much more dependent on the emission height than O_2.

CHAPTER 6

Gravity Waves in the OH and O_2 Airglow: An Analysis of a Three Day Period

It is the purpose of this Chapter to examine several examples in terms of the gravity wave parameters mentioned in the previous Chapters, i.e., both the vertical and horizontal wavelengths, the propagation direction and speed, the wave period, and the relative amplitudes of the intensity and temperature fluctuations.

The analysis is concentrated on a 3-day period of data taken from Longyearbyen, Svalbard ($78°N$) near the end of 1986. At this latitude, sunlight never strikes the emitting layer, since the sun is never higher than $12°$ below the horizon. Thus, it is possible to acquire 24 hours of observation of the airglow each day. During this period, there was an intensive effort to obtain as much information from the airglow as possible. Both the spectrometer and the MSP were running during this period. The spectrometer was operating in a spatial scanning mode, set to observe in the geomagnetic directions of north, south, and east, at an elevation of $65°$ from the horizon. The MSP scanned the geomagnetic meridian from north to south every 16 seconds with a $1°$ resolution. The MSP and the spectrometer thus made coordinated measurements in the north and south directions.

The OH temperature and intensity for the entire period are shown in Figure 6.1. The uncertainty in the temperature calculations is represented by the bar in the upper left. The uncertainty in the intensity is represented by the bar on the right side of the plot. There are several features that are immediately obvious in the data. There is an oscillation with a 4-6 hour period in the first half of the data set. There are also

71

LYR OH DECEMBER 27-29 1986
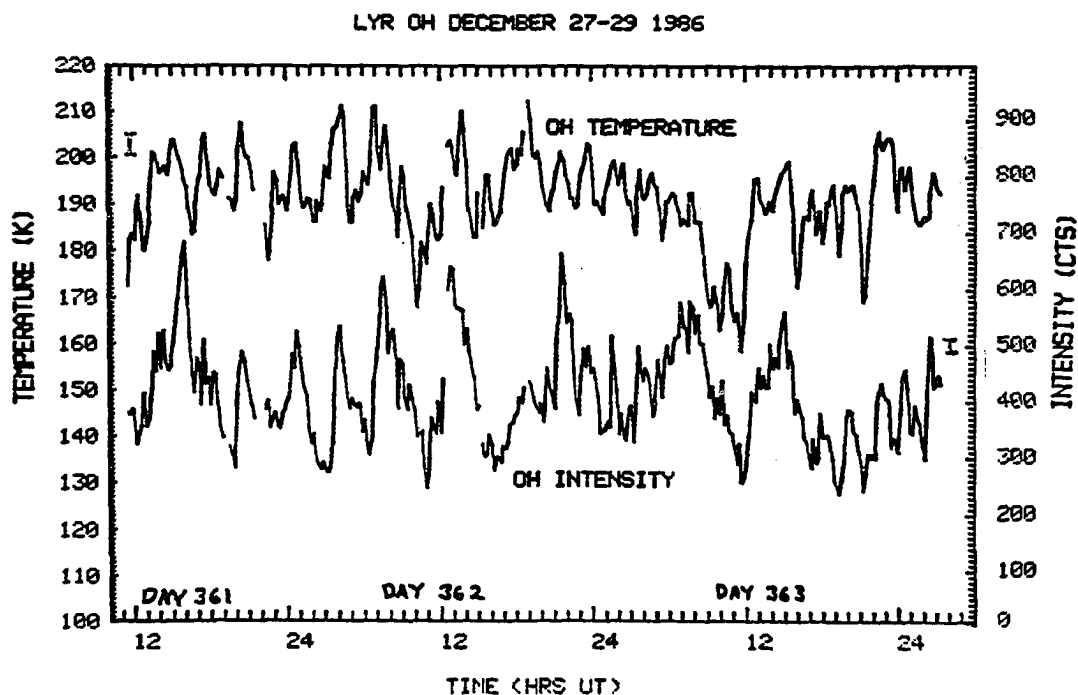
Fig. 6.1 60 hours of spectrometer data from Svalbard showing numerous wave-like oscillations. The top trace is of the OH temperature and the bottom is the intensity. The uncertainties in the temperature and intensity curves are represented by the bars in the upper-left and center-right respectively. There is an obvious oscillation during the first half of the data set with a period of 4-6 hours. There are also smaller scale oscillations in the data as well.

shorter period gravity waves present in the data such as the wave at about 20:00 UT on December 28.

The first example is not nearly so spectacular when observed with the spectrometer. Figure 6.2 shows the OH temperature and intensity as observed in the three directions by the spectrometer. The top three curves are the temperature as observed in the three geomagnetic directions of north, south, and east. The bottom three curves are the airglow intensity. The thickness of the top curve represents the ±5° uncertainty in the temperature traces and is the same for the second and third curves as well. Similarly,

the thickness of the fourth curve represents the uncertainty in the intensity measurements. Fluctuations which have amplitudes less than the thickness of the curves are not considered significant. The scales on the left and right apply to the thick curves of temperature and intensity respectively. The south and east components of the temperature have been offset by -20° and -40° respectively. The south and east components of the intensity have been offset by -200 counts and -400 counts respectively.

The major features seem to be large swings in the intensity with periods of 6 hours or more. The detailed fluctuations between the times of 16:30 UT and 20:00 UT hardly stand out as significant. It was only after observing the MSP data that this wave packet was discovered to be a coherent gravity wave. The fluctuations in temperature are of the same magnitude as the uncertainty and thus cannot be used in the interpretation. The fluctuations in the intensity traces are small but significant when compared with the uncertainty. The waves are somewhat more evident in the MSP data. Unfortunately, the MSP was not turned on until 17:45 UT and it did not record the first part of the wave sequence. Figure 6.3 shows an enlargement of the MSP data around the time of the gravity wave fluctuations on December 27.

The average wave period was approximately 35 minutes. The value of η in this example is not well defined since the fluctuations in the temperature were not clear. The intensity fluctuations were about 5% of the total intensity and the temperature fluctuations were hardly discernible and thus, must have been less than the 5°K uncertainty of the data, which implies an amplitude of less than 5%. Thus the value of η was on the order of one or two, which is not in agreement with the predicted values for a wave of this period [*Walterscheid et al.*, 1987; *Hickey*, 1987a,b]. Both the *Walterscheid* and *Hickey* models predict a value of $\eta > 5$ for a wave of this period. One explanation for this discrepancy, which was given in Chapter 5, is that the field-of-view of the spectrometer was too large to observe the full amplitude of waves of this scale.

LYR OH DEC 27, 1986

TEMP (N)
TEMP (S)
TEMP (E)
INT(N)
INT(S)
INT(E)

TEMPERATURE (K)

INTENSITY (CTS)

TIME (HRS UT)
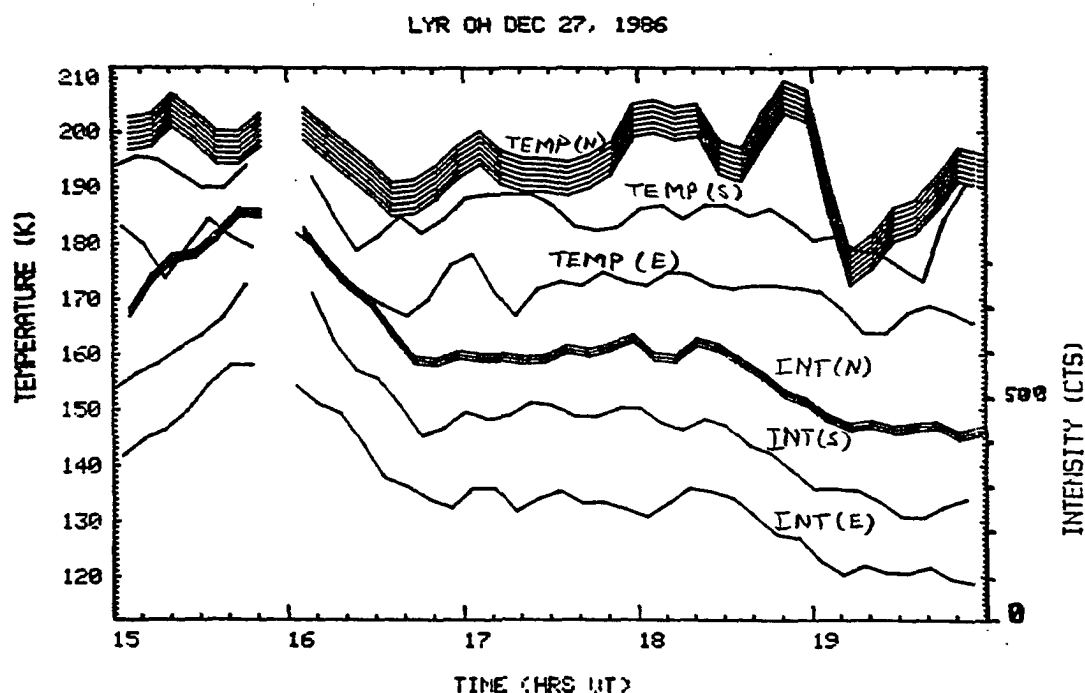
Fig. 6.2 Time series of OH temperature and intensity for the wave packet beginning at 16:30 UT on December 27. The curves are arranged such that the top three curves are the OH temperature observed in the three directions of geomagnetic north, south, and east, all at an elevation of 65° above the horizon. The bottom three curves are of the intensity. The 5°K uncertainty in the temperature measurments is represented by the thickness of the top curve. The uncertainty of the intensity measurements is represented by the thickness of the fouth curve. The scale values apply to the thickened traces. The wave packet of interest is only observable in the OH intensity curves and begins at about 16:30 UT.
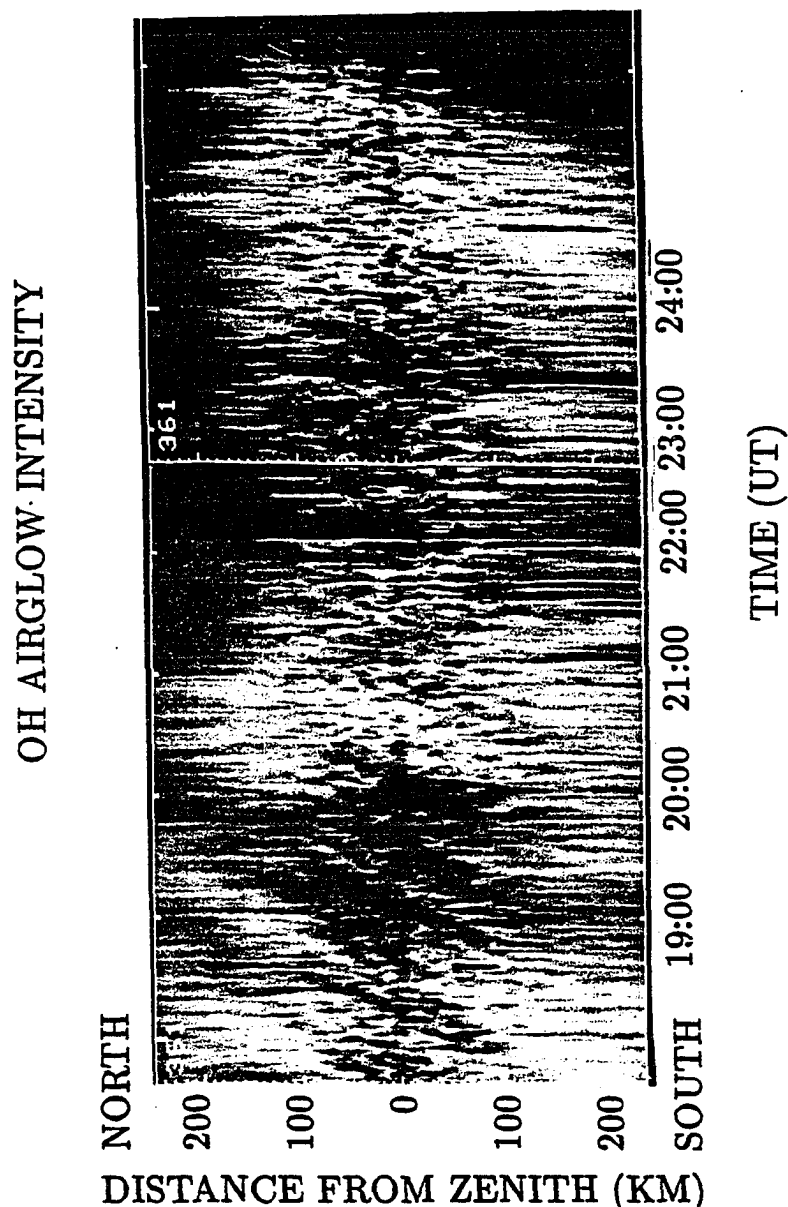
Fig. 6.3 Detail of the MSP grayshade plot of the wave packet beginning at 16:30 UT on December 27, 1987. The X-axis is time, the Y-axis is distance from zenith, and the grayshade represents the OH airglow intensity. The gravity waves appear as diagonal stripes in the grayshade.

Horizontal wave direction and horizontal phase speed were measured by matching up wave crests and wave troughs and determining the arrival times of each feature in each direction. Table 6.1 shows the arrival times of two complete waves in the three directions. The last two columns in Table 6.1 are the calculated source direction, in geomagnetic coordinates, and the phase speed, in meters per second. There was some ambiguity in the matching of the crests and troughs, especially for the data from eastward direction. The match was confirmed for the north and south directions by comparison with the MSP. The eastward direction had two reasonable correlations and the match was chosen by determination of the most consistent results for direction and wave speed. These results are shown in Table 6.1.

Table 6.1

Arrival Times for the Crests and Troughs of the Wave Packet on December 27.

Phase	North	South	East	Direction	Velocity
trough	17:10±:05	17:00±:05	17:45±:05	263±5°	12±3 m/s
crest	17:39	17:10	18:00	256°	12 m/s
trough	17:45	17:20	18:15	254°	12 m/s
crest	18:00	17:35	18:20	249°	14 m/s
Mean				255°	13 m/s
Standard Dev.				5°	1 m/s

The wave came from a direction of 255°±5° which is approximately geomagnetic west. The magnetic declination is 45° west, which implies that the wave came from a direction of 210° geographic, or 30° west of south.

The horizontal propagation velocity for this wave was only 13 m/s. The horizontal velocity can be used, along with the wave period of 35 minutes, to obtain the horizontal wavelength which in this case is on the order of 27 km. This can be checked by comparison with the MSP data. In Figure 6.3, the observed meridional wavelength of about 100 km
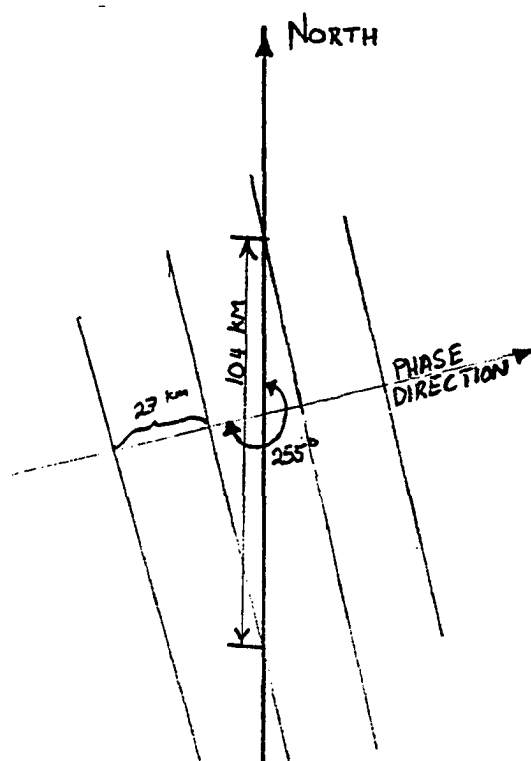
Fig. 6.4   The projection of a wave with a horizontal wavelength of 27 km propagating from a direction of 255° will result in a meridional wavelength of 104 km. This agrees well with meridional wavelength as observed with the MSP data shown in Figure 6.3.

projects to a 27 km wave traveling from a direction of 255°. It should be noted that there is no correction for any Doppler effects on wave period and propagation direction. The geometry of the wave is shown in Figure 6.4 and the resulting meridional wavelength is 104 km. It should be noted that the horizontal wavelength of 27 km is more than twice the 12 km field-of-view of the spectrometer. It is, therefore, unlikely that the large field-of-view is the source of the small amplitude in the observed temperature fluctuations.

Figure 6.5 shows the O_2 and OH temperatures observed with the spectrometer on December 27, 1986. There is a wavelike structure in the O_2 temperature between 16:00

UT and 18:00 UT which corresponds very well to the observed wave in the OH intensity. The OH temperature on the other hand, does not show any obvious wavelike structures with 20-30 minute periods. There is also an increase of about a factor of three in the amplitude of the structures between the O_2 and the OH temperature. This is in good agreement with the theory of vertically propagating gravity waves which have amplitudes that are inversely proportional to the number density of the atmosphere. There is very little time lag between the structures in the O_2 temperature at 16:00 UT and those in the OH intensity, which implies that the vertical propagation is quite rapid and that the vertical wavelength is larger than the 8 km separation between the layers. A long vertical wavelength associated with a short period gravity waves agrees well with classical gravity wave theory.

The next example begins at 8:00 UT on the following day (i.e. December 28, 1986), as shown by the spectrometer data in Figure 6.6, and as with the previous example, the wave propagates from the south as can be seen in Figure 6.7. This wave has a period of about 70 minutes and the amplitudes of the OH intensity and temperature are such that the value of η for this wave is approximately three. According to the calculations by *Hickey* [1987b], the wavelength of a wave with a period of 70 minutes and a value of $\eta = 3$ is slightly less than 100 km. This will be shown to be the case for this gravity wave as well.

LYR OH AND O2 DEC. 27, 1986
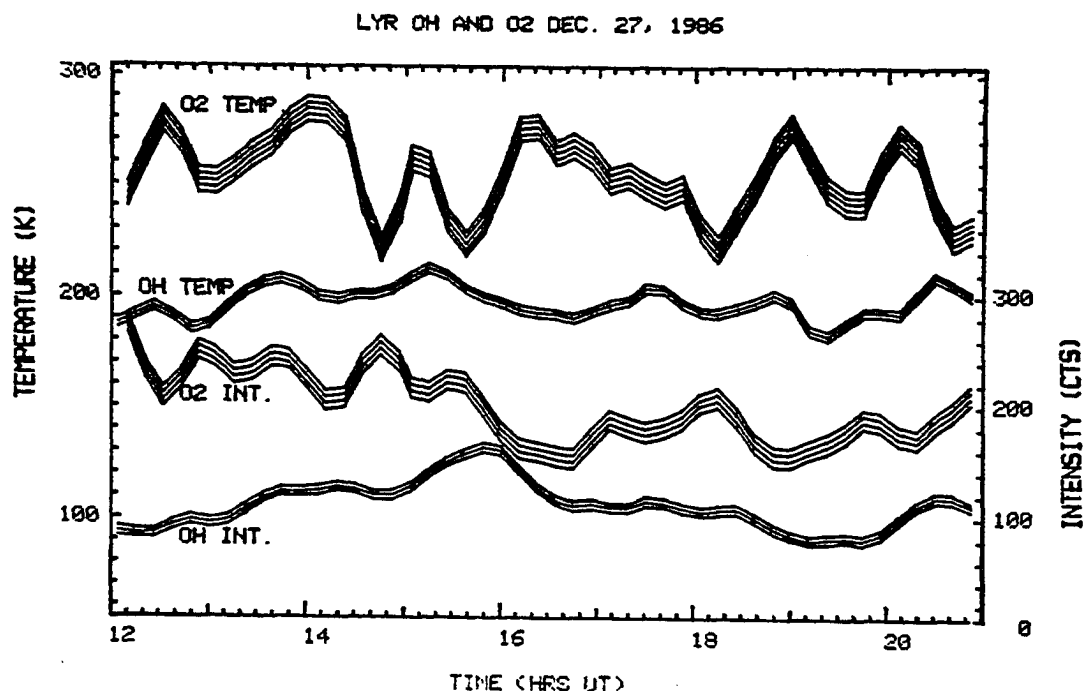
Fig. 6.5 The O_2 temperature (top) and OH temperature (bottom) for the the period around the observed gravity wave on December 27, 1986. Note that there is evidence of a wavelike structure in the O_2 temperature between 16:00 UT and 18:00 UT while there is very little evidence of a similar wave in the OH.

The arrival times of the wave crests and troughs are listed in Table 6.2.

Table 6.2

Arrival Times of Wave Crests and Troughs for the Wave Packet Begining at 8:00 UT December 28 1986.

Phase	North	South	East	Direction	Velocity
trough	11:00±:05	10:45±:05	11:00±:05	225±30°	46±10 m/s
crest	11:40	11:25	11:35	199°	63 m/s
trough	12:05	11:50	12:00	199°	63 m/s
crest	13:05	12:45	12:50	180°	50 m/s
trough	13:30	13:10	13:10	135°	35 m/s
Mean				187°	51 m/s
Standard Dev.				35°	12 m/s

LYR OH DEC 28, 1986
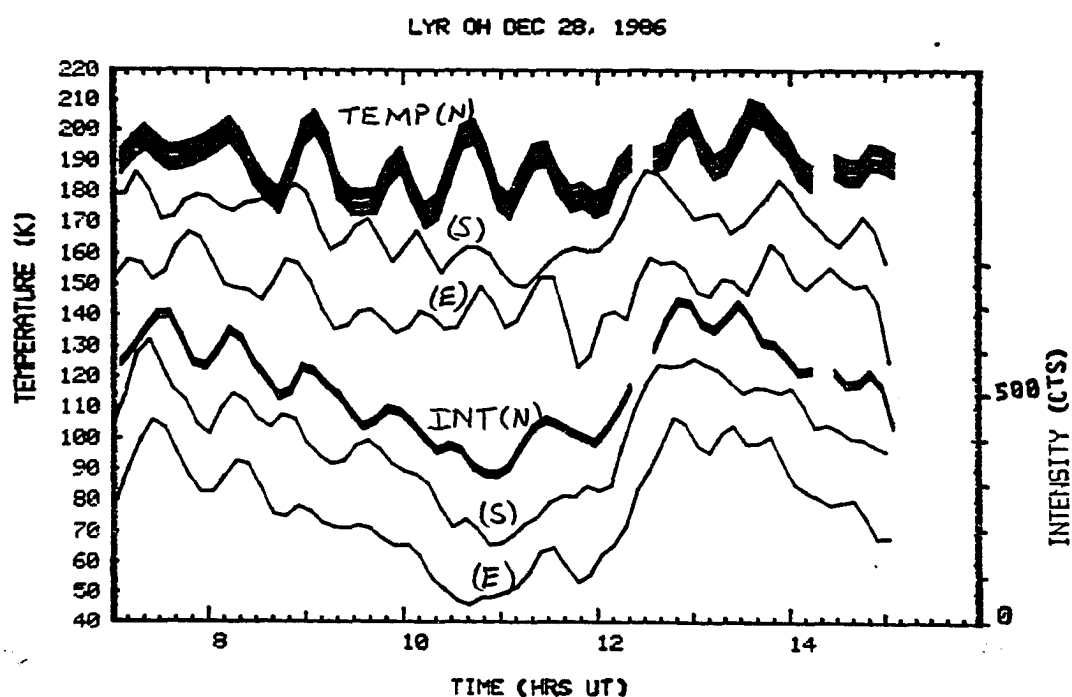
Fig. 6.6 OH temperature and intensity, for the wave beginning at 8:00 UT on December 28, 1986. As in Figure 6.2, the top three curves represent the OH temperature as observed in the three directions of north (top), south (middle), and east (bottom). The bottom three curves represent the intensity. The uncertainty in the temperature and intensity measurements are represented by the thickness of the first and fourth curves and the scale values apply to the thickened curves. Note that the wave occurs on the downward phase of the longer, 5-hour wave.
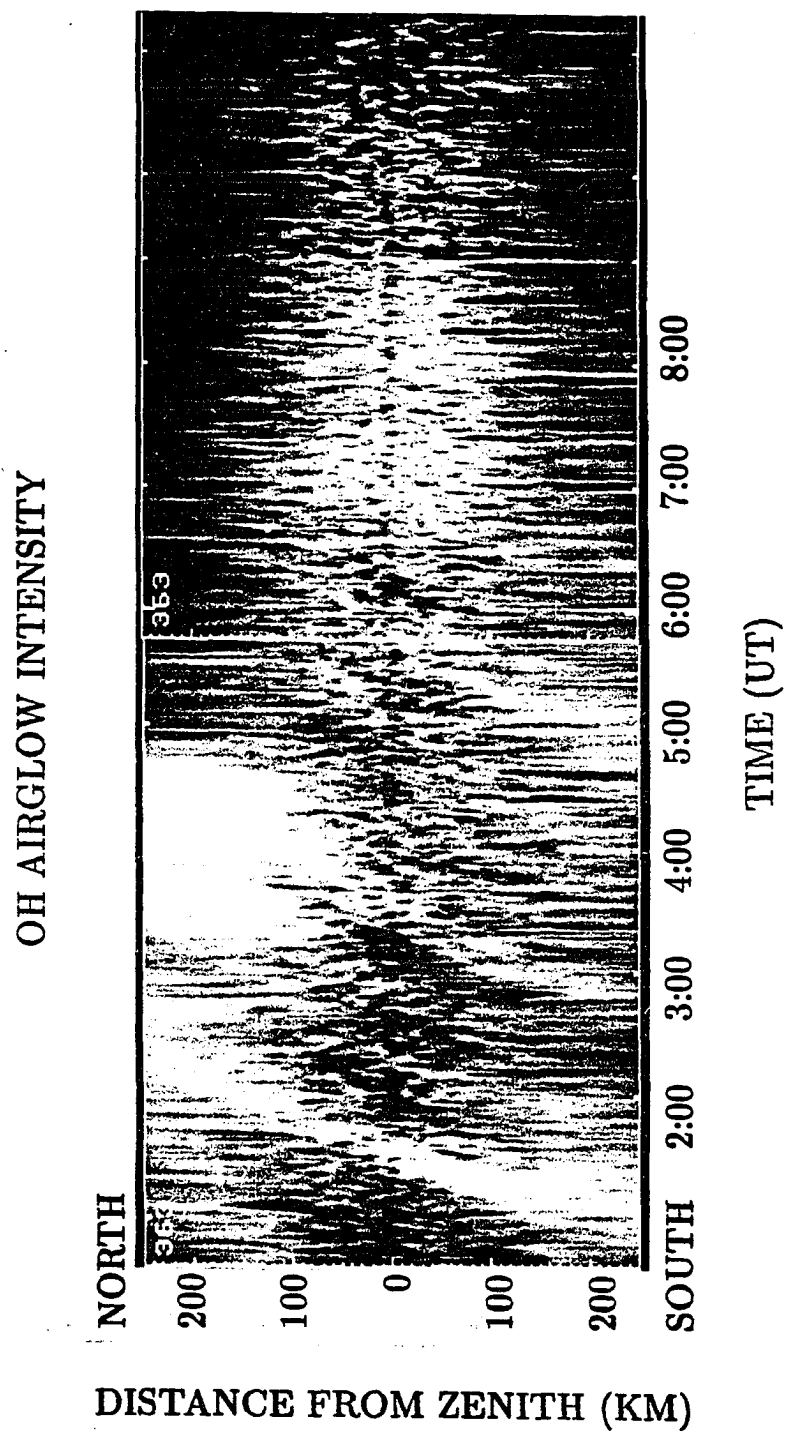
Fig. 6.7 Detail of the meridional OH intensity as observed by the MSP for the data around 8:00 UT on December 28 1986. Note the northward propagating features which correspond to propagating enhancements in intensity associated with a gravity wave.

As can be seen in this Table, the wave came from a direction of $187°\pm35°$ with a phase speed of about 50 m/s. There is significantly more deviation from the average values of the direction and velocity than in the previous example. There are several possible reasons for this. The most probable reason is the uncertainty in the arrival times of the crests and troughs. The time resolution of the data is nine minutes and thus, the uncertainty in the arrival times is somewhat less (allowing for some interpolation), which is about 10% of the time of propagation between observation directions. This will result in an uncertainty in the calculated direction of propagation on the order of 10%, or $30°$. In the previous example the propagation speed was much slower and thus, the nine minute sample rate was a smaller proportion of the propagation time.

The phase velocity is about 50 m/s which indicates a horizontal wavelength of about 60 km. Since the propagation direction is almost meridional, the observed meridional wavelength should be of the same size. The MSP plot indicates a meridional wavelength of about 80 km which is slightly larger than that observed by the spectrometer, but it is within the uncertainty in the spectrometer based calculations.

The last example is of the wave which begins at about 20:00 UT on December 28, 1986. Figure 6.8 contains six curves; the top three are again of the OH temperature as measured in the three geomagnetic directions of north (top), south (middle), and east (bottom). The bottom three curves are of the OH intensity. Begining about 19:00 UT on December 28, and running through about 3:00 UT on December 29, is an obvious, well defined wave packet. In this example, the wave has a period of about 110 minutes, but with quite a bit of variability. The relative amplitudes of the intensity and the temperature result in a value of $\eta = 4$. According to *Hickey* [1987], this would imply a horizontal wavelength of about 100 km. The waves can also be seen in the MSP data in Figure 6.9.

LYR OH DEC 28-29 1986
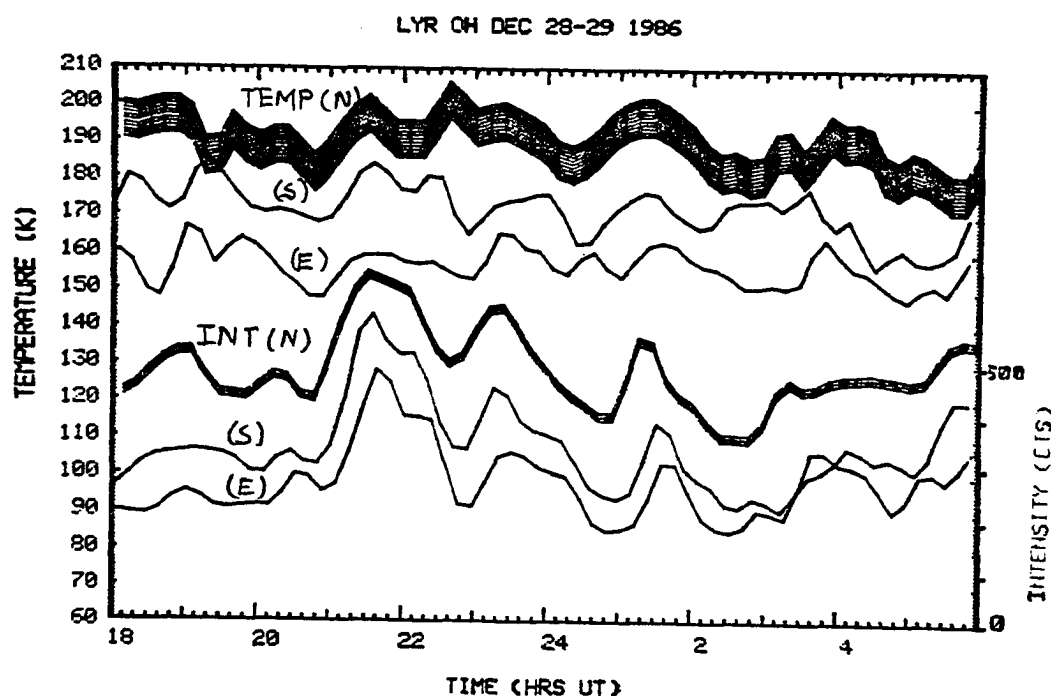
Fig. 6.8 Time series from December 28, of OH temperature and intensity. As in Figure 6.2, the top three curves represent the components for the geomagnetic directions of north (top), south (middle), and east (bottom) taken at an angle of 30° from zenith. As in Figure 6.2, the thickness of the first and fourth curves represents the uncertainty of the temperature and intensity and the scale values refer to the thickened curves.

OH AIRGLOW INTENSITY

NORTH

200

100

0

100

200

SOUTH

5:00 6:00 7:00 8:00 9:00 10:00 11:00 12:00

TIME (UT)

DISTANCE FROM ZENITH (KM)
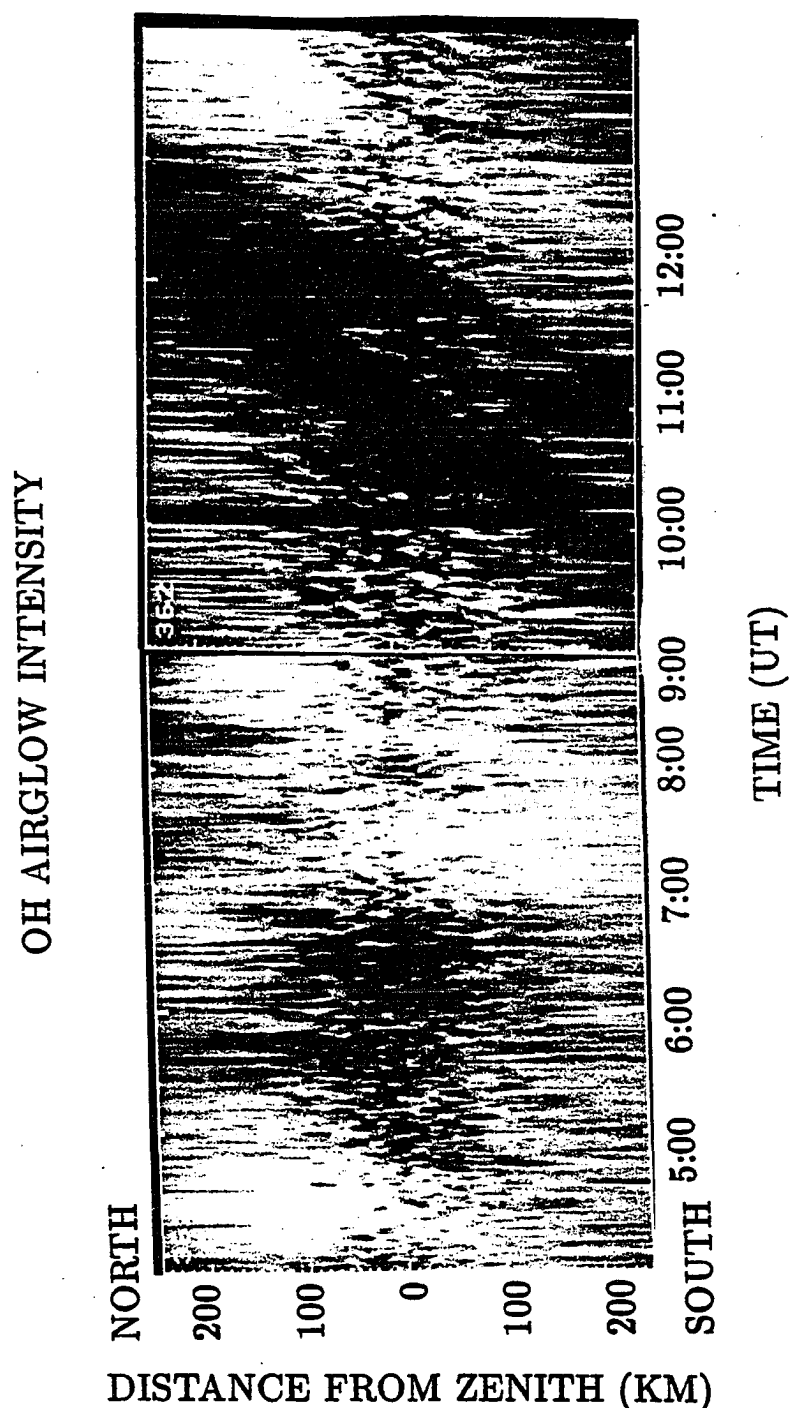
Fig. 6.9   Grayshade plot of the MSP data from December 28, 1986. The X-axis is time, the Y-axis is horizontal distance, and the brightness represents airglow intensity. The wave-like pattern which appears as striations from the lower right to the upper left are, in fact, traveling enhancements in brightness propagating from south to north.

The arrival times of peaks and valleys of the oscillations in intensity are listed in Table 6.3. The uncertainty in the time of the crests and troughs is, again, the largest source of error and thus, the most probable source of the large deviations in the arrival directions.

Table 6.3

Arrival Times of Wave Crests and Troughs for December 28-29, 1986.

Phase	North	South	East	Direction	Velocity
crest	20:35±:05	20:10±:05	20:25±:05	192±40°	39±15 m/s
trough	20:55	20:40	20:45	168°	62 m/s
crest	21:35	21:20	21:35	225°	47 m/s
trough	22:55	22:40	22:55	225°	47 m/s
crest	23:40	23:20	23:20	135°	35 m/s
trough	24:50	24:45	1:00	110°	38 m/s
crest	1:40	1:20	1:30	180°	50 m/s
Mean				174°	47 m/s
Standard Dev.				35°	10 m/s

The average arrival direction is about 174° geomagnetic and the propagation speed is about 47 m/s as can be seen in Table 6.3. The waves came from a southerly direction which corresponds to a direction of about 130° in geographic coordinates. The horizontal wavelength of the waves should be calculated on an individual basis since the periods are so variable. The first wave of the packet has a period of about 70 ± 10 minutes and a phase speed of about 45 m/s. This corresponds to a wavelength of 190 ± 15 km. The average wavelength for the whole wave packet is about 250 ± 20km. This was more than twice the horizontal wavelength that was predicted by *Hickey* [1987b].

As in the previous example, the propagation is almost entirely meridional and thus, the meridional wavelength observed by the MSP should be fairly close to the actual horizontal wavelength. As can be seen in Figure 6.9, the average wavelength is about 220 km which agrees with the spectrometer calculations.

The final piece of information that we can gain from the data is the vertical wavelength. The O_2 and OH temperatures are shown in Figure 6.10 and the wave can be seen in the OH temperature. There is a large amplitude wave in the O_2 temperature between 22:00 UT and 24:00 UT and the period is approximately 70 minutes which is a shorter period than was observed in the OH. It is quite difficult to trace corresponding wave peaks between the OH and O_2 temperatures. The most likely match between the two traces can be determined by assuming a phase lag of 1-2 hours between the two layers. The peaks in the O_2 temperature at 23:00 UT, 24:15 UT, and 2:55 UT would correspond to peaks in the OH temperature at 23:55 UT, 1:50 UT, and 3:50 UT respectively. The phase between the waves would then be slightly larger than 180° implying a vertical wavelength of 14 km. Once again, the factor of three increase in the amplitude between OH and O_2 curves would be expected due to the decrease in the density of the atmosphere.

6.6 Overview of the Three Day Period

The three days of uninterrupted airglow data have several interesting features which are worth mentioning. Throughout the data set there exists an oscillation in the temperatures and especially the intensities of the OH and O_2 airglow with a period of between four and six hours. This wave-like motion has a northward meridional phase velocity. The amplitude of this wave is about 10°K, or about 7% of the mean temperature. The fluctuations in intensity are on the order of 35% of the mean intensity. This results in a value of $\eta \simeq 5$. According the theory of gravity wave interaction with OH airglow emission, put forth by *Hickey* [1987b], this should be the result of a gravity wave with a horizontal wavelength on the order of 100 km. The measurements show that the wavelength is closer to 500 km. This does not agree well with the 100 km predicted by

LYR OH AND O2   DEC 28,1986

TIME (HRS UT)
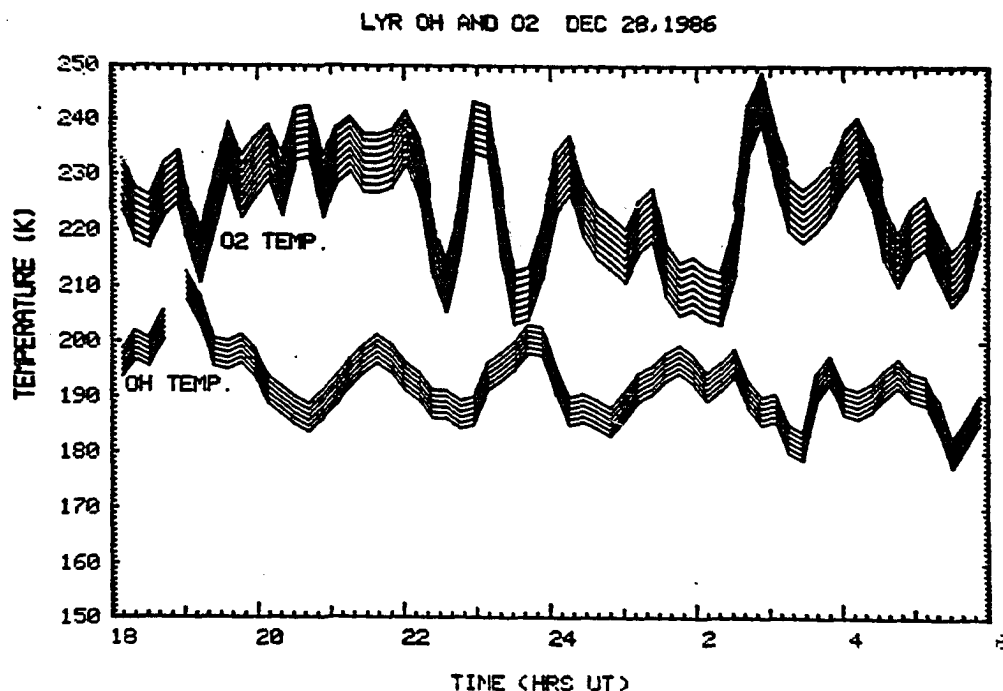
Fig. 6.10 O_2 and OH temperatures for the same period as in Figure 6.8. There are fluctuations in the O_2 temperature which may correspond to the gravity wave in the OH temperature. A probable match might be that the peaks in the O_2 temperature at 23:00 UT, 24:15 UT, and 2:55 UT would correspond to peaks in the OH temperature at 23:55 UT, 1:50 UT, and 3:50 UT respectively.

Hickey. However, I am so encouraged by the agreement in the trend of the parameter η and the phase between the model and the data that I feel justified in proposing that the model is subject to several assumptions and may be adjusted to fit the observations [*Hickey*, private communications].

Along with the large-scale wave are several smaller waves with periods of approximately one to two hours. These smaller waves have relative amplitudes of OH intensity and temperature which yield a value of $\eta = 1$. The smaller waves occur on the decreasing phase of the wave in both OH temperature and intensity. The first small wave packet occurs at about 16:30 UT on December 27 and has a period of 30 minuites. The second

wave packet occurs at about 6:00 UT on the following day and has a period of just over 60 minutes. The last of the shorter waves occurs at 18:00 UT on December 28 and has a period of almost two hours. Each of these waves is larger than the last and the propagation direction progresses from geographic southwest for the first wave to south for the second and just east of south for the last. The amplitudes of the waves also increased from less than 5°K for the first to almost 10°K for the last. The increase in amplitude is even more evident in the OH intensity where the final wave set has an amplitude of almost 50%.

The most obvious interpretation is that there was a strong gravity wave source south of the observing site which was traveling eastward. Examination of the 500 mb weather maps for that period indicated that there was a low pressure system which traversed the North Atlantic Ocean and was in the direction of the source of the observed gravity waves at a distance of 1000-2000 km.

The key may lie in the relationship between the three observed wave packets and the larger scale 4-6 hour wave. There are several studies which suggest that gravity waves can and do interact with the mean flow [*Holton*, 1978; *Dunkerton*, 1982; and *Holton and Zhu*, 1984; *Fritts and Vincent*, 1987]. It is possible that the large scale waves were produced several hundreds of kilometers from the observation point and the smaller scale waves were secondary gravity waves which interacted with the larger wave. The theories imply that the large gravity waves may be seen as a reversing mean flow and that during one phase of the large wave, saturation occurs while during the opposite phase, the shorter period wave is either transmitted or even enhanced. This would explain why the short period waves seemed to occur only during one phase of the larger scale waves.

Another characteristic that could be important is the progressive increase in wave period from the first to the last of the smaller waves. One possibility is that the change in observed period was the result of Doppler shifting by the mean wind. It is likely that

the mean flow is towards the north-west (from the south-east) and thus, the first wave is Doppler shifted to a higher frequency. The problem with this interpretation is that the phase velocity of the first wave was much slower than that of the other waves. Thus, Doppler shifting is not a likely cause of the change in frequency. Another possibility is that the environment regulating the interaction between the short and long waves was changing with time.

CHAPTER 7

Conclusions

7.1 The Airglow Parameters of η and Phase

The effects of gravity waves on the airglow may be seen in terms of temporal and spatial variations in the atmospheric temperature and density deduced from observations of the airglow intensity and rotational temperature. Gravity waves are described in terms of amplitude, phase, and wavelength. In the airglow observations, the amplitude is related to the parameter η which is the ratio of the observed amplitudes of the oscillations in intensity and temperature; the phase is the phase angle between the oscillations in intensity and temperature, and the wavelength is the distance, both vertically and horizontally, between the points of equal phase.

In this study, the relationship between the intensity and temperature of both the OH and the O_2 emissions have been measured and compared with recent theories relating the airglow pertubations to gravity wave action. In order to do this, it was necessary to calculate the two parameters from the observations which relate the temperature fluctuations to the intensity fluctuations.

The ratio of the amplitudes of the fluctuations, η, and the phase angle between the temperature and intensity fluctuations were both calculated as functions of wave period in order to compare them with the model of *Walterscheid et al.* [1987] and subsequent modifications to their model by *Hickey* [1987a,b]. The observed values of η and phase are both functions of wave period, but not in the way predicted by the linear model of *Walterscheid et al.*. In general, we observe that the parameter η increases with wave

90

period starting at a value of $\eta = 1$ for waves with periods between 10 and 60 minutes. *Walterscheid et al.* predicted that η should decrease with wave period and that this was dependent on the scale height of O.

The addition of nonlinear terms such as thermal conductivity and eddy diffusion to the *Walterscheid et al.* model by *Hickey* [1987a,b] seems to have brought the theory into fair agreement with the observational data. In this model, η is dependent on the horizontal wavelength which dominates over any dependence on the scale height of O, although this may still be important.

Even with the modifications by *Hickey*, the *Walterscheid et al.* model predicts values of η between 5 and 10 for short periods (10^3 to 10^4 seconds). Our observations show that the observed values are closer to one. This discrepancy has not been resolved although it may be simply a result of the observing geometry, i.e. the shorter period waves may correspond to vertical wavelengths shorter than the emitting layer thickness and/or horizontal wavelengths shorter than the field of view of the spectrometer.

The temperature and intensity fluctuations in the OH emission were within $40°$of being in phase for all of the frequencies measured. The observed phase angle was substantially different than that predicted by the theories of both *Walterscheid et al.* and *Hickey*. However, *Hickey's* modifications to the theory of the phase relationship effectively eliminated the difference between observations and theory for the long period waves(10^4 to 10^5 seconds) Any small differences between theory and observations, for long period waves, can be accounted for by either changes in horizontal wavelengths of the waves or by Doppler shifting of the wave period by the mean wind.

The temperature and intensity fluctuations in O_2 were $180°$ out-of-phase for all but the very long period waves. The ratio of the amplitudes, or η, was similar to that observed for the OH emission. The only theory that has examined the O_2 emission [*Weinstock*, 1978] has been criticized, [*Hines and Tarasick*, 1987], but no alternative

theory has been proposed. In the meantime, the 180° phase difference is expected from linear theory, but the η values are awaiting an explanation.

7.2 The Analysis of Gravity Waves from Airglow Observation

One of the best examples of gravity wave effects in the airglow is a continuous 60-hour interval (December 27-30, 1986) of observations from Svalbard, showing several examples of gravity wave effects with periods ranging from 30 minutes to 5 hours. A significant detail of the smaller waves is that they were observed only on the trailing edge of the larger wave, implying that there was some wave-wave interaction. The periods and horizontal wavelengths of the smaller waves started at 30 minutes and 30 km, respectively, and got progressively longer to values of 120 minutes and 250 km for the third wave. The vertical wavelength was very difficult to measure, but indications were that the shortest wave had the largest vertical wavelength as would be expected from classical gravity wave theory.

The analysis indicates that although both the smaller waves and the larger wave were propagating poleward, the smaller waves seemed to originate from a source moving from east to west. The most obvious source was a low pressure system which lay in the North Atlantic. The shorter waves seemed to come from a moving source which tracked the low pressure system as it traversed the North Atlantic from a position south-west of Svalbard at the beginning of December 27, 1986 to a position south of south-east of Svalbard on December 30.

However difficult it may be to measure all of these parameters simultaneously, the apparent convergence of the observations with the theory is very encouraging. Suggestions for further studies include combined measurements of the type used for this thesis along with lidar or radar measurements which obtain much better measurements of the vertical wavelengths and phase speeds. Better measurements of the horizontal wave field

could be made by using several meridian scanning devices along with imagers with high spectral resolution. One of the more difficult measurements to make would be of the horizontal structure of the rotational temperature of the airglow emissions. These types of measurements would be very useful and provide much needed data for the theoretical modeling of the interaction of gravity waves with the airglow. Finally, it is very important to account for any Doppler shifting of the waves due to the mean flow. For this reason it is important to include some method of determining the mean wind in any comprehensive study of gravity waves.

APPENDIX A

Synthetic Spectra of OH and O_2

Airglow spectra consist of vibration-rotation bands of numerous species of the atmosphere. In this thesis, only the airglow emission spectra of the diatomic molecules O_2 and the OH radical are considered. The analysis technique required the use of synthetic spectra to determine the rotational temperature of the emitting molecule. The synthetic spectra consist of individual rotational lines grouped into vibrational bands. It is thus required to calculate a wavelength and a line intensities for each rotational line. Elementry quantum theory states that the wavelength of each line is determined by the difference in energy between the initial and final states of a molecule as it undergoes a transition. The intensity of a line depends on the number of molecules in the initial state and a *transition probability* for each transition. The following description for emission spectra of diatomic molecules will set the groundwork for the discussion of the analysis technique.

The energy absorbed or emitted, during a given molecular transition, is the sum of the changes of rotational and vibrational energies, $E_v(v)$ and $E_r(J)$. The vibrational and rotational energies are often rewritten in terms of *term values* such that

$$E_n(v, J) = E_v(v) + E_r(J) = hc[G(v) + F(J)]$$

where $G(v)$ and $F(J)$ are the vibrational and rotational term values respectively and v and J are the vibrational and rotational quantum numbers. There are numerous influencing factors that need to be considered in the calculation of the term values. As a result, each molecule will have specific term values and specific vibrational and rotational constants that are used in calculating the term values.

94

The vibrational term value is determined from the formula given in *Herzberg* [1950] as

$$G(v) = w_e(v + \tfrac{1}{2}) - w_e x_e(v + \tfrac{1}{2})^2 + w_e y_e(v + \tfrac{1}{2})^3 + \cdots \qquad A.1$$

where w_e, x_e, and y_e are vibrational constants. With the vibrational constants for the OH molecule, taken from *Krassovsky* [1962], the term value becomes

$$G(v) = 3739.90(v + \tfrac{1}{2}) - 84.965(v + \tfrac{1}{2})^2 + 0.5398(v + \tfrac{1}{2})^3 + \cdots$$

The origins of a band, defined by the transition from the $v' = 6$ state to the $v'' = 2$ state, can then be determined by taking the difference between $G(v = 6)$ and $G(v = 2)$.

The rotational energies are determined by somewhat more complicated formulas

$$^2\Pi_{3/2} F_1(J) = B_v\left[(J + \tfrac{1}{2}) - 1 - \tfrac{1}{2}\sqrt{4(J + \tfrac{1}{2})^2 + Y_v(Y_v - 4)}\right] - D_v J^4$$

$$^2\Pi_{1/2} F_2(J) = B_v\left[(J + \tfrac{1}{2}) - 1 + \tfrac{1}{2}\sqrt{4(J + \tfrac{1}{2})^2 + Y_v(Y_v - 4)}\right] - D_v J^4$$

$$^2\Pi_{3/2} F_1(K) = B_v\left[K(K + 1)^2 - 1 - \tfrac{1}{2}\sqrt{4(J + \tfrac{1}{2})^2 + Y_v(Y_v - 4)}\right] - D_v K^2(K + 1)^2$$

$$^2\Pi_{1/2} F_2(K) = B_v\left[K - 1 + \tfrac{1}{2}\sqrt{4K^2 + Y_v(Y_v - 4)}\right] - D_v K^2(K + 1)^2$$

where $K = J - \tfrac{1}{2}$ for $^2\Pi_{3/2}$ and $K = J + \tfrac{1}{2}$ for $^2\Pi_{1/2}$. The vibrational constants are $B_v = 18.867\text{cm}^{-1} - 0.708\text{cm}^{-1}(v + \tfrac{1}{2}) + 0.00207\text{cm}^{-1}(v + \tfrac{1}{2})^2$ and $D_v = 00018\text{cm}^{-1}$ where v is the final vibrational state. It should be noted that there will be a splitting of the spectral lines produced by two different ground states, as indicated by the spectroscopic notation $^2\Pi_{3/2}$ and $^2\Pi_{1/2}$. There are two slightly different levels of the ground state for diatomic molecules as defined by the projection of the electronic spin vector and the electronic orbital vector onto the internuclear axis. The $^2\Pi_{1/2}$ state has a slightly higher energy level and thus, there is a splitting of the emission lines. There is even further splitting of the lines, called λ-*type doubling*, due to the interaction of the orbital angular momentum and the rotation of the nuclei. For the spectral resolution considered in this thesis, this was not considered important.

Given a specific vibrational transition such as the (6-2) transition, the position of the rotational lines will be defined by calculating the energy for each term value for $J = 0, 1, 2, 3, \ldots$ It should be noted that there are three branches defined by the selection rules $\Delta J = 1$ (R-branch), $\Delta J = -1$ (P-branch) and $\Delta J = 0$ (Q-branch).

Similar formulas for the O_2 molecule can also be found in *Krassovsky* [1962]. In the case of the O_2 molecule the vibrational constants are different for the initial and final vibrational states. Thus the vibrational term value in Equation A.1 will become

$$G(v) = w_e'(v' + \tfrac{1}{2}) - w_e'x_e'(v' + \tfrac{1}{2})^2 + w_e'y_e'(v' + \tfrac{1}{2})^3 + \cdots$$

$$- w_e''(v'' + \tfrac{1}{2}) + w_e''x_e''(v'' + \tfrac{1}{2})^2 - w_e''y_e''(v'' + \tfrac{1}{2})^3 + \cdots$$

For the $O_2(0-1)$ atmospheric band, the constants are $w_e' = 1432.6874$, $w_e'' = 1580.3613$, $w_e'x_e' = 13.95008$, $w_e''x_e'' = 12.0730$, $w_e'y_e' = -0.01075$, $w_e''y_e'' = 0.0546$, $w_e'z_e' = 0.0000$, and $w_e''z_e'' = -0.00143$. The rotational energies for the O_2 molecule are determined from the formula

$$F(K) = B_v K(K + 1) - D_v K^2 (K + 1)^2$$

for $J = K$ and $J = K \pm 1$ where $B_v = 1.400416 - 0.018170(v' + \tfrac{1}{2}) - 0.000043(v' + \tfrac{1}{2})^2$, and $D_v = 5.356 \times 10^{-6} - 0.007 \times 10^{-6}(v' + \tfrac{1}{2})$ and v is the final vibrational state. For each of the branches, the above formula will become

$${}^P P(J', K') = F(K') - F_2(J' + 1, K' + 1)$$

$${}^P Q(J', K') = F(K') - F_3(J', K' + 1)$$

$${}^R Q(J', K') = F(K') - F_1(J', K' - 1)$$

$${}^R R(J', K') = F(K') - F_2(J' - 1, K' - 1)$$

$$F_1 = B_v[K(K + 1) - (2K + 3)] - \lambda - \sqrt{(2K + 3)^2 B_v^2 + \lambda^2 - 2\lambda B_v} \qquad K = J - 1$$

$$F_2 = B_v K(K + 1) \qquad K = J$$

$$F_3 = B_v[K(K + 1) - (2K - 1)] - \lambda - \sqrt{(2K - 1)^2 B_v^2 + \lambda^2 - 2\lambda B_v} \qquad K = J + 1$$

where $\lambda = 1.985$ for the $O_2(0-1)$ band.

With the above information one can calculate the energies of the transitions and thus, the wavenumbers of the lines of the emission spectra for OH and O_2. The wavenumber of an emission line for a transition from the state defined as $|v', J'\rangle$ to the lower energy state $|v'', J''\rangle$ is the difference in the energy of the two states

$$\nu_{em} = E(v', J') - E(v'', J'').$$

The next step in calculating a synthetic spectrum is to calculate the intensity of each of the rotational lines. In the absence of quenching, the intensity of a given line in the spectra of a molecule is proportional to the number of molecules in the upper state, $N_{v'J'}$, and a transition probability, A. The rate at which molecules will undergo transition is

$$\frac{dN_{v'J'}(t)}{dt} = \sum_{v'' < v'} \sum_{J''} A(v'J' \to v''J'')N_{v'J'}(t)$$

After integration,

$$N_{v'J'}(t) = N_{v'J'}(t = 0)\exp\left[-\sum_{v'' < v'} \sum_{J''} A(v'J' \to v''J'')\right]$$

The term $A(v'J' \to v''J'')$ is defined as the Einstein coefficient for spontaneous emission.

The calculation of the Einstein coefficients is an on-going topic of research and requires the calculation of the electric dipole function. The determination of the electric dipole function involves experimental determination of the absolute transition probabilities. The Einstein coefficients used in this thesis for the OH molecule were determined by *Mies* [1974] who used the electric dipole moments of *Stevens et al.* [1974] and the results are in good agreement with the coefficients determined experimentally by *Potter et al.* [1971] and *Murphy* [1971].

If the system is in a steady state (production and loss mechanisms are equal), the number density of the upper state will remain constant. In this case, the intensity of an emission line (in photons/sec.) will be given by

$$I(v'J' \to v'', J'') = N_{v'J'} A(v'J' \to v''J'').$$

The number density of the upper state $|v', J'\rangle$ can be separated into a term dependent only on the vibrational quantum number v' and the total angular momentum J'. The assumption that the molecule is in local thermodynamic equilibrium implies that $N_{J'}$ is defined by a Boltzmann distribution. Thus, the total number density is given by

$$N_{v'J'} = \frac{N_{v'} 2(2J' + 1) \exp[-E_{J'}/kT_{rot}]}{Q_R}$$

where $E_{J'} = hcF(J')$ is the energy of the state, k is Boltzmann's constant, T_{rot} is the rotational temperature of the emitting molecule, and Q_R is the partition function (sum over all states)

$$Q_R = 1 + 3\exp[\frac{-2Bhc}{kT}] + 5\exp[\frac{-6Bhc}{kT}] + \cdots \approx \frac{kT}{hcB}.$$

where B is a constant.

The assumption of thermodynamic equilibrium implies that if T_{th} is the local ambient temperature, then the molecule has undergone enough collisions while in the excited state that $T_{rot} = T_{th}$. As a result, the intensity of a given emission line is defined by the formula

$$I(v'J' \to v'', J'') = \frac{N_{v'} A(v'J' \to v'', J'') \exp[F(J')hc/kT_{th}]}{Q_R} \qquad A.2$$

The line intensities for the OH band emission were calculated by substituting previously calculated values for the rotational term values [Coxon and Foster 1982] and the transition probabilities [Mies 1974] into Equation A.2. The O_2 band intensities were calculated using the term values and transition probabilities from Krassovsky [1963].

The substantial difference in the emission spectrum of OH and O_2 is due primarily to the fact that O_2 is a symmetric molecule while OH is not. Not only does this bring the O_2 lines together but it eliminates the separation between the Q and R branches since the symmetry of the O_2 molecule removes one of the degrees of freedom and thus, the Q-branch overlaps the R and P branches.

BIBLIOGRAPHY

Baker, D. J., Studies of atmospheric infrared emissions, Air Force Geophysical Laboratory Report # AFGL-TR-78-0251, 1978.

Bloomfield, P., Fourier analysis of time series: An introduction, John Wiley & sons, New York, 258 pp, 1976.

Chamberlain, J. W., Theory of planetary atmospheres, Vol 22 in International Geophysics Series, Academic Press, New York, 330 pp, 1978.

Coxon, J. A. and S. C. Foster, Rotational analysis of hydroxyl vibration-rotation emission bands: molecular constants for OH X, $6 \geq v \leq 10$, *Can. J Phys.*, *60*, 41, 1982.

Donahue, T. M., B. Guenther, and R. J. Thomas, Distribution of atomic oxygen in the u pper atmosphere deduced from Ogo 6 airglow observations. *J. Geophys. Res.*, *78*, 6662, 1973.

Dunkerton, T. J., Stochastic parameterization of gravity wave stress, *J. Atmos. Sci.*, *39*, 1711, 1982.

Fastie, W. G., A small plane grating monochromator, *J. Optical Soc. Am.*, *42*, 9, 642, 1952.

Fritts, D. C., Gravity wave saturation in the middle atmosphere: A review of theory and observations, *Rev. of Geophys. and Space Phys.*, *22*, 275, 1984.

Fritts, D. C. and R. A. Vincent, Mesospheric momentum flux studies at Adelaide, Australia: Observations and a gravity wave-tidal interaction model, *J. Atmos. Sci.*, *44*, 605, 1987.

Gardner, C. S., and D. G. Voelz, Lidar studies of the nightime sodium layer over Urbana Illinois: Gravity waves, Electro-Optic Systems Lab. Tech. Rept. No. 06-002, University of Illinois, Urbana Illinois, Sept., 1986.

Hamwey, R. M., A spectrophotometric study of hydroxyl emissions from a high latitude winter mesopause, M. S. thesis, Univ. of Alaska, Fairbanks, Alaska, 107 pp, 1985.

Hecht, J. H., R. L. Walterscheid, G. G. Sivjee, A. B. Christensen, and J. B. Pranke, Observations of wave driven fluctuations of OH nightglow emission from Sønderstrømfjord, Greenland, Submitted to *J. Geophys. Res.*, 1987.

Hickey, M. P., Effects of eddy viscosity and thermal conduction and coriolis forces in the dynamics of gravity wave driven fluctuations in the OH nightglow, Submitted to *J. Geophys. Res.*, 1987a.

Hickey, M. P., Wavelength dependence of eddy dissipation and coriolis force in the dynamics of gravity wave driven fluctuations in the OH nightglow, Submitted to *J. Geophys. Res.*, 1987b.

Hickey, M. P. and K. D. Cole, A quartic dispersion equation for internal gravity waves in the thermosphere, *J. Atmos. Terr. Phys.*, *49*, 889, 1987.

Hines, C. O., Internal atmospheric gravity waves at ionospheric heights, *Can. J. Phys.*, *38*, 1441, 1960.

Hines, C. O. and D. W. Tarasick, On the detection and utilization of gravity waves in airglow studies, *Planet. Space. Sci.*, *35*, 851, 1987.

Holton, J. R., An introduction to dynamic meterology, Second ed., Vol. 23 International Geophysics Series, Academic Press, New York, 391 pp, 1979.

Holton, J. R. and X. Zhu, A further study of gravity wave induces drag and diffusion in the mesosphere, *J. Atmos. Sci.*, *41*, 2953, 1984.

Houghton, J. T., The stratosphere and mesosphere, *Q. J. R. Meteorol. Soc.*, *104*, 1, 1978.

Houghton, J. T., The physics of atmospheres, Second ed., Cambridge University Press, Cambridge, 271 pp, 1986.

Hunsucker, R. D., Atmospheric gravity waves generated in the high-latitude ionosphere, *Rev. Geophys. Space Phys.*, *20*, 293, 1975.

Jenkins, G. M., and D. G. Watts, Spectral analysis and its a pplications, Holden-Day, California, 525 pp, 1968.

Krassovsky, V. I., Infrasonic variations of OH emission in the upper atmosphere, *Ann. Geophys.*, *28*, 739, 1972.

Krassovsky, V. I., and M. V. Shagaev, Optical method of recording acoustic or gravity waves in the upper atmosphere, *J. Atmos. Terr. Phys.*, *36*, 373, 1974a.

Krassovsky, V. I., and M. V. Shagaev, Inhomogeneities and wavelike variations of the rotational temperature of atmospheric hydroxyl, *Planet. Space Sci.*, *22*, 1334, 1974b.

Krassovsky, V. I., and M. V. Shagaev, On the nature of internal gravitational waves observed from hydroxyl emission, *Planet. Space Sci.*, *25*, 200, 1977.

Krassovsky, V. I., and N. N. Shefov, The intensities of u pper atmopheric emissions and internal gravity waves, *Ann Geophys.*, *32*, 43, 1976.

Krassovsky, V. I., K. I. Kuzmin, N. A. Piterskaya, A. I. Semenov, M. V. Shagaev, N. N. Shefov, and T. I. Toroshelidze, Results of some airglow observations of internal gravitional waves, *Planet. Space Sci.*, *23*, 896, 1975.

Krassovsky, V. I., B. P. Potapov, A. I. Seminov, M. V. Shagaev, N. H. Shefov, and T. I. Toroshelidze, Internal gravity waves near the mesopause and the hydroxyl emission, *Ann. Geophys.*, *33*, 347, 1977.

Kvifte, G., Nightglow observations at Ås during the I.G.Y., *Geophys. Pub.*, *20*, 1, 1959.

Lindzen, R. S., Turbulence and stress owing to gravity wave and tidal breakdown, *J. Geophys. Res.*, *86*, 9707, 1981.

Meek, C. E., I. M. Reid, and A. H. Manson, Observations of mesospheric wind velocities: 1. Gravity wave horizontal scales and phase velocities determined spaced wind observations, *Radio Sci.*, *20*, 1363, 1985.

Mies, F. H., Calculated vibrational transition probabilities of $OH(X^2_\pi)$, *J. Mol. Spectrosc.*, *53*, 150, 1974.

Moreels, G., and M. Herse, Photographic evidence of waves around the 85 km level. *Planet. Space Sci.*, *25*, 265, 1977.

Moreels, G., G. Megie, V. Vallance Jones and R. L. Gattinger, An oxygen hydrogen atmospheric model and its application to the OH emission problem, *J. Atm. Terr. Phys.*, *39*, 551, 1977.

Murphy, R. E., Infrared emissions of OH in the fundamental and first overtone bands, *J. Geophys. Res.*, *54*, 4852, 1971.

Myrabø, H. K., Temperature variations at mesopause levels during winter solstice at 78°N, *Planet. Space Sci.*, *32*, 249, 1984.

Myrabø, H. K., K. Henriksen, C. S. Deehr, and G. J. Romick, O_2 ($b^1\Sigma_g^+ - X^3\Sigma_g^-$) atmospheric band night airglow measurements in the northern polar cap region, *J. Geophys. Res., 89*, 9145, 1984.

Myrabø, H. K., C. S. Deehr, G. J. Romick, and K. Henriksen, Midwinter intensities of the night airglow O_2(0-1) atmospheric band emission at high latitudes, *J. Geophys. Res., 91*, 1684, 1986.

Myrabø, H. K., C. S. Deehr, R. A. Viereck, K. Henriksen, Polar mesopause gravity wave activity in the sodium and hydroxyl night airglow, *J. Geophys. Res., 92*, 2527, 1987.

Noxon, J. F., Effect of internal gravity waves upon night airglow temperatures, *Geophys. Res. Lett., 5*, 25, 1978.

Peterson, A. W. and L. M. Kieffaber, Infrared photography of OH airglow structures. *Nature, 244*, 92, 1973.

Potter, A. E., R. N. Coltharp, and S. D. Worley, Mean radiative lifetime of vibrationally excited hydroxyl, *J. Chem. Phys., 54*, 992, 1971.

Richmond, A. D., and S. Matsushita, Thermospheric response to a magnetic substorm, *J. Geophys. Res., 83*, 999, 1978.

Romick, G. J., The detection and study of visible spectrum of the aurora and airglow, *Proc. Soc. Photo. Opt. Instrum. Eng., 91*, 63, 1976.

Schubert G. and R. L. Walterschieid, Wave-driven fluctuations in OH nightglow from and extended source region, Submitted to *J. Geophys. Res.*, 1987.

Sivjee, G. G., R. L. Walterscheid, J. H. Hecht, R. M. Hamwey, G. Schubert, and A. B Christensen, Effects of atmospheric disturbances on polar mesopause airglow OH emissions, *J. Geophys. Res., 92*, 7651, 1987.

Smith, S. A., Gravity wave dynamics near the mesopause over Poker Flat Alaska, Ph. D. - thesis, Univ. of Alaska, Fairbanks, 190 pp, 1985.

Smith, S. A., D. C. Fritts, and T. E. Van Zandt, Comparison of mesospheric wind spectra with a gravity wave model, *Radio Sci., 20(6)*, 1331, 1985.

Stevens, W. J., G. Das, M Whal, M. Krauss, and D. Neumann, Study of the ground state potential curve of OH, *J. Chem. Phys., 61*, 3686, 1974.

Takahashi H., P. P. Batista, Y. Sahai, and B. R. Clemesha, Atmospheric wave propaga-
tion in the mesopause region observed by the OH(8-3) band, NaD, $O_2A(8645\text{Å})$
band, and OI 5577Å nightglow emissions, *Planet Space Sci*, *33*, 381, 1985.

Taylor, M. J., M. A. Hapgood, and P. Rothwell, Observations of gravity wave propagation
in the OI (557.7 nm), Na (589.2 nm) and the near infrared OH airglow emissions,
Planet. Space. Sci., *35*, 413, 1987.

Walterscheid, R. L. and G. Schubert, A dynamical-chemical model of tidally driven
fluctuations in the OH nightglow, *J. Geophys. Res.*, *92*, 8775, 1987.

Walterscheid, R. L., G. Schubert, and J. M. Straus, A dynamical-chemical model of wave
driven fluctuations in the OH nightglow, *J. Geophys. Res.*, *92*, 8775, 1987.

Weinstock, J., Theory of the interacion of gravity waves with O_2 airglow, *J. Geo-
phys. Res.*, *83*, 5175, 1978.

Witt, G., J. Stegman, B. H. Solheim, and E. J. Llewellyn, A measurement of the O_2
atmospheric band and the OI green line in the nightglow, *Planet Space Sci.*, *27*,
341, 1979.